MECHANICS & MALIGNANCY:

PHYSICAL CUES AND CHANGES THAT DRIVE TUMOR PROGRESSION

A Dissertation
Presented to
The Academic Faculty

By

Daniel J. McGrail

In Partial Fulfillment
of the Requirements for the Degree
Doctor of Philosophy in the
School of Chemical and Biomolecular Engineering

Georgia Institute of Technology

August, 2015

Mechanics & Malignancy:

Physical cues and changes that drive tumor progression

Approved by:

Dr. Michelle Dawson, Advisor
School of Chemical and Biomolecular Engineering
Georgia Institute of Technology

Dr. Mark Prausnitz
School of Chemical and Biomolecular Engineering
Georgia Institute of Technology

Dr. Mark Styczynski
School of Chemical and Biomolecular Engineering
Georgia Institute of Technology

Dr. John McDonald
School of Biology
Georgia Institute of Technology

Dr. Manu Platt
School of Biomedical Engineering
Georgia Institute of Technology

Date Approved: July 16, 2015

In memory of my grandmother, who taught me more about life
than I could ever hope to learn about science.

ACKNOWLEDGEMENTS

This work would not have been possible without the guidance, help, and support from many people.

I would like to thank all of my committee members Dr. Manu Platt, Dr. Mark Prausnitz, Dr. Mark Styczynski, and Dr. John McDonald for serving on my committee. I am specifically grateful Dr. John McDonald as well as Roman Mezencev and other members of his lab for the helpful conversations, as well as experimental advice and reagents.

I thank my advisor, Dr. Michelle Dawson, for her guidance and patience throughout my time at Georgia Tech. Though after our first meeting I feared I would never grasp the long strings of acronyms she so easily breezed through, countless hours of conversation with her have garnered a level of scientific fluency I hadn't imagined possible. I thank her for teaching me how to design scientific research, for all the times she has supplied me with the tools needed to test these ideas, and for all the times she did not kick me out of the lab when they ended in great failure. In particular, I thank her for going out on a limb and allowing me the flexibility to pursue my curiosities in the completion of this project.

I thank all the members of the Dawson research group for their support while completing this project. I thank Kate McAndrews for listening to my non-stop ramblings as I reasoned by way through the projects. I thank Deepraj Ghosh for all the late nights and times he was around to help stop an experiment so I could get a "full six hours" of sleep. I must also thank a series of amazing undergraduates who helped perform these

experiments, not only for their time but also for their motivation to work which helped keep me moving forward even on days where I was feeling sluggish and tired. I thank Nhat Quach for both his help with molecular biology while in this lab as well as later helpful discussions as he went on to pursue his own graduate degree. I thank Jason Iandoli for his help quantifying substrate-dependent adhesion. I am grateful to Quang Kieu for a number of experiments, most notably his impeccable staining technique and his help starting our work with tumor spheroids. I thank Mark Qi for his hours of help as we first struggled to isolate chemoresistant cells. I thank Krishan Patel for the countless hours he spent helping optimize and run adhesion kinetics experiments as well as helping spear head our work on temporal responses to chemotherapeutics. I thank Niti Khambhati for her perseverance helping to get western blots working and other assistance in studying chemoresistance. I thank Kishan Pithadia for his continual willingness to help, even with the most boring of protocols. I thank Chandler Brandenburg for the hours she spent helping image on the microscope. Finally, I thank Nithin Ravikumar for his amazing perseverance even as his first project failed in moving forward with helping with the spheroid studies and transfection studies.

Finally, I would like to thank my family for all of they have done for me over the years. Without their love and dedication none of this would be possible.

TABLE OF CONTENTS

LIST OF TABLES

LIST OF FIGURES

LIST OF SYMBOLS AND ABBREVIATIONS

ANOVA	analysis of variance
BCC	breast cancer cell
BrdU	5-bromo-2'-deoxyuridine
CFSE	carboxyfluorescein succinimidyl ester
δ	phase angle
DAPI	4',6-diamidino-2-phenylindole
$\mathcal{D}_{eff}$	effective diffusion coefficient
DMSO	dimethylsulfoxide
EMT	epithelial to mesenchymal transition
η	dynamic viscosity
FAK	focal adhesion kinase
FDR	false discovery rate
G'	elastic modulus
G"	viscous modulus
HBSS	Hanks's buffered saline solution
Hz	hertz
IC50	half maximal inhibitory concentration
k	drug efflux rate
LPA	lysophosphatidic acid
MLCK	myosin light chain kinase
μM	micromolar
mM	millimolar

μm	micrometer
MPT	multiple particle tracking
MSC	mesenchymal stem cell
MTT	3-(4,5-dimethylthiazol-2-yl)-2,5-diphenyltetrazolium bromide
nM	nanomolar
nm	nanometer
OCC	ovarian cancer cell
Pa	pascals
PBS	phosphate buffered saline
P-gp	P-glycoprotein
PIV	particle image velocimetry
ρ	Perason correlation coefficient
ROCK	Rho-associated protein kinase
σ_{rr}	radial stress
SEM	standard error of the mean
τ	time lag
TFM	traction force cytometry
τ_r	relaxation time
UV	ultraviolet

SUMMARY

Despite advances in the molecular regulators of cancer, patient survival rates have stagnated. Mechanical cues from the extracellular matrix can induce a malignant phenotype, and the spread of cancer which results in 90% of cancer-related deaths is also a mechanical process. This work first shows that metastatic ovarian cancer cells, which preferentially metastasize to soft tissue, become more malignant on soft matrices by increasing adhesion, growth, chemoresistance, and migration as well as undergoing epithelial-to-mesenchymal transition (EMT). However, most cancers such as breast become more malignant on stiff matrices, so we next contrasted metastatic ovarian cancer cells with breast cancer cells. We show that matrix preference is dependent on basal levels of cytoskeletal tension and can be reversed or blocked by modulating cytoskeletal tension. To understand the biophysical changes associated with the phenomena observed on soft substrates, we next utilized matched cell lines that were either chemoresistant or had undergone EMT independent of substrate rigidity. To analyze chemoresistance, cells resistant to microtubule-targeting Taxol were isolated from ovarian cancer cell lines. We found that these cells altered their adhesion to produce down-stream changes in microtubules culminating in Taxol resistance. Next, in a genetically-induced EMT model we found near-identical phenotypic changes as seen with substrate-induced EMT. Moreover, these studies also revealed that mesenchymal cells are softer and can no longer support solid stress. Finally, we identify an actin-sodium channel pathway responsible for supporting solid stress. Taken together, this biophysical analysis reveals key pathways associated with cancer progression and identifies multiple pathways that could be targeted to reverse these changes, paving the way for novel therapeutic strategies.

CHAPTER 1
INTRODUCTION

In Hanahan and Weinberg's seminal review "The Hallmarks of Cancer" they summarize 25 years of advances in oncology to conclude that the cornerstone of cancer is dynamic genomic alterations, in particular oncogenes and tumor suppressor genes that undergo either gain or loss of function, respectively. They go on to predict that the next era of research will produce a vastly different type of science, not only technically, but also conceptually (1).

Over a decade later their prediction remains accurate. New treatment strategies often target the tumor stroma, which is essential for tumor growth and metastasis. Angiogenic inhibitors, like bevacizumab, offered new hope for treating tumors, even those resistant to chemotherapy, by targeting their blood supply and starving the tumors of nutrients and oxygen. However, initially promising anti-angiogenic therapies have failed in part to a variety of factors including the onset of tumor hypoxia, which reduces chemotherapeutic delivery (2), enriches cancer stem cell populations (3), and contributes to tumor metastasis (4). These results have led to a paradigm shift from attempting to block the growth of new blood vessels to attempting to "normalize" the vasculature (5).

In addition to changes in existing paradigms, entirely new fields have come to the forefront of research, most notably physical oncology. By analyzing the physical forces exerted on and by the cells, physical oncology utilizes a multi-disciplinary tool kit to

understand the complexities of cancer growth and metastasis. Some of the ideas could be seen as a resurrection of Stephen Paget's 1889 'seed and soil' hypothesis which sought to explain the observation that certain cancer cells, or seeds, seem to prefer specific metastatic sites, or soil (6). Mammary tumors are often stiffer than the surrounding tissue and can be detected by physical palpitation (7). Further investigation of this phenomena revealed that this increase in stiffness can directly induce malignant transformation (8) and promote breast cancer metastasis (9). Metastasis, ultimately responsible for 90% of cancer-related deaths (10), is also fundamentally a mechanical process orchestrated by the dynamic rearrangement of the cytoskeleton.

This project began by seeking to understand the cause of this matrix-stiffness dependence by integrating cellular mechanics and molecular biology. It then evolved to further demonstrate how intracellular biophysical changes are important as cells become resistant to chemotherapeutics or undergo a switch to the metastatic phenotype known as epithelial to mesenchymal transition. Finally, it concludes by documenting how distinct biophysical phenotypes are required for the metastatic process and solid tumor growth while elucidating the molecular drivers of both.

CHAPTER 2
BACKGROUND

In recent years a growing body of evidence has emerged highlighting the importance of mechanical cues in both normal tissue development and progression of diseases such as arteriosclerosis, muscular dystrophies, osteoporosis, and cancer (11). The ability of a cell to sense and interact with its local environment is so important that it is conserved across essentially all life from humans down to the simplest single-celled bacteria (12). Despite highly divergent chemical signaling cascades, a highly conserved feature of mechanical signaling is that it requires transmission of force from the extracellular matrix (ECM) to the internal cytoskeleton which forms the structure of the cell.

2.1 The Cytoskeleton

The cytoskeleton of mammalian cells consists of three primary classes of polymeric proteins: actin microfilaments, intermediate filaments, and microtubules. Of these, actin and microtubules (shown in Figure 2.1) largely control key cell functions such as motility, polarity, and division (13). Though microtubules, which are largely responsible for intracellular trafficking, cannot bear significant stress, they are supported by the other cytoskeletal filaments (14). F-actin provides the greatest structural integrity at commonly encountered stress levels, but at very high strains F-actin depolymerizes and more deformable intermediate filaments are required to maintain cell structure (15).

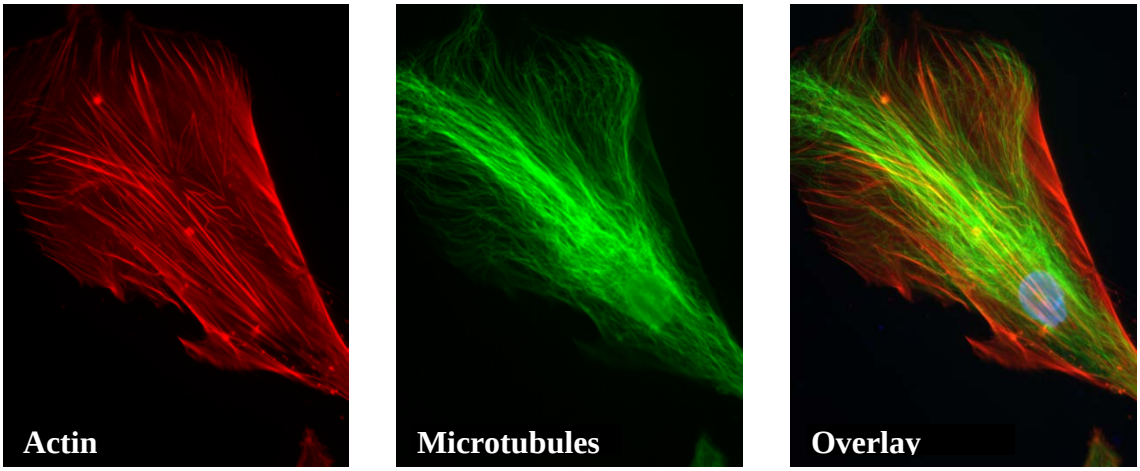

Figure 2.1 Micrograph of cytoskeletal filaments. A human mesenchymal stem cell after staining for F-actin (red), β-tubulin (green), and nucleus (blue).

In addition to requiring these structural filaments cells must also be able to adhere to the external environment. This is accomplished through an array of cell adhesion molecules; here we will focus on cadherins and integrins, responsible for cell-cell and cell-matrix adhesion, respectively (16). Integrins are heterodimeric trans-membrane receptors composed of one α-chain and one β-chain that bind to specific ECM molecules. The α-chain is largely responsible for ECM specificity while the β-chain links to the actin cytoskeleton (17). After binding the ECM, integrins transduce signals either by direct binding with F-actin or via adapter proteins in focal adhesion complexes (18). Cadherins (calcium-dependent adhesion molecules) are responsible for cell-cell adhesion. They play key roles during tissue morphogenesis by controlling cell sorting, arrangement, and morphology (19). These molecules can bind directly to F-actin or interact through other intermediates (20), and can even bear force (21). Loss of cell-cell adhesions, in particular E-cadherin, along with increased integrin expression are indicative of epithelial

to mesenchymal transition (EMT), which plays a crucial role in normal development as well as cancer metastasis by enhancing cell migratory capacity (22).

2.2 EMT, Cell Motility, and Metastasis

Epithelial cells typically display a cuboidal morphology with high levels of E-cadherin expression allowing the formation of tight junctions and cell monolayers. These cells tend to reside in more developed tissues, whereas during development cells may need to transition to the more migratory mesenchymal phenotype (22). By shedding E-cadherin responsible for cell-cell adhesion and increasing expression of ECM-binding integrins, EMT allows for cells to migrate in response to chemical or mechanical cues (23). Furthermore, expression of ECM-degrading matrix metalloproteinases on their surface allows for degradation of the basement membrane and dissemination to other tissues (24).

In order for cells to migrate in response to these cues, they must undergo a highly coordinated series of steps (25) as shown in Figure 2.2. First, actin monomers on the leading edge polymerize to form filaments leading to small protrusions known as filopodia or larger lamellipodia. As they do, integrins bind ECM molecules to form adhesions to stabilize the protrusions. As the adhesions connect to the actin cytoskeleton, the cell begins to exert force via actomyosin contraction, which propels it forward (26). Thus, in addition to controlling cell motility, this series of linkages may serve as mechanotransducers.

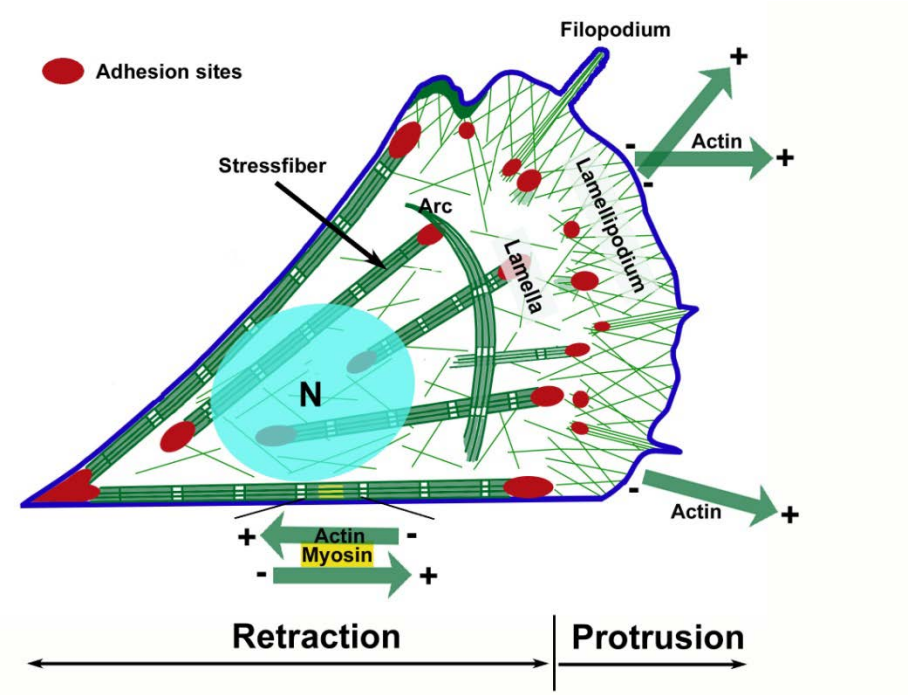

Figure 2.2 Illustration of cell migration, adapted from (27)

2.2 Mechanotransduction

Cells convert mechanical cues into biochemical signals through a process known as mechanotransduction. Though cells must be able to sense a variety of mechanical cues such as shear stress, compression and tension forces, and pressure, this discussion will focus on the cell's ability to sense matrix rigidity (28). Two primary mechanisms will be discussed: (1) force-induced confirmation changes in focal adhesion complexes and (2) actomyosin contraction via the Rho/ROCK pathway (Figure 2.3).

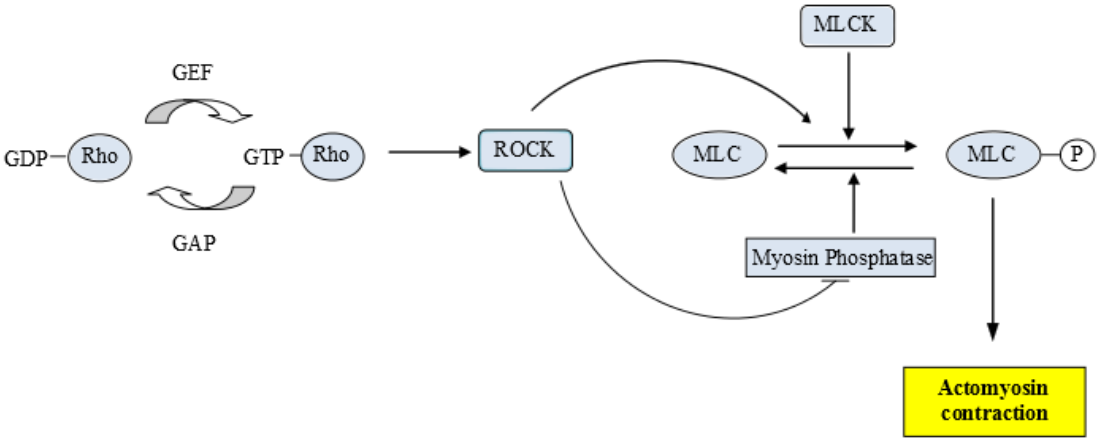

Figure 2.3 Rho/ROCK pathway illustration. GTPase nucleotide exchange factors (GEFs) and GTPase activating proteins (GAPs) help regulate Rho activity by changing it from its inactive GDP-bound form to active GTP-bound form. This active GTP-bound form can then act to phosphorylate Rho-associated protein kinase (ROCK). ROCK influences myosin contraction both by activating myosin light chain (MLC) and blocking MLC deactivation through myosin phosphatase. Myosin can also be activated directly through myosin light chain kinase (MLCK).

Focal adhesion complexes consist of an array of adapter and signaling proteins such as α-actinin, FAK, talin, paxillin, and vinculin (29). It has been shown that increasing cytoskeletal tension, either through increased actomyosin contraction or increased matrix rigidity will increase vinculin recruitment and focal adhesion size (30). Though vinculin can support force, this tension was dispensable for vinculin recruitment (31). Instead, conformational changes in the protein talin were shown to reveal multiple cryptic vinculin binding domains allowing for increased vinculin recruitment (32). The tension required to induce this conformational change in talin is generated via actomyosin contraction. Thus, though adhesion proteins contribute to mechanotransduction, cell-generated contractile forces ultimately control the mechanosensitivity of cells to their extracellular environment stiffness (33).

2.3 Matrix Stiffness and the Malignant Phenotype

As illustrated by the groundbreaking work of Paszek et. al., this mechanotransduction pathway is not simply a passive, unidirectional response to matrix stiffness but can ultimately feed an autocrine loop and promote malignant transformation (8). Integrin binding to ECM results in guanidine exchange factors (GEFs) activating small GTPases such as RhoA (34). RhoA in turn activates rho-associated kinase (ROCK) ultimately leading to phosphorylation of myosin light chain (MLC), inactivation of MLC phosphatase, and increased actomyosin contractility (35). Moreover, RhoA can also serve to drive cell cycle progression, which may increase the proliferation of tumor cells (36). Once malignancies begin to develop, lysyl oxidase-driven matrix crosslinking promotes invasion of the cancer into surrounding tissues (37). As matrix stiffening continues, cancer cells must continually activate RhoA in order to maintain force equilibrium (38).

The direct effects of actomyosin contractility on tumor progression were elegantly elucidated by Samuel et. al. using a murine squamous cell carcinoma (SCC) model (39). Skin is a mechanoresponsive tissue that must actively balance forces between cellular actomyosin tension and collagen fibrils (40). Noting that Rho and ROCK signaling are associated with SCC (41), the authors chose to directly investigate how actomyosin tension influences tumor progression. They showed that increasing cellular tension by activating ROCK elevated tissue stiffness and led to hyperproliferation, which was reversible upon reducing actomyosin contractility via downstream effectors. Finally, ROCK activation increased overall tumor load, which was also inhibited by ROCK blockade, directly implicating actomyosin tension in cancer progression (39).

2.4 Mechanical Stresses in Tumor Progression

In addition to altered matrix mechanics, the tumor mechanical microenvironment additionally has increased fluid and solid stresses. The former fluid stresses include interstitial fluid pressure (IFP), which is typically less than or equal to arterial intravascular pressures allowing for perfusion of fresh nutrients from the blood stream. As nutrients are consumed by the cells, lower pressures in venous capillaries and lymphatics then allows for recirculation of the fluid and resulting by products. As early as 1950 it was recognized that this fluid pressure was elevated in tumors relative to normal tissue (42). Almost 40 years later Rakesh Jain proposed that this increased IFP may be a barrier to drug delivery (43, 44). In the coming years researchers would document elevated IFP in most solid tumors including head and neck, breast, melanoma, cervical, and colorectal (45). Moreover, increased IFP is linked with poor patient prognosis (46–48) and normalization by enzymatic ablation of stromal components can radically improve survival (49).

These fluid phase stresses are further complicated by solid phase stresses accumulated during tumor growth. As a tumor expands and comes into contact with local tissue, it must exert sufficient force to overcome resulting compressive stresses (50). These stresses typically represent mechanical loads of 50-200 mmHg (51, 52) which can prevents the growth of cancer cell spheroids (51). This growth-induced stress co-evolves with IFP and may be a key factor controlling the increases in IFP seen in solid tumors (52). Furthermore, these mechanical stresses deform local blood vessels further hindering

drug delivery (53). Despite the importance of solid stress in tumor growth, few studies have explored how cancer cells physically support this stress.

2.5 Chemotherapeutics and Evolution of Chemoresistance

Though cancer survival rates have shown some improvement in recent years, this is largely due to earlier detection from improved screening. For those with later stage disease at detection, prognosis remains poor. Approximately one out of every twenty women in America will be diagnosed with breast cancer at stage II or later when the disease is no longer localized to the breast (54). At this stage, even in patients with operable breast cancer given advanced drug cocktails survival to five years does not often exceed 60% (55). In ovarian cancer, the situation is even more dire due to lack of early detection techniques. Here, more than 75% of the patients are diagnosed after the cancer spreads from the primary site (54). When the entire tumor cannot be excised, clinicians must rely on chemotherapeutic drugs to eradicate any disseminated tumor cells. In ovarian cancer, standard treatment protocol of tumor resection followed by dual agent chemotherapy consisting of platinum therapy plus Taxol (paclitaxel) have increased progression-free survival to nearly 18 months and overall survival to 38 months (56). However, just as bacteria can acquire resistance to antibiotics tumor cells acquire resistance to these drugs. Once refractory, the disease rapidly progresses with progression-free survival of 3-5 months and overall survival rarely exceeding a year even with new experimental treatments (57).

2.6 Objectives and Outline

The overall goal of this project is to understand the role of biophysical changes during tumor progression and elucidate the molecular mechanisms to uncover next-generation targeted therapies. This begins in chapter 3 where we demonstrate that metastatic ovarian cancer cells become more proliferative, chemoresistant, and motile on soft surfaces and this corresponds with transitioning from a more epithelial phenotype to a more mesenchymal phenotype. This increased malignancy of soft matrices may explain ovarian cancer's predisposition to metastasize to the soft omentum fat pad (58). This result runs counter to most previously studied cell lines, of which 70% grew better on stiff surfaces with the remaining displaying matrix-independent growth (59). To understand this discrepancy, in chapter 4 we use contrast these metastatic ovarian cancer cells which become more malignant on soft matrices with metastatic breast cancer cells which become more malignant on hard matrices and found that levels of basal cell contractility determine their matrix preference. In chapter 5, we utilized Taxol-resistant cells to demonstrate how biophysical changes in adhesions can be transmitted to microtubules causing chemoresistance. In chapter 6, we sought to understand how the epithelial to mesenchymal transition (EMT) observed in chapter 3 altered cancer cell mechanics. To decouple EMT from matrix stiffness, we used a genetically engineered model of EMT that would maintain its epithelial or mesenchymal character regardless of matrix stiffness. These studies revealed that EMT induced several pro-migratory biophysical changes such as cytoplasmic and nuclear softening. However, this increased plasticity to improve migration came at the cost of decreased structural stability,

ultimately leading to inability to support solid stress in 3D tumor spheroids. Building on this finding, in chapter 7 we sought to understand the precise mechanisms used by tumor spheroids to support solid stress. These studies revealed that while cytoskeletal filament polymerization is required to survive under solid stress, it is predominately to support the ability of cells to alter their osmotic pressure by effluxing sodium. The overall findings are summarized in chapter 8 along with recommendations for future studies.

CHAPTER 3
THE MALIGNANCY OF METASTATIC OVARIAN CANCER CELLS IS INCREASED ON SOFT MATRICES[1]

3.1 Summary

Though current treatments for localized ovarian cancer are highly effective, it still remains the most lethal gynecological malignancy, largely in part to late detection after tumor cells leave the primary tumor. Clinicians have long noted a clear predilection for ovarian cancer metastasis to the soft omentum. Here, we show that this tropism is due not only to chemical signals but also mechanical cues. Metastatic ovarian cancer cells (OCCs) preferentially adhere to soft microenvironments and display an enhanced malignant phenotype including increased migration, proliferation, and chemoresistance. To understand the cell-matrix interactions used to sense the substrate rigidity, we utilized traction force microscopy and found that OCCs increased both the magnitude of traction forces as well as their degree of polarization. After culture on soft substrates, cells underwent morphological elongation characteristic of epithelial-mesenchymal transition, which was confirmed by molecular analysis. Consistent with the idea that mechanical cues are a key determinant in the spread of ovarian cancer, the observed mechanosensitivity was greatly decreased in less metastatic OCCs. Finally, we demonstrate that this mechanical tropism is governed through a Rho/ROCK signaling pathway.

[1]McGrail DJ, Kieu QMN, Dawson MR. (2014) The malignancy of metastatic ovarian cancer cells is increased on soft matrices through a mechanosensitive Rho-ROCK pathway. *J. Cell Sci.* 127: 2621–6.

3.2 Introduction

Ovarian cancer is the fifth leading cause of cancer deaths among women, largely because it is often diagnosed at late stages after metastasis with a 5 year survival rate of only 30% (60). In contrast to following the normal metastatic process of intravasation to the vascular system and extravasation at a distal site, ovarian cancer is more likely to disseminate through the intraperitoneal fluids. From there, it preferentially accumulates in soft tissues such as the adipocyte-rich omentum (58). Previous work suggests this is because adipocytes act as a rich energy source and actively promote ovarian cancer cell homing via cytokines such as interleukin-8 (58). However, these studies were based solely on chemical factors, whereas the burgeoning field of physical oncology has recently shown the mechanical environment a cell experiences can be of equal importance. For instance, pioneering studies by Weaver and colleagues demonstrated that increased matrix stiffness can induce a malignant phenotype in mammary epithelial cells by leading to increased Rho activation and actomyosin contractility (8), with further studies directly implicating contractility in increasing matrix stiffness and cancer progression (39). Though most of these studies linked increased matrix stiffness to tumor progression, breast cancer metastatic subclones with tropism for soft lung tissue *in vivo* exhibit growth advantages on soft substrates *in vitro* (61). Based on these results, we hypothesized that the preferential accumulation of ovarian cancer cells in soft tissues may be due to intrinsic mechanical properties of the environment.

To test this hypothesis, we utilized a series of biophysical and biochemical techniques to understand the response of ovarian cancer cells to a soft matrix similar to adipose tissue and a stiff matrix similar to tumor tissue (62, 63) using both the more metastatic SKOV-3 cell line and less metastatic OVCAR-3 cell line (64), both of which harbor either mutated or deleted p53 indicative of high grade serous ovarian carcinomas (65–67). We found that ovarian cancer cells (OCCs) show increased adhesion on soft microenvironments. After engraftment, OCCs on soft matrices are more proliferative and resistant to standard chemotherapeutic drugs. In addition to these increases in growth, cells also displayed increased migratory capacity. Further immunocytochemistry and gene expression analysis revealed a shift from a more epithelial phenotype on stiff substrates to a more mesenchymal phenotype on soft matrices. Cell-matrix interactions were directly probed with traction force cytometry and revealed changes in both force magnitude and polarization on softer matrices. Moreover, use of small molecule modulators of the Rho/ROCK pathway demonstrates this signaling cascade plays a key role in determining this tissue tropism. This study reveals the previously undocumented role of mechanical cues in ovarian cancer metastasis which could lead to new methods to target metastatic disease.

3.3 Results and Discussion

3.3.1 Ovarian cancer cells preferentially engraft, expand, and migrate on soft substrates.

Following dissemination from the primary tumor ovarian cancer cells frequently engraft onto the mesothelial lining of the soft omentum. To probe if tissue stiffness plays

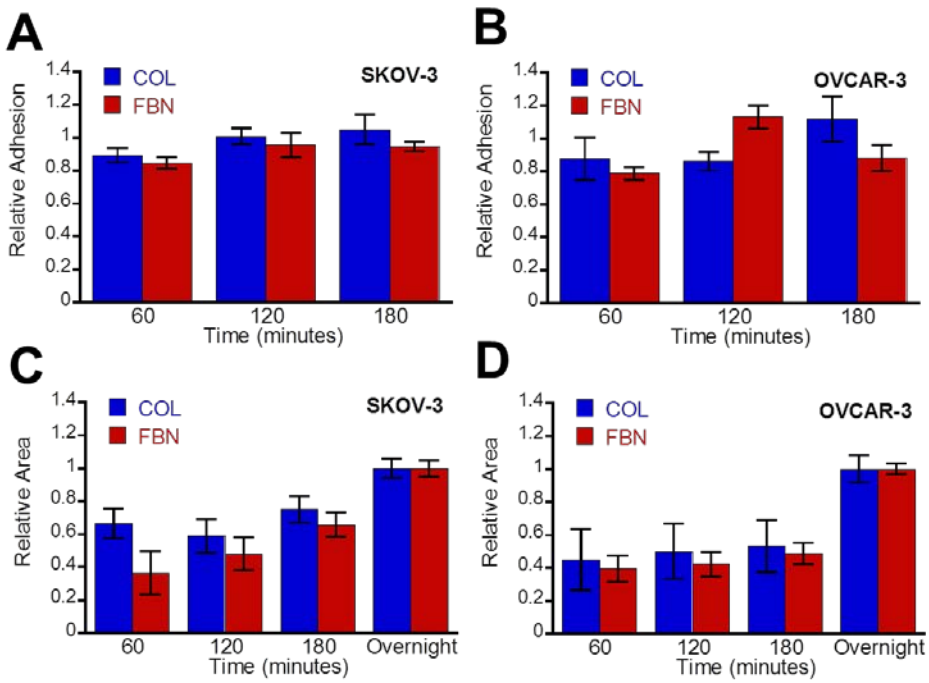

Figure 3.1 Ovarian cancer cells show equivalent adhesion and spreading on collagen I (COL) and fibronectin (FBN). (A,B) Cells were incubated for specified period of time on TCP coated with desired molecule and blocked with BSA and normalized to average adhesion at 180 minutes. (C,D) Cells spreading showed negligible differences on either ECM molecule.

a role in OCC engraftment, we utilized two model systems. First, we tested the adhesion of OCCs on a monolayer of hMSCs differentiated into either soft adipocytes (E ≈ 0.9 kPa) or stiffer osteoblasts (E ≈ 2.6 kPa) (72) which would both express ligands implicated in mesothelial engraftment such as VCAM-1 and CD44. We found that OCCs were significantly ($p<0.001$) more adherent on the softer adipocytes relative to stiffer osteoblasts. We next repeated this analysis on synthetic polyacrylamide substrates with elastic moduli mimetic of either adipose tissue (soft, 2.83 kPa) or tumor tissue (hard, 34.88 kPa) and found near identical changes in adhesion (Fig. 3.2A). Though these substrates were coated with collagen I, additional studies showed equivalent adhesion and

spreading on fibronectin (Fig. 3.1), which taken together with the results on cell monolayers suggests this result is not adhesion-ligand dependent.

After OCCs engraft into the secondary site, they must then survive and proliferate. Remarkably, after only 48 hours of culture there was nearly two times as many cells on the soft substrate as compared to collagen-coated glass, and significantly more than on hard substrates ($p<0.01$) (Fig. 3.2B). We hypothesized this increase in proliferation may lead to increased levels of chemotherapeutic-induced cell death, however treatment with carboplatin was significantly less effective on soft substrates (Fig. 3.2C), nearly replicating results seen previously when OCCs were cultured in a 3D environment (73). Finally, single-cell motility analysis revealed large increases in migration on soft substrates, as quantified by cell migration coefficient (Fig. 3.2D). Though the overall average migration coefficient increased almost 5-fold, the fastest 1% of cells increased over 30-fold (Fig. 3.4A), which may represent the small tumor cell subpopulation capable of metastasis.

After observing these functional alterations on soft substrates, we sought to probe cell-matrix interactions. To do so, we utilized traction force microscopy (TFM) to quantify the force exerted by cells on the underlying substrate (Fig. 3.2Ea). We found that when cultured on soft matrices, OCCs exerted more force (Fig. 3.2Eb), often indicative of increased metastatic phenotype (74). Previous work has demonstrated that during invasion into the sub-mesothelial environment ovarian cancer cells utilize myosin-dependent traction force to clear the mesothelial cell layer (75) . Our results indicate this

key step in ovarian cancer invasion may be exacerbated by the mechanical properties of the omentum. Additionally the cells were more capable of polarizing these forces on the soft substrates (Fig. 3.2Ec), a crucial step for effective cell migration. These changes in force profiles corresponded with changes in phosphorylated myosin light chain (pMLC) in both overall intensity and polarization (Fig. 3.2F).

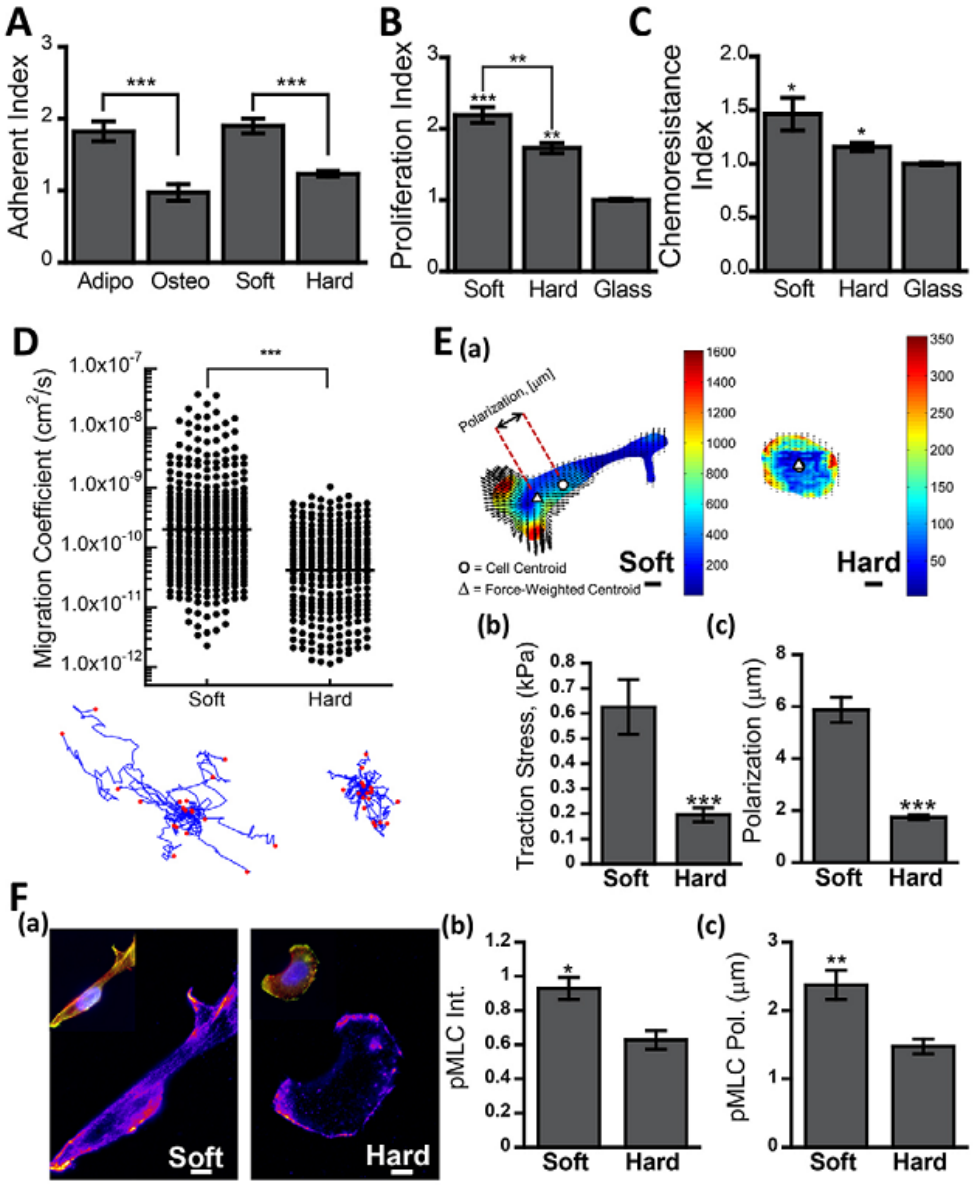

Figure 3.2 Metastatic SKOV-3 ovarian cancer cells display increased malignant phenotype on soft matrices. (A) Adhesion to soft microenvironments shows that OCCs are more adherent on soft adipocytes relative to osteoblasts, with near identical changes seen on soft and hard polyacrylamide substrates. (B) After engrafting, cells proliferated more on soft substrates relative to hard substrates, with both values being significantly greater than the collagen-coated glass control. (C) Cells on compliant matrices showed increased viability after treatment with 50μM carboplatin. (D) Analysis of cell motility tracks revealed significantly higher cell migration coefficient on soft substrates. (E) Heat maps of traction stresses in Pascals overlaid with black arrows showing cell-induced matrix displacements (E,a). The cell center of mass is shown by the circle (○) and the triangle (Δ) shows the force-weighted center of mass. Quantification of the cell-exerted traction forces show increased peak traction stresses (E,b), as well as force polarization (E,c), defined as the difference in cell center of mass and force-weighted center of mass (scale bar = 10 μm) (F) Staining for pMLC revealed a increase in pMLC intensity and polarization.

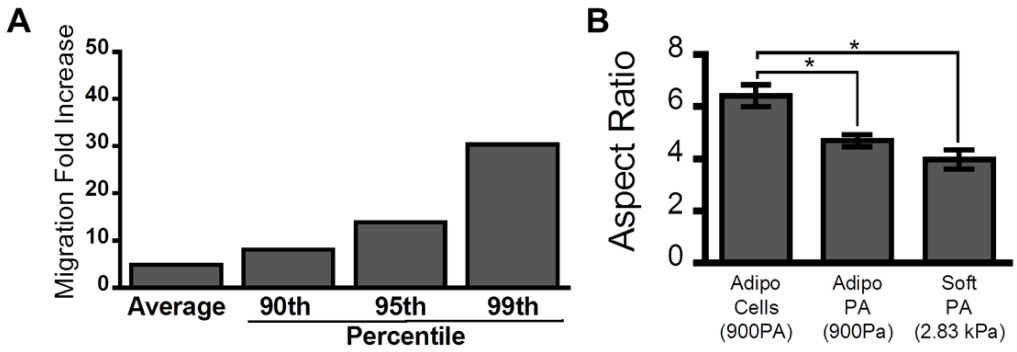

Figure 3.4 Most motile cells and elongation on softer substrates. (A) Metastatic SKOV-3 motility shows a 5-fold increase on soft substrates relative to hard for the population average, but the most motile subpopulations show exponentially higher fold changes reaching an over 30-fold increase for the fastest 1% of cells. (B) Culturing cells on polyacrylamide substrates with rigidities comparable to the differentiated adipocyte monolayers does not reproduce the observed elongation, suggesting soluble factors released by the cells are a contributing factor.

3.3.2 Culturing OCCs on soft substrates induces more mesenchymal phenotype

When grown on soft substrates or soft cells, OCCs displayed a more elongated morphology indicative of a mesenchymal phenotype, with cells cultured on adipocyte monolayers exhibiting the most elongation at nearly six times long as wide (Fig. 3.4A). This may be due in part to soluble factors released by the cells as polyacrylamide substrates of similar rigidities did not recapitulate this elongation entirely (Fig. 3.3B). Cell aspect ratio was near equivalent on osteoblasts and the soft matrix, both of which have similar elastic moduli. However, all evaluated culture substrates showed increased elongation over the collagen-coated glass control. Based on the elongated morphology and increased migration indicative of a mesenchymal phenotype, we hypothesized cells were undergoing epithelial-mesenchymal transition. To test this, we first stained cells for

the intermediate filament cytokeratin which is preferentially expressed in epithelial cells. We found that OCCs cultured on soft substrates displayed nearly 5-fold less cytokeratin ($p<0.01$) than when cultured on collagen-coated glass (Fig. 3.4B). This finding was validated with qRT-PCR which showed increases mesenchymal markers (Fig. 3.4Ca) as well as decreases in epithelial markers (Fig. 3.4Cb) when OCCs were cultured on compliant matrices.

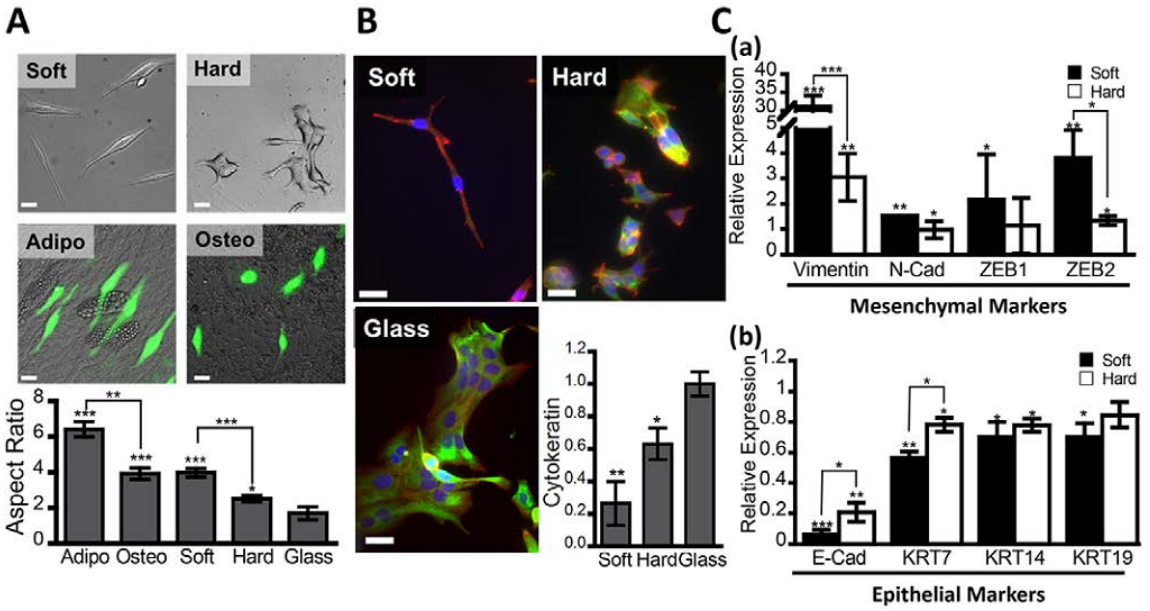

Figure 3.4 Increased malignant phenotype correlates with epithelial-mesenchymal transition. (A) SKOV-3 cells show morphological elongation consistent with a more mesenchymal phenotype on soft matrices as well as on soft adipocyte monolayers (SKOV-3 cells labeled green with CFSE). (B) Staining cells with pan-cytokeratin (green) and F-actin (red) shows decreased cytokeratin expression on softer substrates (scale bar = 50 μm) (C) Gene expression analysis shows both an up-regulation of mesenchymal markers (C,a) as well as down regulation of epithelial markers (C,b) relative to collagen-coated glass control.

3.3.3 Mechanosensitivity is decreased in less invasive OCCs.

After finding that compliant matrices produced a more metastatic OCC phenotype, we next questioned if this mechanosensitivity was conversely decreased in a less

metastatic cell line. To do so, we utilized poorly metastatic OVCAR-3 cells (64). In contrast to their more metastatic counterparts, these cells showed no significant advantage in adhesion, proliferation, chemoresistance, or migration on soft substrates (Fig. 3.5A). To test if this was due to altered interactions with the underlying substrate, we repeated the TFM and found a slight increase in traction stresses on soft matrices (Fig. 3.5B), though the change was much smaller than that observed in more metastatic cells. In contrast to previously studied types of cancer (74), the peak traction forces exerted by the less invasive cells were actually higher than those exerted by the more metastatic cells. However, the more aggressive SKOV-3 cells showed a larger fold increase in traction forces on soft substrates suggesting that force modulation based on matrix stiffness may be a more relevant parameter for grading cell invasiveness than the absolute magnitude of the force (Fig. 3.5Bd). When evaluating changes in epithelial/mesenchymal character, we found that the less metastatic OCCs still showed decreases in cytokeratin expression, though even on soft substrates these values were still equivalent to SKOV-3 on glass (Fig. 3.5Ca). Confirmation with gene expression analysis showed similar changes (Fig. 3.5Cb).

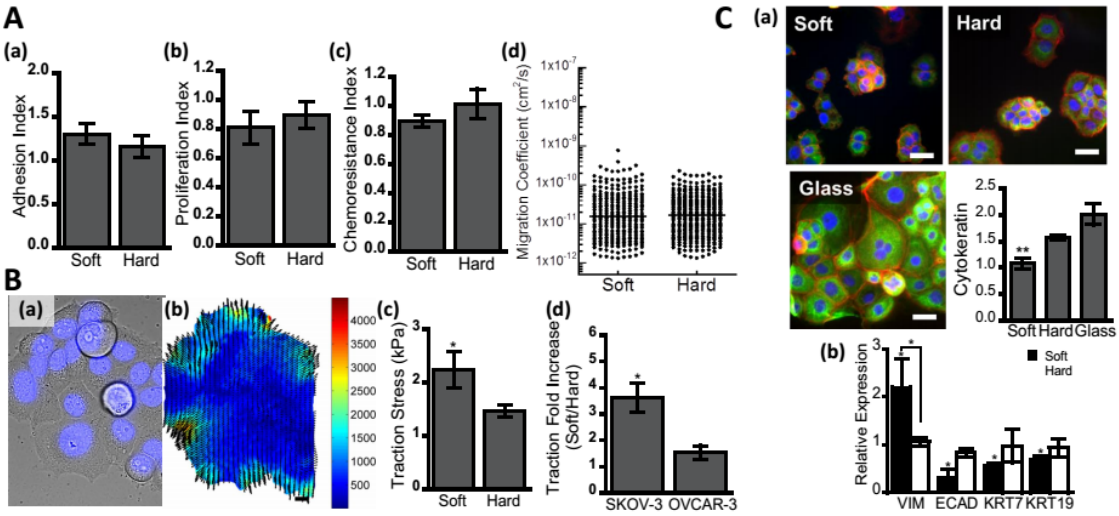

Figure 3.5 Less metastatic OVCAR-3 ovarian cancer cells show decreased mechanosensitivity. (A) Previously observed changes in adhesion (A,a), proliferation (A,b), carboplatin resistance (A,c), and migration (A,d) were no longer observed in the less metastatic cells. (B) Image of OVCAR-3 cells labeled with NucBlue on stiff substrates (B,a) and underlying traction forces in Pascals overlaid with black arrows to show matrix displacements (scale bar = 10μm) (B,b). Quantification of peak traction stresses shows slight increase on soft substrates (B,c). Fold increase in traction force on soft substrates shows significantly larger changes in SKOV-3 cells relative to OVCAR-3. (B,d). (C) OVCAR-3 cells show decreased changes in epithelial/mesenchymal character by (C,a) quantitative image analysis of OVCAR-3 cells labeled with F-actin (red) and pan-cytokeratin (green) (values normalized to SKOV-3 on glass, scale bar = 50μm) and expression of EMT-associated genes (C,b).

3.3.4 OCC mechanical preference is controlled through a Rho/ROCK pathway

Since Rho and Rho kinase (ROCK) have both been associated with matrix-stiffness induced malignancy (8, 39) and mechanotransduction (11) we hypothesized these molecules may play a role in the changes observed in this study. To probe this, we treated metastatic OCCs either with LPA to activate Rho/ROCK or inhibited ROCK with Y27632 and H1152.

Consistent with previous literature reports that LPA is often increased in ovarian cancer patients and leads to increased cell invasion (76), LPA induced marked migration

on hard substrates with rigidities similar to the primary tumor (Fig. 3.6Aa). This LPA-induced motility on hard substrates bore great phenotypic resemblance to that seen natively on soft matrices including cell elongation (Fig. 3.6Ab), increased traction forces and force polarization (Fig. 3.6C). In contrast to this, on soft matrices LPA drastically reduced migration and caused cells to collapse to a rounded morphology (Fig. 3.6Ab). TFM revealed similar peak traction stresses for LPA treated OCCs (Fig. 3.6B, Fig. 3.6Ca), though the decreased spread area (Fig. 3.7A) did result in a significantly less total force exertion on soft matrices (Fig. 3.7B). We hypothesize that on the soft matrix the Rho activation by LPA led to hypercontractility and subsequent cell collapse, such as that observed in neuronal cells, suggesting it may be characteristic of cells that prefer softer environments (77).

Inhibition of ROCK with either Y27632 or H1152 (Fig. 3.6Aa) produced rigidity-independent motility, suggesting it plays a key role in OCC mechanosensitivity. Moreover, ROCK inhibition greatly mitigated changes in EMT-associated genes (Fig. 3.6Ac). When grown on soft substrates Y27632 reduced traction forces (Fig. 3.6B, Fig. 3.6Ca). Though Y27632 induced modest increases in force on hard substrates, treatment with the more specific H1152 produced completely rigidity-independent forces and corresponding decreases in pMLC (Fig. 3.7Cb). This disparity may either be due to incomplete ROCK inhibition with Y27632 (Fig. 3.7Ca) or off-target effects of Y27632 (78). Despite the larger traction forces on hard substrates Y27632-treated OCCs showed no increase in motility, possibly due to the cell's inability to properly polarize forces (Fig.

3.6Cb). The near-complete force inhibition with H1152 greatly mitigated OCC motility regardless of matrix rigidity (Fig. 3.6Ac).

Our results are consistent with recent findings by Waterman and colleagues that below a threshold matrix stiffness cells utilize a subset of focal adhesions (FAs) for mechanosensing that undergo constant force fluctuations through a ‘tugging’ mechanism (79) and that these ‘tugging’ FAs exert larger forces than their stable counterparts. ROCK inhibition in tugging cells on soft matrices decreased pMLC and subsequent force exertion as observed here. In contrast to this, in ‘non-tugging’ cells on hard matrices ROCK inhibition induced tugging which could lead to the increased forces as seen on hard substrates (Fig. 3.6C). This theory would imply that ROCK inhibition essentially “decouples” the cell’s mechanosensing machinery, and indeed down-stream molecular and functional changes were largely mitigated with ROCK inhibition (Fig. 3.6A). Since cells on soft matrices can display biphasic behavior based on ECM density (80) future studies investigating the role of ECM density on Rho/ROCK mediated mechanosensitivity may help determine the interplay of these conditions required for ovarian cancer metastasis.

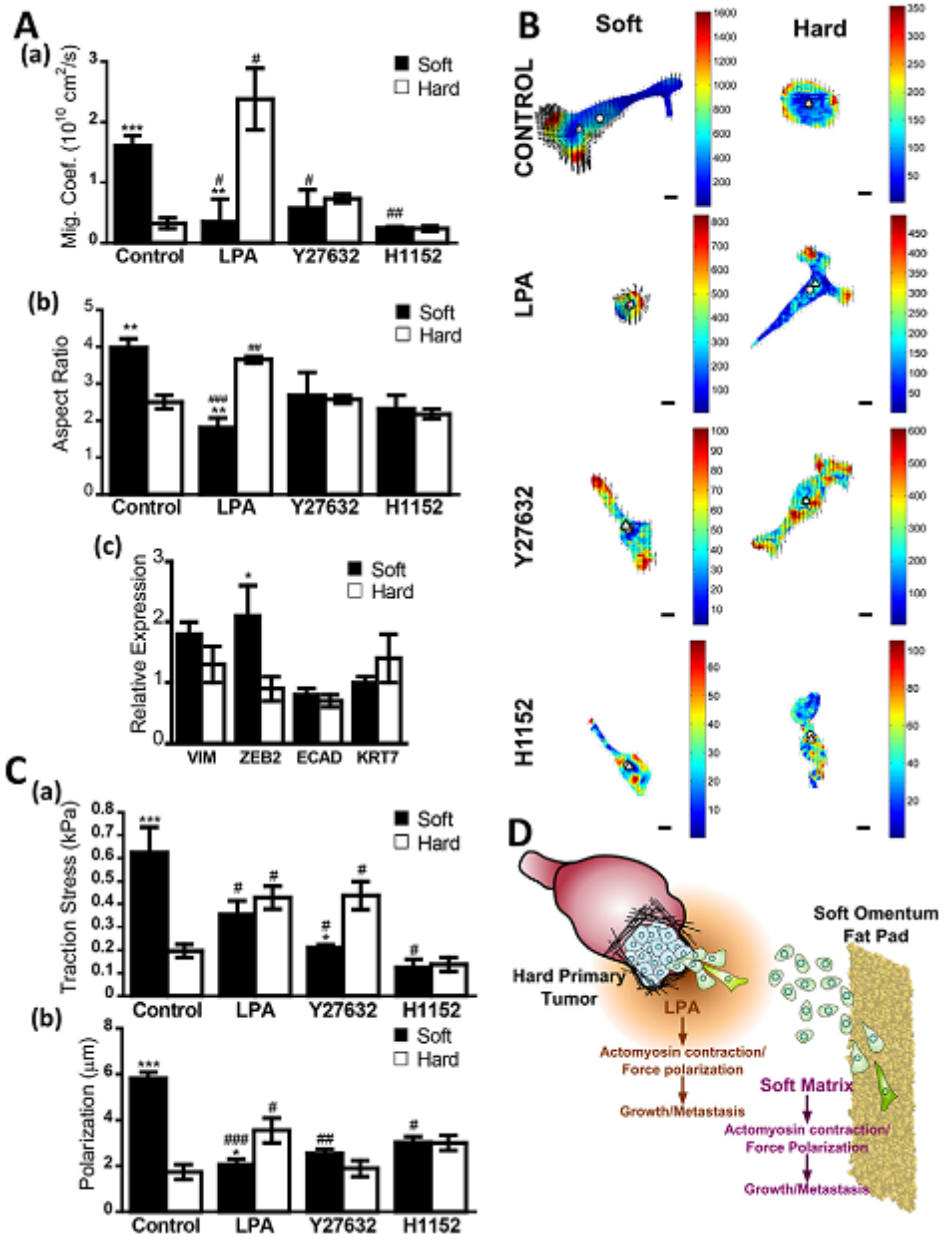

Figure 3.6 Mechanical tropism is governed by a Rho/ROCK pathway as demonstrated by Rho activation with 10μM LPA or ROCK inhibition with 10μM Y27632 and 1μM H1152. (A,a) LPA induced large increases migration on hard substrates, but inhibited migration on soft substrates. ROCK inhibition produced rigidity-independent migration with decreased migration on soft matrices and increased migration on hard matrices. (A,b) Similar trends in cell morphology were observed as quantified by cell aspect ratio. (A,c) ROCK inhibition with Y27632 mitigates changes in EMT-associated gene expression. (B) Tractions force maps as described in Figure 2 after treatment with small molecules. (C) Quantification of peak traction stresses (C,a) as well as traction force polarization (C,b). (D) Proposed model of ovarian cancer cell metastasis where LPA in the hard environment of the primary tumor induces change from less migratory/more epithelial cells (blue) to more migratory/mesenchymal cells (green). After spreading into the ascites fluid, engraftment into the soft omentum likewise results in a more aggressive mesenchymal phenotype.

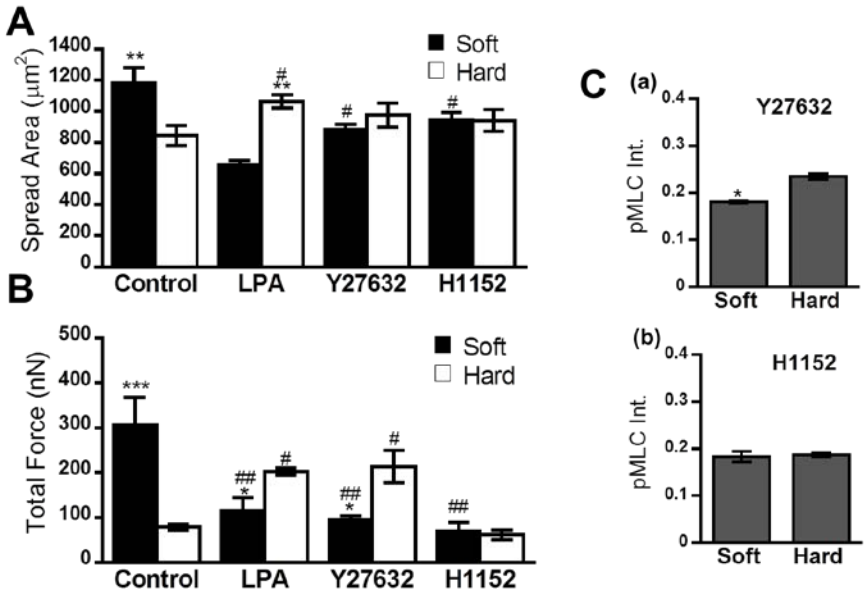

Figure 3.7 Spreading and force production in presence of Rho pathway modulation. (A) Spread area of SKOV-3 cells after Rho activation with LPA and ROCK inhibition with Y27632 or H1152. (B) Total force exerted by SKOV-3 cells after Rho activation with LPA and ROCK inhibition with Y27632 or H1152. (C) SKOV-3 cells treated with Y27632 show significantly higher pMLC on hard matrices, with no differences observed with H1152.

These findings hearken back to Stephen Paget's 1889 'seed and soil' hypothesis which sought to explain the observation that certain cancer cells, or seeds, seem to prefer specific metastatic sites, or soil (6). We posit that secreted soluble factors increase OCC homing to the omentum, and then mechanical cues from the matrix spur OCC engraftment, growth, and migration. Interestingly, nuclear lamin levels have recently been shown to scale with tissue stiffness (81), and microarray analysis of primary and metastatic ovarian tumors showed changes in lamin expression consistent with this result (82).

In conclusion, this report demonstrates a previously undocumented mechanical tropism in metastatic ovarian cancer cells regulated through a Rho/ROCK pathway. Based on these observations, we propose a model as outline in Figure 3.6D whereby high local amounts of LPA around the tumor increase OCCs growth and migration out of the primary tumor. Once in the peritoneal fluid, cells preferentially adhere to the omentum as they come in contact with the soft matrix. After adhering, the compliant matrix causes an increase in malignant characteristics including growth, chemoresistance, and motility. Taken together with recent studies implicating ascitic fluid flow in ovarian cancer cell EMT (83), this work further highlights the crucial role of mechanical cues on ovarian cancer metastasis. By further understanding about the factors affecting ovarian cancer metastatic tropism this work may help address the void of effective therapies for advanced-stage disease.

3.4 Materials and Methods

3.4.1 Cell culture and substrate synthesis

Ovarian carcinoma cells SKOV-3 and OVCAR-3 were cultured per manufacturer's instructions. Human mesenchymal stem cells (hMSCs) acquired from TAMU were differentiated as described (68) into adipocytes and osteoblasts (Fig. 3.8A). Polyacrylamide substrates (63) were coated with equal densities of Collagen I (Fig. 3.8B).

3.4.2 Adhesion, proliferation, chemoresistance, and cell motility

Cells labeled with CFSE (Biolegend) were allowed to adhere for two hours in HBSS with divalents before taking an initial florescence reading. A final reading was taken after removing non-adherent cells by washing with HBSS to determine adherent fraction. Cell proliferation was quantified by cell number increase 48 hours after plating. Chemoresistance was quantified using a MTT assay on cells treated with 50 μM carboplatin. All three parameters are reported relative to a collagen-coated glass control. For cell migration coefficient quantification, cells were imaged on an environmentally-controlled Nikon Eclipse Ti microscope and traces fit to the persistent random walk model (69).

3.4.3 Traction force microscopy

Cell-induced displacements were used to determine traction forces as previously described (70). To capture the traction forces of OVCAR-3 cells that grow in clumps and avoid inaccuracies arising from analyzing patches of cells, traction stress values are reported as the peak (95^{th} percentile) of traction forces (Fig. 3.8C). Polarization was defined as the difference between the centroid of the cell and the force-weighted center of mass (Fig. 3.8Ea).

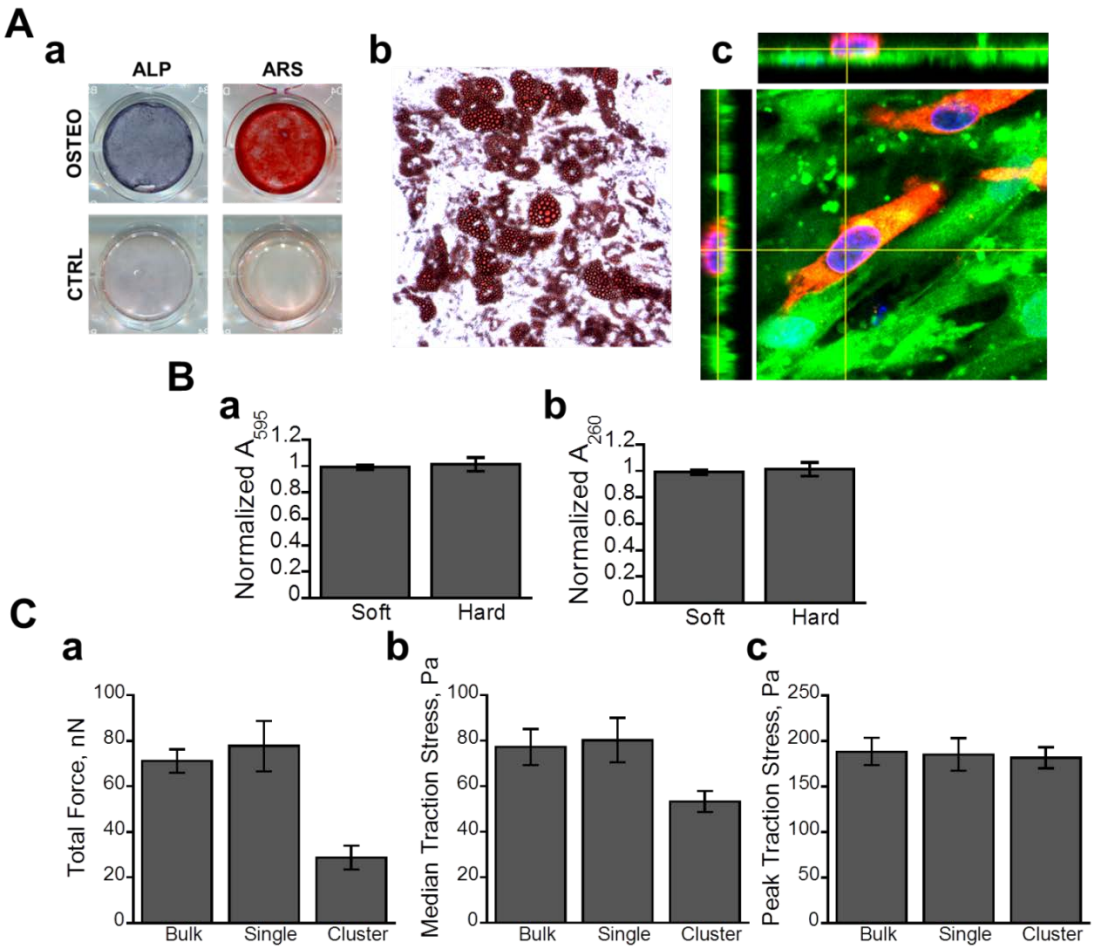

Figure 3.8 Differentiated hMSC monolayers, ECM conjugation to substrates, and traction force quantification. (A) Differentiation of human mesenchymal stem cells was confirmed by histological staining. (A,a) Osteoblasts were stained for both alkaline phosphotase (ALP) and calcium deposits with Alizarin Red S (ARS). (A,b) Adipocytes were stained with Oil Red O to label fat droplets. (A,c) After 24 hours of culture, SKOV-3 cells (labeled red with CM-DiI) do not invade hMSC monolayers (labeled green with CFSE) as verified by confocal microscopy. (B) Both substrates are conjugated with equal amounts of protein. (B,a) Surface protein quantification by staining with Coomassie G-250 and taking absorbance shows equal density on both substrate rigidities. (B,b) A similar trend was found by hydrolyzing surface proteins with 6N NaOH and then taking the absorbance of the release protein at 260 nm. (C) Traction forces of SKOV-3 clusters and single cells on hard substrates show that though parameters such as total force (C,a) and median stress (C,b) depending on if the cells are quantified as single cells or a cell cluster, peak traction stress remains unchanged regardless of cell density (C,c).

3.4.4 Immunofluorescence and gene expression characterization

Staining for cytokeratin was performed with anti-pan-cytokeratin (Biolegend) followed by incubation with rhodamine phalloidin and AlexaFluor 488 secondary (Invitrogen) before sealing with Vectashield with DAPI. Staining for pMLC was performed as described (71). Gene expression analysis normalized to 18s RNA are reported relative to collagen-coated glass (68).

3.4.5 Statistical Analysis

All studies were performed in triplicate or and are reported mean ± SEM. Statistical analysis was carried out using a student's t-test or ANOVA, considering $p<0.05$ to be significant (***$p<0.001$,**$p<0.01$,*$p<0.05$). For inhibitor studies, # signs compare samples to their untreated rigidity-matched controls.

CHAPTER 4
ACTOMYOSIN TENSION AS A DETERMINANT OF METASTATIC CANCER MECHANICAL TROPISM[2]

4.1 Summary

Despite major advances in the characterization of molecular regulators of cancer growth and metastasis, patient survival rates have largely stagnated. Recent studies have shown that mechanical cues from the extracellular matrix can drive the transition to a malignant phenotype. Moreover, it is also known that the metastatic process, which results in over 90% of cancer-related deaths, is governed by intracellular mechanical forces. To better understand these processes, we identified metastatic tumor cells originating from different locations which undergo inverse responses to altered matrix elasticity: MDA-MB-231 breast cancer cells that prefer rigid matrices and SKOV-3 ovarian cancer cells that prefer compliant matrices as characterized by parameters such as tumor cell proliferation, chemoresistance, and migration. Transcriptomic analysis revealed higher expression of genes associated with cytoskeletal tension and contractility in cells that prefer stiff environments, both when comparing MDA-MB-231 to SKOV-3 cells as well as when comparing bone-metastatic to lung-metastatic MDA-MB-231 subclones. Using small molecule inhibitors, we found that blocking the activity of these pathways mitigated rigidity-dependent behavior in both cell lines. Probing the physical forces exerted by cells on the underlying substrates revealed that though force magnitude may not directly correlate with functional outcomes, other parameters such as force

[2] McGrail DJ, Kieu QMN, Iandoli J a, Dawson MR. (2015) Actomyosin tension as a determinant of metastatic cancer mechanical tropism. *Phys. Biol.* 12: 026001.

polarization do correlate directly with cell motility. Finally, this biophysical analysis demonstrates that intrinsic levels of cell contractility determine the matrix rigidity for maximal cell function, possibly influencing tissue sites for metastatic cancer cell engraftment during dissemination. By increasing our understanding of the physical interactions of cancer cells with their microenvironment, these studies may help develop novel therapeutic strategies.

4.2 Introduction

The ability of a cell to sense and interact with its local environment is important in both normal tissue development such as directing cell lineage during stem cell differentiation as well as progression of diseases such as arteriosclerosis, muscular dystrophies, osteoporosis, and cancer (11). As illustrated by the groundbreaking work of Paszek et. al., this mechanotransduction pathway is not simply a passive, unidirectional response to matrix stiffness but can ultimately feed an autocrine loop and promote malignant transformation in breast cancer (8). Once malignancies begin to develop, lysyl oxidase-driven matrix crosslinking promotes the invasion of breast cancer into surrounding tissues (37). As matrix stiffening continues, cancer cells must continually activate the Rho/ROCK signaling pathway to increase cytoskeletal tension in order to maintain force equilibrium (38). The direct effects of actomyosin contractility on tumor progression were elegantly demonstrated by Samuel et. al. using a squamous cell carcinoma model showing ROCK activation catalyzed this transformation (39).

Despite this body of work, the literature is still unclear if this matrix stiffness-induced cancer progression is conserved throughout all cancers. Studies of larger sets of cancer cell lines have shown that 70% grew better on stiff substrates with the remaining displaying matrix-independent growth (59). Moreover, though the stiffness of metastatic site tissue *in vivo* has been shown to correlate with growth on rigidity-matched substrates *in vitro* (61), the mechanisms underlying this mechanical preference remain unknown. We recently demonstrated that ovarian cancer cells that preferentially metastasize to the soft omentum fat pad also become more malignant on soft matrices (84). Thus, we sought to compare these cells with metastatic MDA-MB-231 cells which become more malignant in hard environments in order to understand the drivers of this mechanical preference.

To accomplish this, we cultured cells on soft (2.83 kPa) and hard (34.88 kPa) polyacrylamide substrates and found that matrix-dependent differences in spreading appeared within two hours of culture and continued culture increased proliferation, chemoresistance, and motility on substrates of preferred rigidity. Microarray analysis revealed breast cancer cells have significantly higher expression of genes associated with contractility such as myosin light chain, myosin heavy chain, RhoA, and myosin light chain kinase (MLCK). Chemical blockade of these molecules mitigated rigidity-independent behavior. To probe how this inhibition was altering physical interactions with the underlying substrate, we performed traction force microscopy. Though inhibiting ROCK and MLCK produced equivalent functional outcomes this was accomplished through divergent changes in force profiles. This suggests a model that rigidity-dependent

cell function is determined by the ratio of relative contractility to substrate stiffness. If this ratio is too high, as seen for highly contractile MDA-MB-231 on soft, then the contractile forces overwhelm adhesive strength and cells collapse. Conversely, if this ratio is too low, as seen for the weakly contractile SKOV-3 cells on hard, cells do not have sufficient strength to spread. Alterations in the intrinsic level of contractility may be a necessary step to adapt to various tissue rigidities during metastasis as contractile gene expression signatures are shared with cells with *in vivo* tropism for tissues of different rigidities.

4.3 Results

4.3.1 Metastatic Breast and Ovarian Cancer Function Best on Opposite Matrix Rigidities

To characterize matrix stiffness dependent function we considered three primary malignant characteristics on soft (2.83 kPa) and hard (34.88 kPa) substrates as well as collagen-coated glass control: (1) the ability of cells to grow, (2) the ability of cells to survive chemotherapeutics, and (3) the ability of cells to migrate. Utilizing BrdU incorporation as a marker of cell proliferation we found that consistent with previous reports(73, 85) there were significantly less ($p<0.01$) proliferating MDA-MB-231 cells on soft substrates (Fig. 4.1A). Conversely, the fraction of SKOV-3 proliferating significantly increased on soft substrates over both hard substrates ($p<0.05$) and glass ($p<0.01$). Follow-up studies analyzing viability after 24 hour doxorubicin treatment revealed MDA-MB-231 cells on glass showed 20% higher viability than on soft substrates (Fig. 4.1B). SKOV-3 cells were more resistant to doxorubicin on both soft

($p<0.01$) and hard ($p<0.05$) substrates. Finally, we sought to quantify the effects of substrate rigidity on cell migration. To do so, cells on substrates were labeled with a live-

cell nuclear dye to track cell motion. MDA-MB-231 cells on hard substrates displayed higher velocities relative to those cultured on soft substrates with even larger gains in speed seen on glass (Fig. 4.1C). Though SKOV-3 cells exhibited overall lower velocities, they still were more motile on soft substrates than either hard substrates or glass. Analysis of additional less metastatic cell lines showed that this phenomenon was mitigated, suggesting it may be a property of metastatic cells (Fig. 4.2).

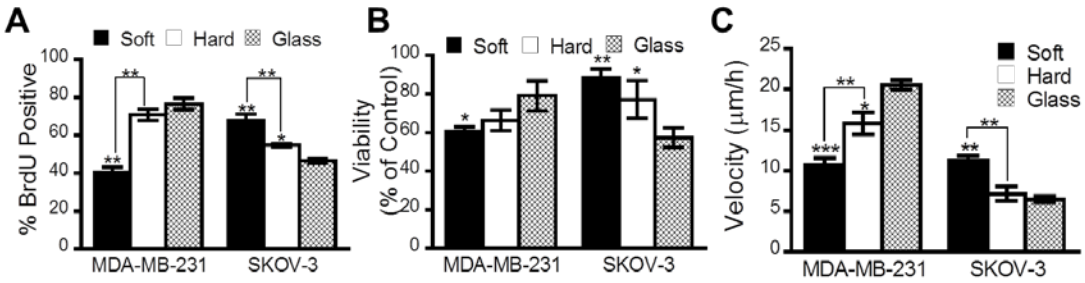

Figure 4.1 Spreading and force production in presence of Rho pathway modulation. (A) Cells were grown on substrates for 24 hours before introducing BrdU for incorporation into dividing cells. MDA-MB-231 cells are more proliferative on either hard or glass substrates than on soft whereas SKOV-3 cells show less proliferation on both hard and glass. (B) After overnight equilibration, cells were treated with doxorubicin for 24 hours before quantifying viability relative to a rigidity-matched control for each cell line using MTT revealing cells remained viable on hard and soft substrates, for MDA-MB-231 cells and SKOV-3 cells, respectively. (C) Quantification of cell velocity by tracking individual cells as they migrated on each substrate showed similar trends, with higher MDA-MB-231 velocities on hard and glass whereas SKOV-3 cells had higher velocities on soft substrates. All values plotted as mean ± SEM of >3 independent experiments. * $p<0.05$, ** $p<0.01$, *** $p<0.001$

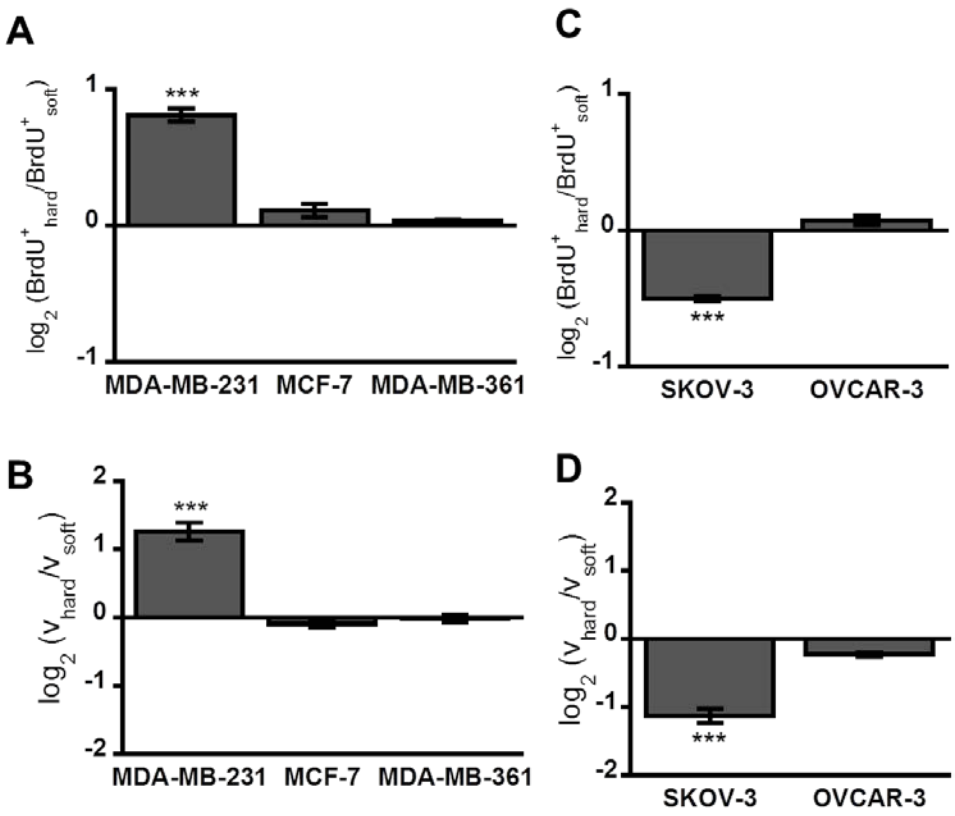

Figure 4.2 Less metastatic cells are less sensitive to matrix rigidity. Less metastatic breast (A-B), and ovarian (C-D) show greatly decreased response to matrix rigidity in terms of proliferation (A,C) and motility (B,D). . All values plotted as mean ± SEM of >3 independent experiments. * $p<0.05$, ** $p<0.01$, *** $p<0.001$

4.3.2 Adhesion and Spreading Dynamics

Next, we tested if the observed differences were also present at early time scales during adhesion to the substrates. For MDA-MB-231 cells there was no statistical difference between hard and soft substrates at any time points (Fig. 4.3A), which may explain their ability to initially adhere to the soft bone marrow when undergoing bone metastasis. In contrast to this, SKOV-3 cells adhered significantly more to soft substrates until the 3 hour time point after which differences were negligible (Fig. 4.3B). For both cell types

there was no difference in either weakly or strongly adherent fractions by the 3 hour time point, so any observed differences were not due to an inability of cells to adhere to the substrates.

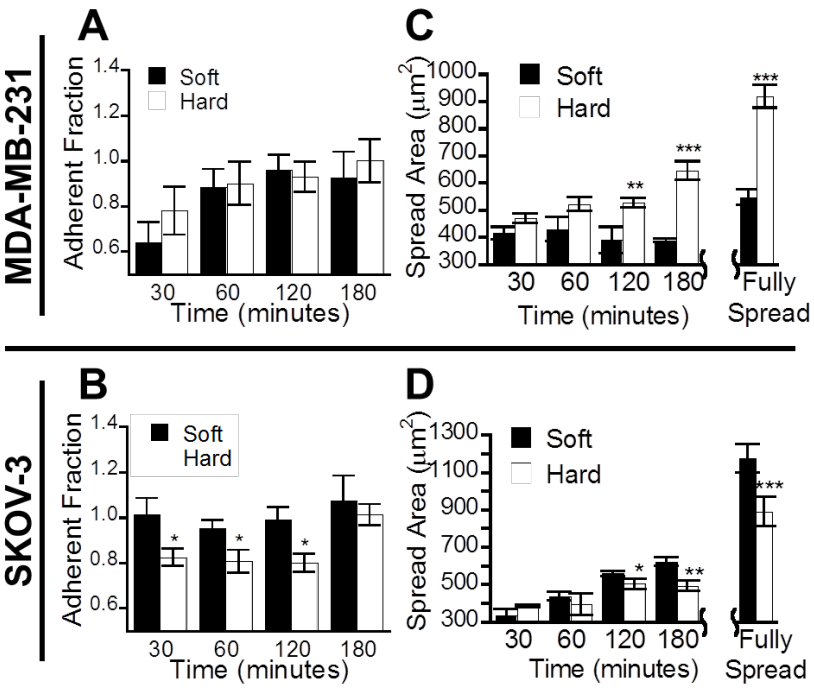

Figure 4.3 Effect of substrate rigidity on cell adhesion and spreading. (A-B) Fluorescently labeled cells were allowed to adhere for the specified length, and then adherent fraction quantified by relative fluorescence intensity before and after washing away non-adherent cells. The adherent fraction showed no differences for MDA-MB-231 (A) between hard and soft substrates, though at early time points SKOV-3 were significantly more adherent to soft substrates (B). Cells were fully adhered to both substrates by three hours. (C-D) Quantification of cell spreading over equivalent time points shows significant differences in spread area occurring after two hours for both MDA-MB-231 (C) and SKOV-3 (D) and persists after overnight incubation. All values plotted as mean ± SEM of >3 independent experiments. * $p<0.05$, ** $p<0.01$, *** $p<0.001$

Since early adhesion was largely unaffected by matrix stiffness, we next investigated the time scale at which differences emerge by determining the rate at which cells spread

on substrates of different rigidities through quantification of the area of stained filamentous actin. Through one hour, there was no significant difference in spreading. However, by two hours significant differences in spreading had emerged. Differences in the spread area persisted after cells reached their final size (Fig. 4.3C-D).

4.3.3 Microarray Analysis Reveals Differences in Contractile Pathways

To begin probing for differences between these two cell types, we utilized publically deposited microarray data sets to test for differences in gene expression. This analysis revealed that MDA-MB-231 cells showed significant higher expression of genes associated with actomyosin contraction (Fig. 4.4A). Notable differentially expressed genes include contractile genes such as *RHOA*, *MYLK*, and *ARHGEF18*, as well as *MYL9* and *MYH9*¸ subunits of non-muscle myosin II which we confirmed with RT-PCR verifying this trend held across rigidities to account for any potential lab to lab cell line variation (Fig. 4.4B). Interestingly, SKOV-3 cells expressed higher levels of genes associated with actin filament stabilization such as tropomyosin 2 (*TPM2*) (86) which may help compensate for the lack of cytoskeletal tension. Unsupervised hierarchal clustering of parental MDA-MB-231, as well as subclones that were selected *in vivo* to be bone metastatic or lung metastatic, showed that bone and lung cells form two unique clusters, and that parental cells clustered with bone-metastastic clones indicating they are most similar at the gene expression level (Fig. 4.5). Comparison of these sublcones that metastasize to either soft (lung) or hard (bone) microenvironments recapitulated many of the differences observed between SKOV-3 cells and MDA-MB-231 cells (Fig. 4.6). Due to the importance of RhoA and actomyosin contraction in mechanotransduction we

hypothesized this differential expression could be responsible for the differential response to matrix compliance.

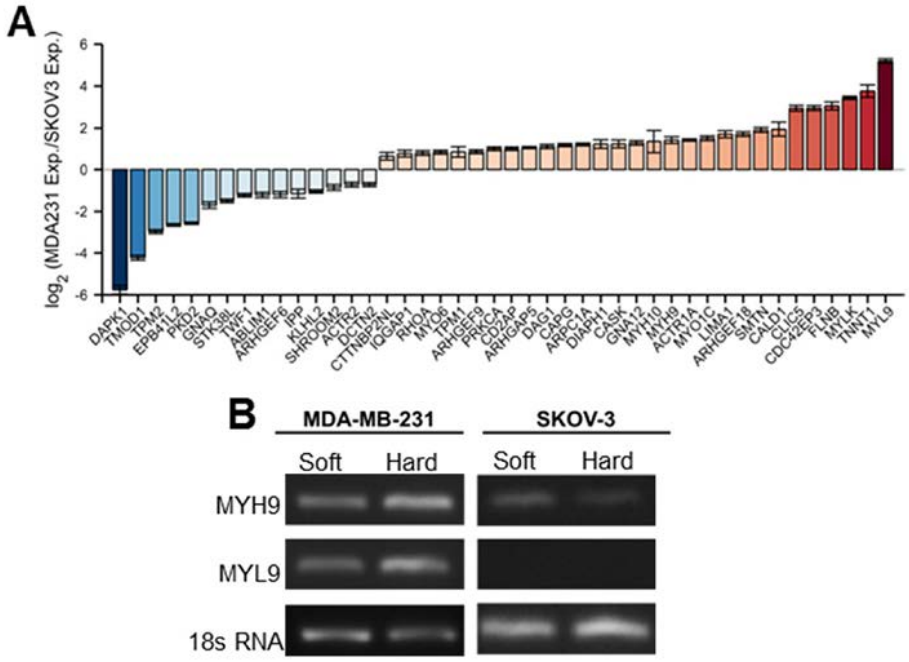

Figure 4.4 Actomyosin tension is up-regulated on cells that prefer stiff matrices and inhibition mitigates this preference. (A) Microarray gene expression analysis reveals higher expression of several genes associated with actomyosin tension, including genes encoding for myosin heavy and light chains, myosin light chain kinase, and RhoA. (B) RT-PCR validation of MYH9 and MYL9 in MDA-MB-231 and SKOV-3 confirming higher gene expression in MDA-MB-231 cells regardless of substrate rigidity.

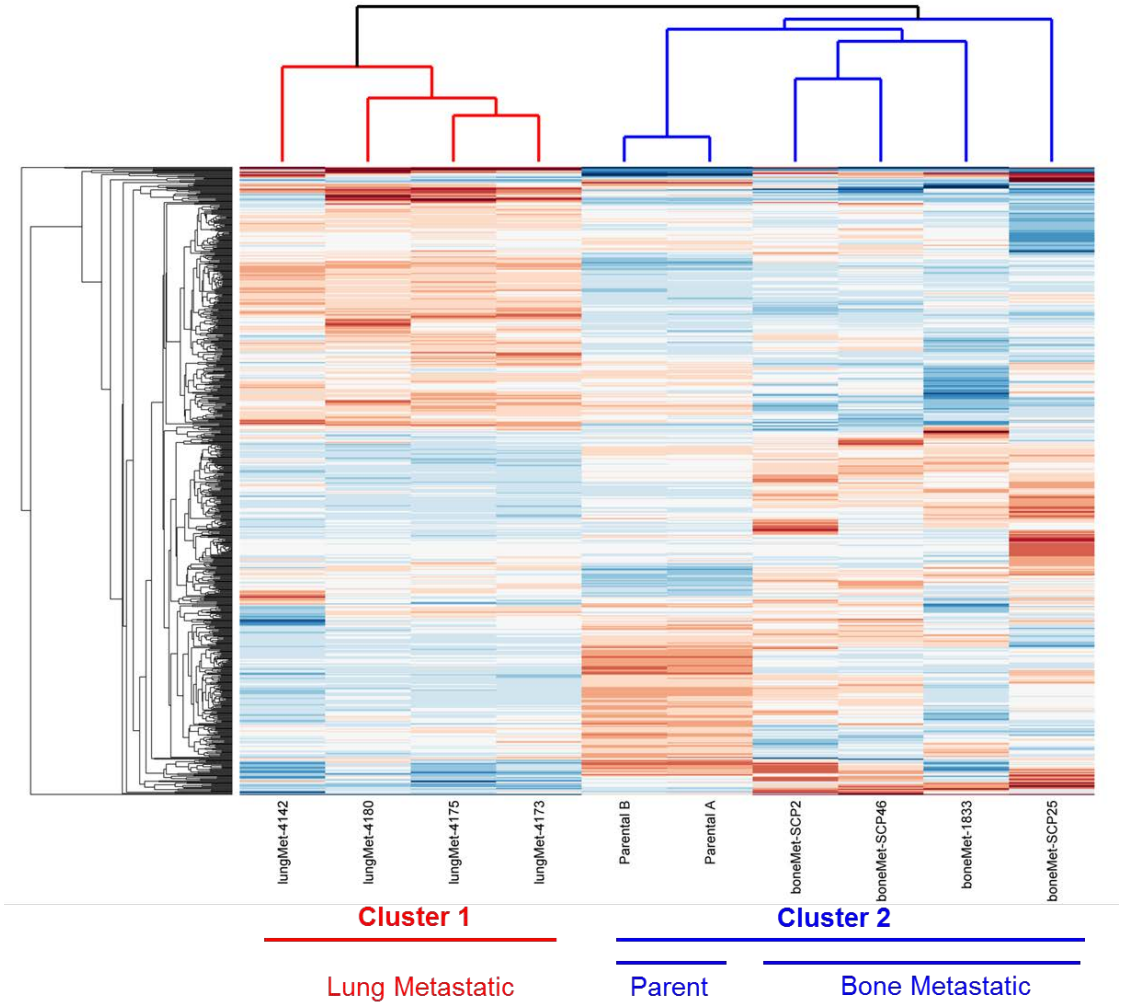

Figure 4.5 Unsupervised hierarchal clustering of lung metastatic, bone metastatic, and parental MDA-MB-231 cells shows that parental MDA-MB-231 cells cluster with the bone metastatic subclones, indicating they are genetically similar. Data were accessed from GEO accession GSE2603 and clustering performed in MATLAB GC-RMA background subtraction. Only probe sets with a standard deviation above 0.5 were used for clustering.

Gene	FC	Gene	FC
Up-Regulated		Down-Regulated	
**MYH10	1.96	BIN1	-0.32
**MYL9	0.99	DCTN3	-0.47
WASF3	0.98	RACGAP1	-0.48
SPTAN1	0.92	MYL6B	-0.49
**CDC42EP3	0.79	STK38L	-0.49
SPTBN1	0.77	**KLHL2	-0.50
**ARHGEF18	0.71	ARHGDIB	-0.51
FLII	0.68	SVIL	-0.52
SSH1	0.59	RASA1	-0.58
**ACTR1A	0.58	MYL6	-0.58
CORO1C	0.51	**PRKCA	-0.61
DLG1	0.47	**SHROOM2	-0.72
RND3	0.43	CLIC4	-0.75
ROCK1	0.41	**TWF1	-0.78
**FLNB	0.37	PLCB1	-1.70

Figure 4.6 Differential gene expression between bone metastatic and lung metastatic MDA-MB-231 subclones. Data was processed as described in methods with data from GEO accession GSE2603. FC is defined as log2(bone metastatic/lung metastatic) expression. ** denotes genes that were also differentially expressed between MDA-MB-231 and SKOV-3 cells as shown in Figure 4.4A.

4.3.4 Modulation of Cytoskeletal Tension Alters Rigidity-Dependent Behavior

Based on these observations, we sought to determine if blocking these differentially regulated pathways could mitigate the observed differences in mechanosensitivity. Analysis of spread area revealed that inhibiting either Rho-associated kinase (ROCK) with Y27632 or myosin light chain kinase (MLCK) with ML7 produced rigidity-independent spread area in both MDA-MB-231 (Fig. 4.7A) and SKOV-3 (Fig. 4.7B) cells. Inhibition of non-muscle myosin with blebbistatin in MDA-MB-231 cells allowed for increased spreading on soft substrates whereas cells on hard substrates had decreased spread area (Fig. 4.7A), though we could not perform further studies due to phototoxcitiy (87). If inhibiting contractility allowed for recovered MDA-MB-231 function on soft

substrates, we hypothesized increasing contractility in SKOV-3 cells may recover function on hard substrates. To test this, SKOV-3 cells were treated with Rho-activating LPA to increase contractility which increased their spread area on hard substrates but collapsed on soft substrates (Fig. 4.7B). Similarly, quantification of cell motility after treatment revealed that the ROCK and MLCK inhibition were sufficient to induce rigidity-independent migration in both cell lines (Fig. 4.7C-D), but Rho activation with LPA increased SKOV-3 motility on hard while decreasing it on soft (Fig. 4.7D). For both spreading and motility the changes were a result of the MDA-MB-231 cells gaining function on soft matrices as opposed to decreasing function on hard. Analysis of MDA-MB-231 proliferation when exposed to inhibitors still produced substrate-independent proliferation in MDA-MB-231 cells, but this was due to both increases in soft substrates as well as decreases in hard substrates (Fig. 4.7E) as opposed to merely a gain of function on soft substrates. For SKOV-3 cells, the inhibitors decreased function on soft matrices (Fig. 4.7B,D,F).

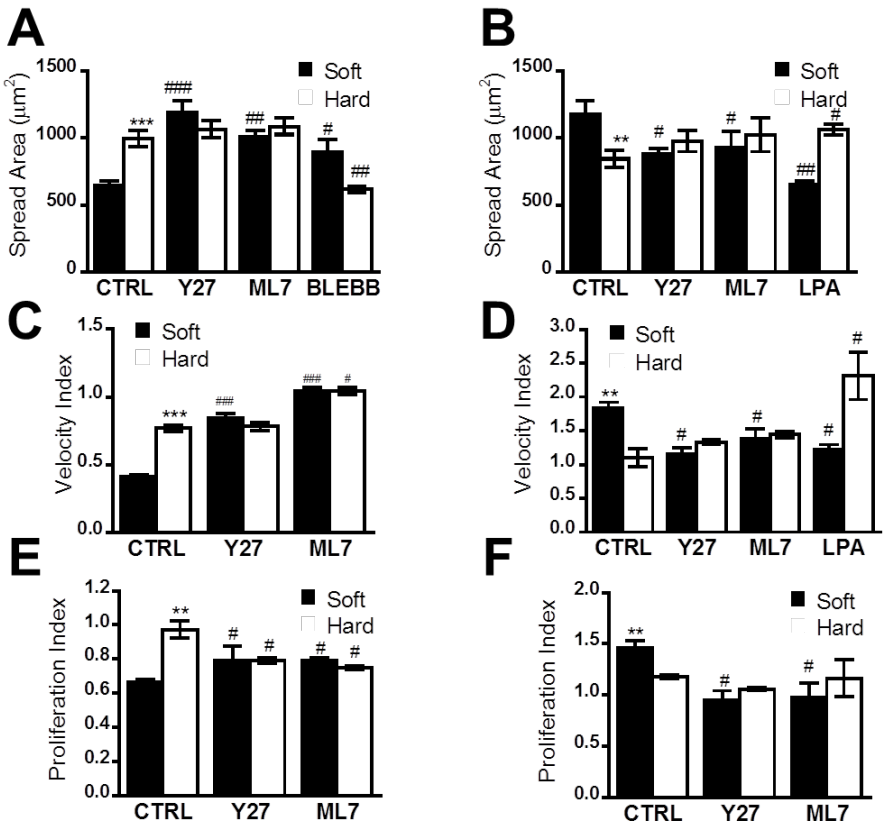

Figure 4.7 Manipulating cytoskeletal tension alters rigidity-dependent behavior. Cells were treated with 10 μM Y27632 (Y27) to inhibit Rho kinase, 10 μM ML7 to inhibit myosin light chain kinase, 50 μM blebbistatin (BLEBB) to inhibit myosin II, or 10 μM LPA to activate RhoA. (A-B) Spread area of MDA-MB-231 (A) and SKOV-3 (B) after treatment with specified inhibitor. (C-D) Motility of MDA-MB-231 (C) and SKOV-3 (D) after treatment with specified inhibitor. Velocity index is defined as velocity normalized to cell speed on collagen-coated glass. (E-F) Proliferation index of cells following overnight inhibitor treatment defined as proliferation relative to a collagen-coated glass control for MDA-MB-231 (E) and SKOV-3 (F). All values plotted as mean ± SEM of >3 independent experiments. Significance is indicated by *'s between substrate rigidities and # signs relative to untreated rigidity-matched controls. * $p<0.05$, ** $p<0.01$, *** $p<0.001$

4.3.5 Actomyosin Tension Determines Rigidity-Dependent Cancer Cell Function

To investigate how cells were interacting with the underlying substrates, we performed traction force cytometry. For control cells, both MDA-MB-231 (Fig. 4.8) and SKOV-3 (Fig. 4.9) cells exerted more force on substrates where the function was best (hard and soft, respectively). This force increase was abrogated by ROCK inhibition for

both cell lines, but had no effect on forces exerted on less preferred matrices. Inhibiting MLCK with ML7 increased force exertion in MDA-MB-231 cells on both rigidities (Fig. 4.8), whereas in SKOV-3 cells it decreased forces on the preferred soft matrix but had no effect for cells on a hard matrix (Fig. 4.9). Activation of contractility in SKOV-3 cells with LPA did increase force exertion on hard substrates as expected (Fig. 4.9), but similar to the trend observed with cell motility (Fig. 4.7D) it decreased total force exertion on soft substrates.

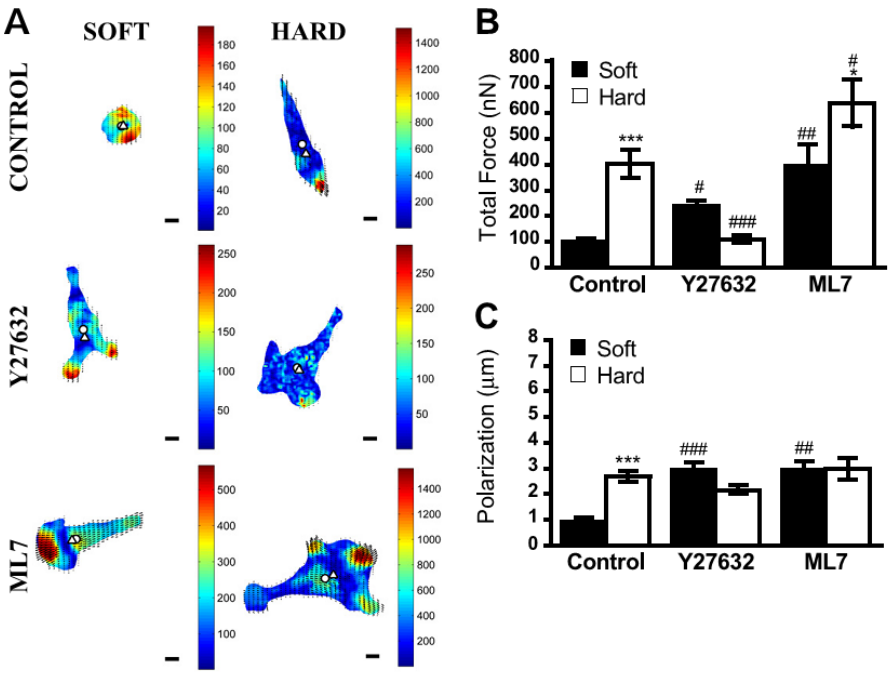

Figure 4.8 Traction force cytometry in MDA-MB-231 cells reveals multiple force profiles with similar functional outcomes. (A) Maps of traction stresses in Pa after treatment with Y27632 and ML7 for cells overlaid with markers for the cell center of mass (○) and the force-weighted center of mass (Δ). (Scale bar = 10 μm). (B) Quantification of total force exerted by MDA-MB-231 cells. (C) Polarization, defined as the distance between the cell's center of mass (circle) and the force-weighted center of mass (triangle). All values plotted as mean ± SEM of >3 independent experiments with a total of 50-150 cells per condition. Significance is indicated by *'s between substrate rigidities and # signs relative to untreated rigidity-matched controls. * $p<0.05$, ** $p<0.01$, *** $p<0.001$

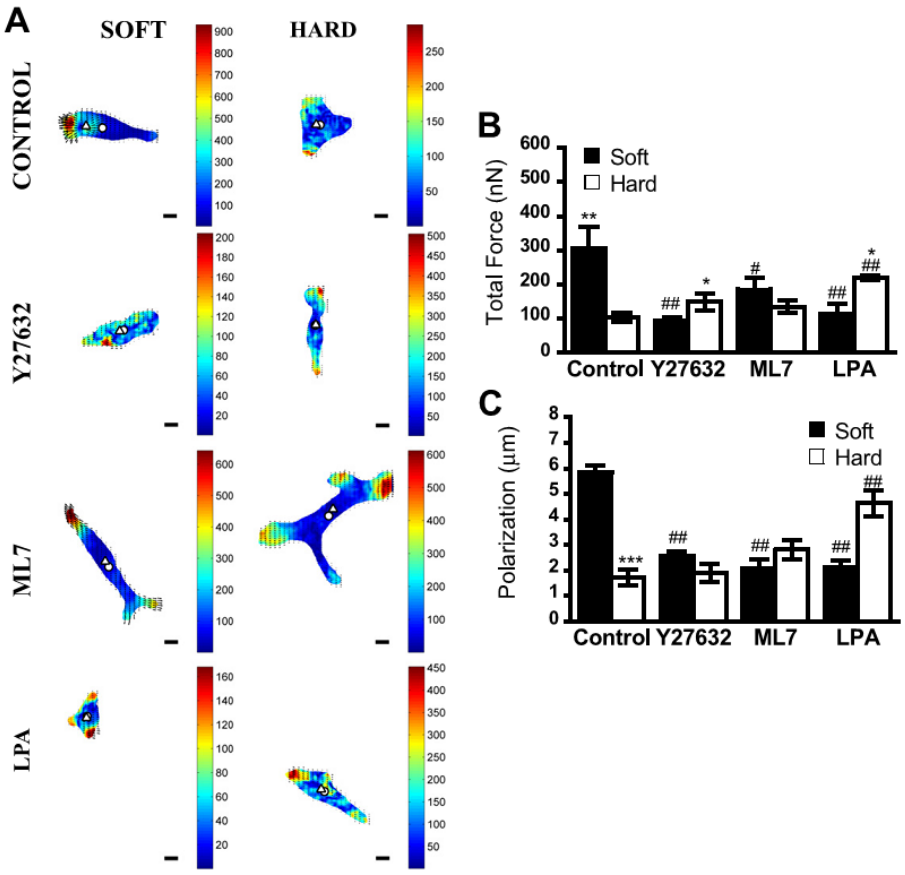

Figure 4.9 Traction force cytometry in SKOV-3 cells following inhibition of ROCK with Y27632, MLCK with ML7, and RhoA activation with LPA. (A) Maps of cell traction stresses in Pa overlaid with markers for the cell center of mass (○) and the force-weighted center of mass (Δ). (Scale bar = 10 μm). (B) Quantification of total force exerted by SKOV-3 cells. (C) Polarization, defined as the distance between the cell's center of mass (circle) and the force-weighted center of mass (triangle). All values plotted as mean ± SEM of >3 independent experiments with a total of 50-150 cells per condition. Significance is indicated by *'s between substrate rigidities and # signs relative to untreated rigidity-matched controls. * $p<0.05$, ** $p<0.01$, *** $p<0.001$

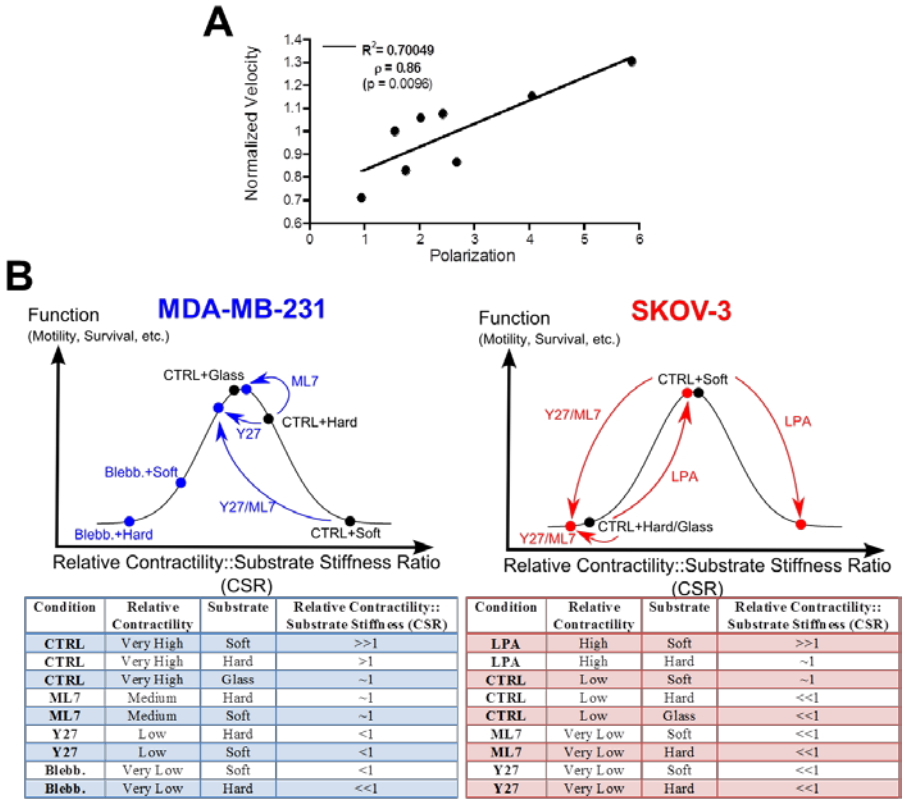

Condition	Relative Contractility	Substrate	Relative Contractility:: Substrate Stiffness (CSR)
CTRL	Very High	Soft	>>1
CTRL	Very High	Hard	>1
CTRL	Very High	Glass	~1
ML7	Medium	Hard	~1
ML7	Medium	Soft	~1
Y27	Low	Hard	<1
Y27	Low	Soft	<1
Blebb.	Very Low	Soft	<1
Blebb.	Very Low	Hard	<<1

Condition	Relative Contractility	Substrate	Relative Contractility:: Substrate Stiffness (CSR)
LPA	High	Soft	>>1
LPA	High	Hard	~1
CTRL	Low	Soft	~1
CTRL	Low	Hard	<<1
CTRL	Low	Glass	<<1
ML7	Very Low	Soft	<<1
ML7	Very Low	Hard	<<1
Y27	Very Low	Soft	<<1
Y27	Very Low	Hard	<<1

Figure 4.10 Analysis of force polarization and proposed model. (A) Force polarization correlates with cell motility. Plotting the normalized cell velocity as a function of force polarization shows a strong positive correlation between the two values with a Pearson correlation coefficient of 0.86 (p = 0.0096). (B) Proposed model of cancer cell mechanosensitivity for MDA-MB-231 cells (left) and SKOV-3 cells (right) where cell function follows a normal curve based on a ratio of relative contractility to substrate stiffness, where we define a value of 1 as an optimum for this contractility to substrate stiffness ratio (CSR). Thus, highly contractile MDA-MB-231 on glass would be near their optimum (very high::very hard) with a CSR~1, as would weakly contractile SKOV-3 cells (low::soft). If the CSR gets too high, as seen in highly contractile MDA-MB-231 on soft (very high::soft>>1) or too low as in SKOV-3 on hard (low::hard<<1), then cells may contract too strongly against the substrate to form adhesions or not have sufficient force to spread, respectively. Modulation of relative contractility would thus shift what substrate rigidity cells could function on; tabulation of these inhibitors is included below the charts.

These data demonstrated that motility could be increased both in absence of increased force or with increased force (for example, MDA-MB-231 on soft with Y27632 and ML7, respectively). To investigate this disparity, we also analyzed the polarization

distance, which describes the distribution of forces relative to the center of mass for each cell. Though following ROCK inhibition SKOV-3 cells exerted more force on hard substrates than soft, the force was not polarized (Fig. 4.9C) and motility unchanged (Fig. 4.7D). MDA-MB-231 showed that regardless of whether force increased (ML7) or not (Y27632) cells were still capable of motility (Fig. 4.7C) with proper force polarization (Fig. 4.8C). While the total amount of force exerted by each cell did not correlate with cell motility, the polarization of these forces did. After normalizing velocity to the average of each respective cell type, the Pearson correlation coefficient showed a strong positive relationship with $\rho = 0.86$ ($p<.01$) (Fig. 4.10A).

4.4 Discussion

In this paper, we sought to elucidate the determinants of how cells respond to matrix stiffness. In order to do so, we first identified cancers that show tropism to different environment rigidities. Clinicians have long noted that ovarian cancer often metastasizes to the omentum, a soft tissue predominately composed of adipocytes (88). Researchers have noted adhesion molecules (64) and soluble factors (58) that contribute to the colonization of the omentum, with similar to adaptions observed in metastatic breast cancer dissemination (89–91). Moreover, metastatic ovarian cancer cells display a more aggressive phenotype when cultured on soft substrates (84) and grow more in soft 3D gels (73). In contrast to this, an array of studies have highlighted how breast cancer advances on stiff matrices through the Rho/ROCK signaling pathway (8, 37, 92, 93). Specifically, using a subcutaneous tumor metastasis model with parental MDA-MB-231 cells, which grow more on hard matrices (59), researchers have found up to 31%

metastasis to rigid bone (89) but near 0% to softer lung tissue (91). Thus, parental MDA-MB-231 cells were chosen as a model cell line with maximal function on stiff matrices. Though some subclones of MDA-MB-231 are capable of lung metastasis even from a subcutaneous tumor, these are not believed to be the majority of the population as unsupervised clustering of microarray gene expression analysis shows the parental cell line clusters with bone metastatic subclones (Fig. 4.5). It also notable the parent MDA-MB-231 cells will typically form lung metastasis if injected via tail vein (94), however this may be largely due to passive trapping instead of active invasion.

First, we verified breast and ovarian cancer cell mechanical preference showing that when grown on soft (2.83 kPa) and hard (34.88 kPa) substrates these cells show opposite changes in proliferation, chemoresistance, and motility (Fig. 4.1) taken together as a metric of cancer cell 'malignant phenotype'. This increase in proliferation could be controlled through alterations in cell metabolism (85) or possibly through crosstalk of the RhoA contractility pathway with the Erk proliferation pathway (8). Though the increase in concomitant chemoresistance and proliferation was somewhat surprising, we hypothesize these differences come downstream of many of the same pro-growth signals responsible for the increase in proliferation. In the time scale of our experiments, cells would not have time to significantly alter drug pumps to gain resistance by simple efflux of the drug, pointing to an intracellular signaling cascade. The precise mechanisms of doxorubicin action are complex and controversial (reviewed in (95)). These include a series of direct effects from DNA binding/intercalation, interference with topoisomerase, and free radical generation. Previous studies with MDA-MB-231 cells suggest that

increased resistance on stiff matrices may be dependent on the JNK signaling cascade (96). Though others have noted that some cell lines such as lung fibroblasts become increasingly resistant to chemotherapeutics on soft matrices, so the precise mechanism by which matrix rigidity influences chemoresistance remains unclear (97). This increase in resistance could also be downstream of the increased contractile forces seen in both cases which would increase integrin signaling, a known protector against oxidative stress (98). Similarly, a variety of studies have noted that cell motility can either be increased (71, 99, 100) or decreased (101) with increasing matrix stiffness, though the reason for this discrepancy between cell lines remains unknown.

To isolate the molecules responsible for this opposite mechanical response, we performed microarray analysis of both cell lines using gene networks associated with actin myosin dynamics responsible for regulating cytoskeletal tension. We found that MDA-MB-231 expressed higher levels of contractility-associated genes such as myosin light chain, myosin heavy chain, and myosin light chain kinase (Fig. 4.5A) and that this expression was conserved regardless of matrix rigidity (Fig. 4.5B). Treatment with inhibitors of these pathways targeting either ROCK (Y27632) or MLCK (ML7) produced rigidity-independent behavior in both SKOV-3 and MDA-MB-231 cells by reducing the ability of the former to spread and migrate on soft matrices (Fig. 4.5D,F) and increasing the ability of the latter (Fig. 4.5C,E). The gain of function on soft seen after inhibition of cytoskeletal tension in MDA-MB-231 is consistent with other cells including fibroblasts (102) and was further verified by looking at proliferation, where again the inhibitors improved the ability of the cells to proliferate on soft (Fig. 4.7E).

Based on these findings we next investigated how these changes in genes associated with cytosketetal tension and their subsequent inhibition changed the forces cells transmitted to the underlying matrix by performing traction force cytometry. Both cell lines exerted approximately 100 nN of force on their less preferred substrates, increasing 2-3 folds on their preferred matrix (Fig. 4.8B, Fig. 4.9B). A similar trend has been observed where more metastatic cells exert larger traction forces than their less metastatic counterparts (74). As expected, inhibition of ROCK mitigated MDA-MB-231 force exertion on hard matrices but slightly increased it on soft-matrices (Fig. 4.8B). Treatment with MLCK inhibitor ML7 also increased forces on soft as well as hard matrices. Previous work in fibroblasts demonstrated that though ROCK and MLCK activation both increase myosin phosphorylation, they act in different spatial regions with ROCK primarily in the center and MLCK predominately at the cell periphery (103). Analysis of SKOV-3 cells further revealed decreased forces on soft after treatment with either inhibitor (Fig. 4.9). Interestingly, when treated with LPA which activates this contractility pathway SKOV-3 cells show a phenotype similar to MDA-MB-231 (Fig. 4.7D, Fig. 4.9), where cells exert higher overall force on hard and lower force on soft with higher function on the former as well. To understand how disparate levels of force transduction could produce equivalent levels of migration we instead looked at the distribution of forces, quantifying the spatial polarization of the exerted forces (Fig. 4.8C, Fig. 4.9C). This analysis revealed that though the absolute magnitude of exerted force did not correlate with cell motility, the polarization of these forces did (Fig. 4.10A).

Though the polarization of traction forces may help explain the counterintuitive motility results, it does not necessarily explain the altered spreading or proliferation observed. We hypothesize that intrinsic levels of cytoskeletal contractility positively correlate with the preferred matrix elastic modulus which allows for maximal cell function. In other words, SKOV-3 cells with low levels of contractility are more aggressive on a soft matrix whereas MDA-MB-231 cells with high levels of contractility are more aggressive on a harder matrix. Thus, taking this as a ratio of cell relative contractility to substrate stiffness there would be an optimum value. Here, we define this optimal value for contractility to substrate stiffness ratio (CSR) as one (low contractility on soft or high contractility on hard). Above this value cells may contract so strongly they cannot form stable adhesions; below this value cells may not be able to produce sufficient force to spread on the substrate. Thus, if a highly contractile cell was grown on a soft matrix the CSR would greatly exceed one leading to collapse, as seen with untreated MDA-MB-231 cells. Conversely, if a weakly contractile cell was grown on hard the CSR would be much less than one, such as untreated SKOV-3 cells. This is illustrated graphically in Figure 4.10B, where all of the various small molecules used in this study collapse directly onto this curve. For SKOV-3 cells, activation of RhoA with LPA increased contractility to allow for function on hard substrates (CSR~1), but cells became too contractile to function on soft substrates (CSR<<1). In other words, increasing contractility in these cells with low intrinsic contractility essentially reproduced the phenotype observed in the highly contractile MDA-MB-231 cells. Inhibition of contractility in SKOV-3 cells had little effect when cells were grown on hard matrices

because they were essentially already at the “minimum function.” In contrast, on soft matrices SKOV-3 cells no longer had sufficient contractility to function, similar to untreated SKOV-3 cells on hard. For the highly contractile MDA-MB-231 cells, reducing contractility with Y27632 or ML7 allowed for recovered function on soft (CSR~1). Following MLCK, but not ROCK, inhibition MDA-MB-231 increased motility on hard substrates to values seen previously on the more rigid collagen-coated glass (Fig. 4.1C, Fig. 4.7C). Though neither MLCK nor ROCK inhibition decreased MDA-MB-231 function on hard, further decreasing contractility by inhibiting their downstream target non-muscle myosin II with blebbistatin did eventually cause cell collapse (Fig. 4.7A). Taken together, these results demonstrate that intrinsic levels of cell contractility contribute to the optimal matrix for cell function. This may have implications for tissue tropism as cancer metastasizes as an equivalent contractile gene signature is seen in cells with *in vivo* tropism for soft or hard tissues (Fig. 4.6).

This hypothesis is supported by previously proposed models of focal adhesion dynamics (104, 105). In agreement with experiment, these models predict that below a certain force threshold cells will fail to form focal adhesions. This may be further influenced by force-induced conformational changes in adhesion proteins that are required for adhesion maturation (29). These models also predict that as contractile forces become exceedingly large adhesions will begin to dissolve, and that the magnitude of this critical force for adhesion dissolution scales with matrix compliance thereby directly linking intrinsic contractility to optimal matrix rigidity for cell function. This critical force where cells become too contractile to form adhesion would also be altered by

adhesion protein phosphorylation, adding an additional level of regulation to cell mechanosensitivity (104). Other cytoskeletal changes may also contribute. For instance, it was recently discovered that actin displays catch-slip bond behavior (106). Catch-slip bonds are force dependent bonds where low levels of force increase bond lifetime (e.g. strength), but after a certain critical force bond lifetimes begin to decrease (107). Thus, this optimal rigidity could also be influenced by actin-binding proteins causing differences in actin catch-slip bond behavior, similar to previous studies showing myosin II mechanosensitive recruitment is altered by varying actin crosslinkers (108). If stresses exerted by MDA-MB-231 cells were too large to be supported by the matrix it could result in decreased actin polymerization (slip regime), which would subsequently be reversed by reducing cytoskeletal tension as observed here. Alternatively, actin binding proteins may stabilize the high-affinity state of actin in SKOV-3 cells reducing the need for force to increase bond lifetimes.

In conclusion, this work demonstrates that in order for cancer to metastasize it must not only adapt to the molecular signature of the new environment but also the mechanical characteristics. Transcriptomic analysis indicated that higher intrinsic cytoskeletal tension increased malignant characteristics on hard substrates; whereas, lower basal tension allowed for increased malignancy on more compliant substrates. By further understanding the role of matrix stiffness in growth and metastasis as well as the mechanisms by which tumor cells may adapt to different mechanical properties of a secondary site, this work may provide new strategies to prevent this deadly spread.

4.5 Materials and Methods

4.5.1 Cell Culture

Human breast carcinoma MDA-MB-231 and SKOV-3 ovarian carcinoma were obtained from American Type Cell Culture (ATCC, Manassas, VA) and cultured in low glucose DMEM and McCoy's 5A obtained from Mediatech (Herndon, VA), respectively, supplemented with FBS obtained from Atlanta Biologicals (Atlanta, GA). All cells were grown in a 37°C humidified incubator with 5% CO_2.

4.5.2 Substrate Synthesis

Preparation of polyacrylamide substrates was carried out per previously published protocols (63) to obtain desired rigidities, with minor modifications. First, 0.1N NaOH was pipetted onto 12 or 18mm glass coverslips (Ted Pella, Redding, CA) and evaporated on a hot plate at 80°C. Next, coverslips were silanized by incubation for 10 minutes in 1.0% (v/v) 3-aminopropyltrimethoxysilane (TCI America, Portland, OR). Residual silane was removed by extensive rinsing in distilled H_2O, and then coverslips were activated by 30-minute incubation in 0.5% glutaraldehyde (BioRad, Hercules, CA). Mixtures of 10% acrylamide with varying amounts bis-acrylamide were used to create soft (0.03%) and hard (0.3%) substrates with elastic moduli of 2.83 kPa and 34.88 kPa, respectively. For traction force experiments, solutions were mixed with 100nm carboxylated green or red florescent nanoparticles (Invitrogen, Carlsbad, CA). Polymerization was initiated with 1:200 ammonium persulfate and 1:2000 TEMED then the solution was immediately pipetted onto the activated coverslips. To create a flat surface, this was topped with a glass slide (Ted Pella) and the entire assembly suspended to dry on a custom hanger. To

allow for cell adhesion, the photo-activated cross-linker sulfo-SANPAH (Thermo Scientific, Bremen, Germany) was diluted to 2 mg/mL in 50mM HEPES (pH 8.5), added to the top of each gel, and then activated for 5 minutes in close proximity to the UV light of a cell culture hood. Following extensive rinsing in HEPES, coverslips were incubated in 0.2 mg/mL collagen I with gentle agitation overnight at 4°C. Before use, coverslips were rinsed in PBS, UV sterilized, and equilibrated in cell media in a cell culture incubator. Microscopy indicated substrates ranged from 75 μm – 125 μm in thickness, sufficient to avoid surface effects on stiffness.

4.5.3 Traction Force Microscopy

Substrates were embedded with fluorescent nanoparticles which were used to determine cell-induced displacements from stressed and unstressed particle image with a freely available MATLAB particle tracking algorithm (MatPIV, http://www.math.uio.no/~jks/matpiv/) and used for subsequent traction force calculation (70). Traction stresses are reported as the total force (integral of force magnitude over the cell area) exerted by each cell from 3 or more independent experiments with at least 10 cells per experiment. Polarization is defined as distance between the cell center of mass and the stress-weighted center of mass (84). It is important to note that both calculations are based on the traction stress magnitude as the net sum of the forces within any cell is zero.

4.5.4 Proliferation and Chemoresistance

For these studies, cells were initially plated at 5,000 cells/cm^2. Proliferation was quantified using BrdU staining as previously described (99). After culturing cells on

substrates for 24 hours, cells were incubated for four hours with 50 μM BrdU (Sigma). Cells were washed with PBS, fixed in formaldehyde and permeabilized with 1% Triton X-100 in PBS and 4N HCl, sequentially. Finally, cells were blocked with normal horse serum, stained with 1:100 biotinylated anti-BrdU (Biolegend) followed by either streptavidin-conjugated AlexaFlour 488 (Invitrogen) or Cy3 (BioLegend), and sealed with VectaShield with DAPI (Vector Labs). Cells were quantified by comparing number of $BrdU^+$ nuclei with total number of nuclei.

For chemoresistance, cells were allowed to adhere to substrates overnight before treating with Doxorubicin (Enzo Life Sciences, Farmdingdale, New York) for 24 hours at either 2 μM (MDA-MB-231) or 0.1 μM (SKOV-3) based on preliminary titration studies. To assess viability, a standard MTT assay was utilized. Cells were incubated in 1mg/mL MTT (3-(4,5-Dimethylthiazol-2-yl)-2,5-diphenyltetrazolium bromide) for four hours in standard growth conditions. The supernatant was then removed and replaced with acidic isopropanol with 4mM HCl to solubilize insoluble purple formazan product. This product was then moved to a 96 well plate for calorimetric analysis in a DTX-800 Multimode Detector microwell plate reader (Beckman Coulter) at 620 nm absorbance with 595 nm reference value. All conditions were normalized to rigidity-matched controls.

4.5.5 Motility Quantification

Cells were plated at 10,000 cells/cm^2 and allowed to adhere overnight before labeling with NucBlue Live Cell Stain (Invitrogen, Carlsbad, CA) per manufacturer's instructions. Imaging was performed on a Nikon Eclipse Ti inverted epifluorescent microscope equipped with an environmental chamber (In Vivo Scientific, St. Louis, MO) and

maintained at 37°C and 5% carbon dioxide throughout the experiment. Images were captured every 5 minutes for 8-16 hours at 10x magnification. Image stacks were then processed in MATLAB to track the x-y coordinates of cell nuclei to determine cell velocity (84).

4.5.6 Adhesion Studies

Cells were first labeled with 2μM Calcein AM (Anaspec), a transmembrane fluorescent marker, in PBS and 2mM dextrose for 20 minutes at 37°C. Next, cells were passed per standard procedure, resuspended in media, and incubated for 30 minutes at 37°C to allow for integrin recovery before plating at 10,000 cells/cm^2. Cells were incubated for the desired time period, and then an initial florescence reading was taken on a DTX-800 Multimode Detector microwell plate reader (Beckman Coulter). The media was then replaced and a second reading was taken to quantify the amount of attached cells. Finally, cells were washed extensively and a final reading was taken. End-point cells were fixed in formaldehyde, blocked with normal horse serum, stained with 1:50 Rhodamine Phalloidin (Invitrogen), sealed with Vectashield with DAPI and imaged at 20x magnification for quantification of spread area.

4.5.7 Gene Expression Analysis

Microarray data was acquired from NCBI GEO, accession numbers GSM803625, GSM803684, GSM803743, GSM803732, GSM803778, and GSM803662. Data were processed with the MATLAB Bioinformatics Toolbox by using the GC robust multi-array average method. Fold changes of 1.5 with $p<0.05$ were considered significant. To narrow candidate genes, unique genes identified through Gene Ontology to be associated

with actin (GO:0003779, GO:0015629, GO:0030036) as well myosin (BIOCARTA_MYOSIN_PATHWAY) were selected for further analysis. Gene expression was confirmed by RT-PCR (109). High quality mRNA was isolated using Ribozol (Amresco, Solon, OH) then complimentary DNA was reverse transcribed using the BioRad iScript cDNA synthesis kit. Reverse transcriptase PCR was performed in a BioRad S1000 Thermocycler with PCR MasterMix (Promega) using following primers: *MYH9* (forward) 5`- AGGACCAGAACTGCAAGCTG-3`, (reverse) 5`-GCGCTCT TCCAAGTCAGTGA-3`, *MYL9* (forward) 5`-ACCCCACAGACGAATACCTG-3`, (reverse) 5`-AAAGGCGTTGCGAATCACAT-3`, and 18s RNA (forward) 5`-GTAACCCGTTGAACCCCATT-3`, (reverse) 5`-CCATCCAATCGGTAGTAGCG-3` for an endogenous control.

4.5.8 Modulation of Cytoskeletal Tension

Cytoskeletal tension was inhibited by treatment with either 10 μM Y27632, 10 μM ML7, or 50 μM blebbistatin to inhibit Rho kinase, myosin light chain kinase, and non-muscle myosin II, respectively. To increase cytoskeletal tension, cells were treated with 10 μM LPA to activate RhoA. Cells were treated for at least one hour before analysis and remained in the media for the duration of the experiment.

4.5.9 Statistics

All studies were performed in triplicate or more with three individual batches of substrates. Data are reported as mean ± SEM. Statistical analysis was carried out using a student's t-test or ANOVA, considering $p < 0.05$ to be significant

(***$p<0.001$,**$p<0.01$,*$p<0.05$). For inhibitor studies, # signs were used in place of * to compare samples to their untreated rigidity-matched controls.

CHAPTER 5
ALTERATIONS IN OVARIAN CANCER CELL ADHESION DRIVE TAXOL RESISTANCE BY INCREASING MICROTUBULE DYNAMICS IN A FAK-DEPENDENT MANNER[3]

5.1 Summary

Chemorefractory ovarian cancer patients show extremely poor prognosis. Microtubule-stabilizing Taxol (paclitaxel) is a first-line treatment against ovarian cancer. Despite the close interplay between microtubules and cell adhesion, it remains unknown if chemoresistance alters the way cells adhere to their extracellular environment, a process critical for cancer metastasis. To investigate this, we isolated Taxol-resistant populations of OVCAR3 and SKOV3 ovarian cancer cell lines. Though Taxol-resistant cells neither effluxed more drug nor gained resistance to other chemotherapeutics, they did display increased microtubule dynamics. These changes in microtubule dynamics coincided with faster attachment rates and decreased adhesion strength, which correlated with increased surface β1-integrin expression and decreased focal adhesion formation, respectively. Adhesion strength correlated best with Taxol-sensitivity, and was found to be independent of microtubule polymerization but dependent on focal adhesion kinase (FAK), which was up-regulated in Taxol-resistant cells. FAK inhibition also decreased microtubule dynamics to equal levels in both populations, indicating alterations in

[3]McGrail DJ, Khambhati NN, Qi MX, Patel KS, Ravikumar N, Brandenburg CP, et al. (2015) Alterations in Ovarian Cancer Cell Adhesion Drive Taxol Resistance by Increasing Microtubule Dynamics in a FAK-dependent Manner. *Sci. Rep.* 5: 1–11.

adhesive signaling are up-stream of microtubule dynamics. Taken together, this work demonstrates that Taxol-resistance dramatically alters how ovarian cancer cells adhere to their extracellular environment causing down-stream increases in microtubule dynamics, providing a therapeutic target that may improve prognosis by not only recovering drug sensitivity, but also decreasing metastasis.

5.2 Introduction

Ovarian cancer is a leading cause of cancer-related deaths in women. Due to lack of early detection techniques, more than 75% of the patients are diagnosed after the cancer spreads from the primary site (54). Though tumor debulking has proven extremely beneficial for patient survival (110), the successful use of chemotherapeutics is still critical to target the disseminated disease. The standard treatment protocol of tumor resection followed by dual agent chemotherapy consisting of platinum therapy plus Taxol (paclitaxel) have increased progression-free survival to nearly 18 months and overall survival to 38 months, though once the cancer returns it is often no longer sensitive to these chemotherapeutic agents (56). At this point, the disease rapidly progresses with progression-free survival of 3-5 months and overall survival rarely exceeding a year even with new experimental treatments (57). Thus, there exists a clear clinical need for improved understanding of recurrent disease.

This chemotherapeutic resistance could occur through a variety of mechanisms, such as increased drug efflux, increased survival signals, blocking of death signals, or even changes in cell tubulin by either binding site mutations and expression of different

isoforms (111, 112). To understand these mechanisms a series of pioneering studies have been performed by isolating Taxol-resistant populations of cancer cell lines and comparing them to their parental controls verifying many of these changes take place including over expression of the P-glycoprotein (Pgp) drug efflux pump (113), alterations in stress response and survival cascades (114), increased microtubule dynamics (115), alteration in expression of tubulin isoforms (116), and mutations to Taxol binding sites (117). Of these studies, the former two were carried out on cells isolated to have super-physiological resistance to Taxol with IC_{50} values in excess of 1 μM. In contrast, the latter studies that observed altered microtubules isolated cells by slowly ramping the Taxol concentration to nanomolar concentrations relevant in the clinic (118) produced an IC_{50} of approximately 20-45 nM, over two orders of magnitude more sensitive.

Though chemoresistance is a key hurdle in the treatment of ovarian cancer, the majority of cancer deaths are ultimately caused by metastatic spread of the disease to distant sites (119). Ovarian cancer typically shows extensive metastasis following treatment with Taxol, and Taxol-resistant cell lines are more metastatic in mouse xenograph models (120). In order to metastasize, ovarian cancer cells must first detach from the primary tumor. After detaching, the cells disseminate through the peritoneal cavity before re-adhering to a secondary site, often the omentum. This adhesion represents the first rate-limiting step in ovarian cancer progression (121). Cell adhesion is controlled both by extracellular integrin domains which bind to the extracellular matrix (ECM), as well as intracellular focal adhesion adapter proteins such as paxillin and vinculin which act as linkers between the transmembrane integrins and internal

cytoskeleton (122). Integrin expression has been linked to progression in a variety of cancers, causing increased metastasis, increased tumor survival, and decreased patient prognosis (123). In ovarian cancer, expression of β1 integrin has been linked to ovarian cancer invasion and metastasis (124, 125). Additionally, specific integrin heterodimers α4β1 and αvβ5 have been shown to increase metastasis and proliferation, respectively (64, 126). Moreover, previous studies have demonstrated a bi-directional link between adhesion signaling and the microtubule dynamics targeted by Taxol where focal adhesion signaling can alter microtubules (127, 128) and microtubules can alter adhesion dynamics (129). Based on this, we hypothesized that ovarian cancer resistance to Taxol may lead to alterations in adhesion dynamics, which may contribute to the rapid progression following disease recurrence.

To test this hypothesis, we isolated Taxol-resistant cell lines from parental ovarian cancer cell lines SKOV3 and OVCAR3 using a metronomic approach by repeated exposure to clinically relevant concentrations of Taxol (118) with intermediate recovery periods similar to therapeutic administration. This produced IC_{50} values of 20-45 nM, equivalent to the latter studies that observed alterations in microtubule dynamics (127, 128). Initial studies suggested that these changes were not due exclusively to changes in drug efflux or other direct pro-survival adaptions but Taxol-resistant cells did show increased microtubule dynamics, including increased microtubule growth rates and decreased levels of polymerized tubulin. Analysis of attachment kinetics revealed that Taxol resistant cells adhered nearly two-fold faster, which correlated with higher integrin expression. In contrast, analysis of adhesion strength using a centrifugal-force based

adhesion assay revealed Taxol-resistant cells attached less strongly to the ECM. To understand the decreased adhesion strength despite increased attachment rate and integrin expression we stained for intracellular focal adhesions and found that Taxol resistance dramatically reduced both their size and number. Finally, we sought to determine if these changes in adhesion and microtubule polymerization occurred independently or if they were causally related. Though chemical perturbation of microtubule polymerization did not alter adhesion strength, inhibition of focal adhesion kinase (FAK) mitigated adhesive differences between parental and Taxol-resistant cells. Additionally, microtubule dynamics were also suppressed following FAK inhibition in both cell lines producing statistically identical growth rates in both the parent and Taxol-resistant cells. These results highlight a novel mechanism of ovarian cancer chemoresistance, and may provide therapeutic targets such as focal adhesion kinase to both slow metastatic cell engraftment and increase chemosensitivity.

5.3 Results

5.3.1 Taxol resistance is independent of drug efflux and does not confer additional chemoresistance

After establishing populations of SKOV3 and OVCAR3 ovarian cancer cell lines capable of growing in Taxol, we first verified this correlated with an increase in IC_{50} by treating cells with Taxol at varying concentrations for 72 hours. Consistent with previous reports(130), SKOV3 and OVCAR3 parental populations (abbreviated as SKOV3-P and OVCAR3-P) showed IC_{50} values of 2.3 ± 0.3 nM and 4.1 ± 1.8 nM, respectively, which were increased an order of magnitude in the Taxol-resistant subpopulations (abbreviated

as SKOV3-T and OVCAR3-T) to 22.1 ± 3.0 nM and 45.5 ± 4.9 nM (Fig. 5.1A). While parent populations show dose-dependent decreases in viability, Taxol-resistant cells

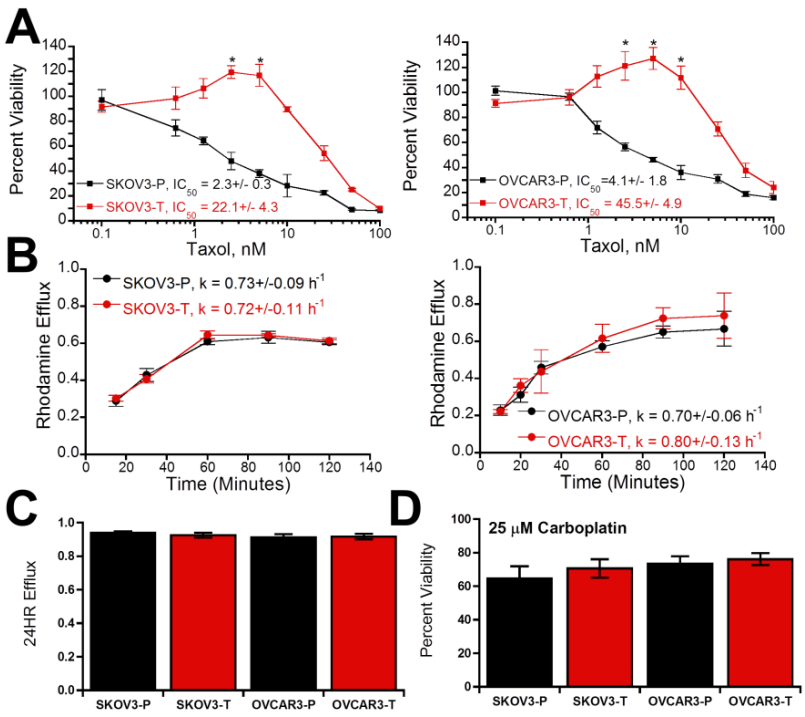

Figure 5.1 Generation of Taxol-resistant populations and analysis of potential resistance mechanisms. (A) Viability of parental (-P) and Taxol-resistant (-T) populations of SKOV3 and OVCAR3 ovarian cancer cells in after incubation in varying concentrations of Taxol (* is significantly greater than solvent treated control, $p<0.05$, N=3). (B) Time-dependent rhodamine efflux over initial two hours was used to calculate efflux rates (k), which showed no significant difference among cell populations (N=3). (C) Long-term 24 hour efflux showed no significant difference between cell populations (N=3). (D) Viability after incubation with 25μM Carboplatin relative to solvent-treated control. Values given as mean ± SEM.

showed significantly increased viability at concentrations of 5-10 nM Taxol beyond which viability decreased. To begin to investigate the mechanism of this resistance, we next evaluated the ability of the cells to efflux Rhodamine 123 as a model drug (Fig. 5.1B-C), as both Taxol and Rhodamine 123 are substrates for P-glycoprotein mediated

efflux.(131) Evaluation of both efflux kinetics (Fig. 5.1B) and total efflux after twenty four hours (Fig. 5.1C) demonstrated no significant changes with Taxol resistance. Finally, to see if changes were the product of other pro-survival adaptions we assayed the ability of cells to survive in 25 μM Carboplatin and found no significant change in Carboplatin resistance in Taxol resistant subpopulations (Fig. 5.1D). These results suggest that alternative mechanisms must be underlying this Taxol resistance.

5.3.2 Microtubule Alterations in Taxol-resistant cells

Based on the increase in viability seen with low-dose Taxol in Taxol-resistant cells, we next evaluated if Taxol-resistant cells displayed enhanced microtubule dynamics. First, we performed a microtubule regrowth assay where microtubules were depolymerized with nocodazole and then allowed to regrow following washout (Fig. 5.2A). By 10 minutes SKOV3-P cells had begun to nucleate whereas microtubule networks had already begun to form in SKOV3-T cells, which was not seen until 30 minutes in the SKOV3-P cells. To verify this difference in live cells in absence of chemical perturbation we transfected cells with fluorescent end-binding protein (mApple-EB3) which binds to the growing plus ends of microtubules allowing for quantification of microtubule growth rates (Supp. Vid. 1-2)(132). Not only were microtubule growth rates significantly faster in the SKOV3-T cells ($p<0.0001$, Fig. 5.2B), but they also showed an increased number of growing plus ends ($p<0.0001$, Fig. 5.2C), indicating significantly increased dynamics. Finally, we performed a microtubule pelleting assay to determine if the cells natively had different levels of polymerized microtubules revealing SKOV3-P cells had significantly more polymerized tubulin than SKOV3-T cells (Fig. 5.2D).

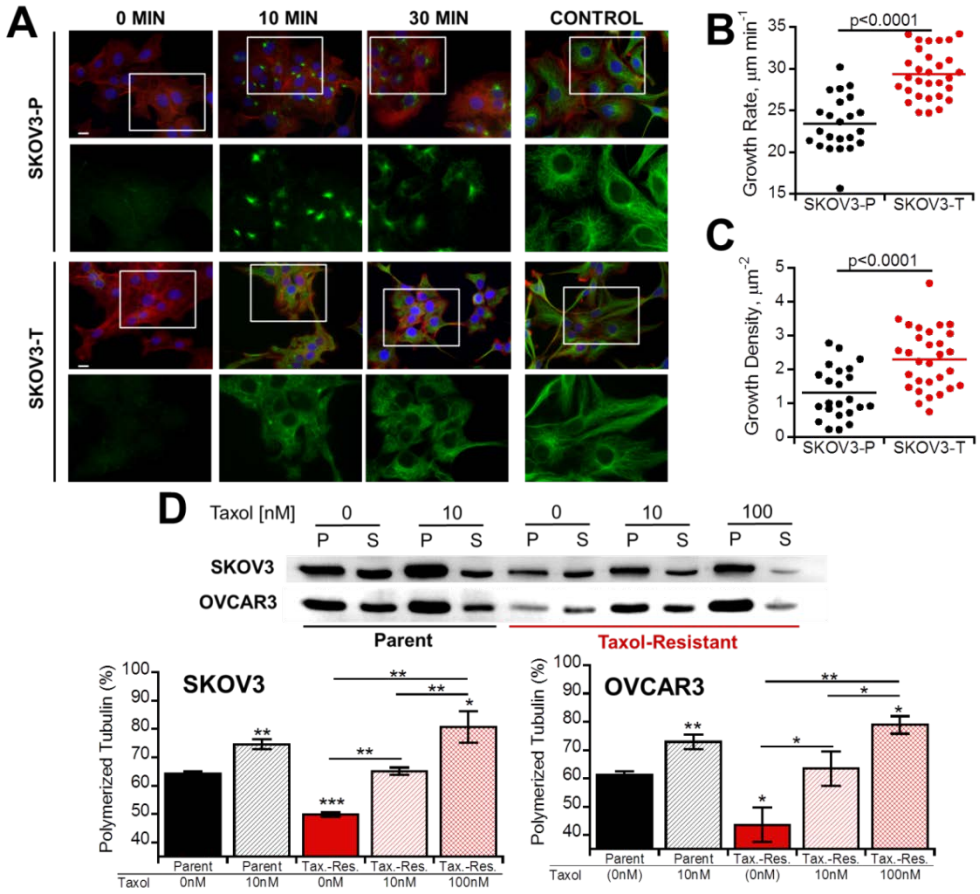

Figure 5.2 Microtubule dynamics are increased in Taxol-resistant cells. (A) Microtubules were depolymerized with nocodazole for four hours and then drug was washed out for indicated time at which point cells were immunostained for microtubules (green), actin (red), and nuclei (blue). Scale bar = 10 µm. (B-C) Live-cell microtubule dynamics as determined from plus-end tracking of fluorescent mCherry-EB3, to quantify growth rate (B) as well as growth density (C), defined as the total number of growing ends normalized to cell area. Each dot represents the average of over 100 tracked plus-ends from one cell collected from a total of 4 independent experiments. (D) Taxol-resistant cells have less polymerized tubulin. Cells were lysed following 4 hour pretreatment with Taxol and separated into polymerized (P) and soluble (S) tubulin fractions for Western blot analysis. Percent polymerized tubulin was quantified as polymerized tubulin divided by the sum of polymerized and soluble tubulin. Values given as mean ± SEM; significance is indicated relative to control parent population unless otherwise noted, *P<0.05, **P<0.01,***P<0.001.

Treating SKOV3-T with 10 nM Taxol returned levels of polymerized tubulin to those of parental cells, while 100 nM Taxol was required to increase tubulin polymerization above

parent levels. With similar findings in OVCAR3-T cells, these results indicate that Taxol-resistant cells have decreased polymerized microtubules and increased microtubule growth rates consistent with previous reports (115–117).

5.3.3 Increased attachment kinetics correlate with integrin expression in Taxol-resistant cells

Several recent studies have shown a strong link between microtubules and focal adhesions (127, 133, 134). Thus, we sought to determine if changes in Taxol sensitivity produced alterations in cell adhesion. To do so, we first analyzed the attachment kinetics as cells initially attached to a collagen-coated surface (Fig. 5.3A). Though SKOV3 cells adhered faster overall, the Taxol-resistant populations both adhered faster than their parental counterparts (Fig. 5.3B). This increase in attachment rate correlated with increased spreading (Fig. 5.4A) and was conserved on both fibronectin and Matrigel coated surfaces (Fig. 5.4B). Due to previous studies linking increased integrin expression and chemoresistance (123). we hypothesized the increased attachment rate in Taxol-resistant cells may be due to integrin overexpression. Surface integrin expression was quantified using flow cytometry for β1 integrin responsible for binding to collagen I (Fig. 5.3C). For both cell lines, surface integrin expression was increased in Taxol-resistant clones, though SKOV3 cells expressed higher overall levels of β1 integrin (Fig. 5.3D). These results directly correlated with observed attachment kinetics, showing a positive linear relationship between β1 integrin expression and attachment rate (R^2 = .90, Pearson's correlation coefficient ρ = 0.95, Fig. 5.3E). However, due to basal variations between SKOV3 and OVCAR3 neither attachment rate (R^2 = 0.03, Fig. 3F) nor integrin

expression (R^2 = 0.21, Fig. 5.3G) correlated with IC_{50}, suggesting though this may be a contributing factor it was not a primary mechanism of Taxol resistance.

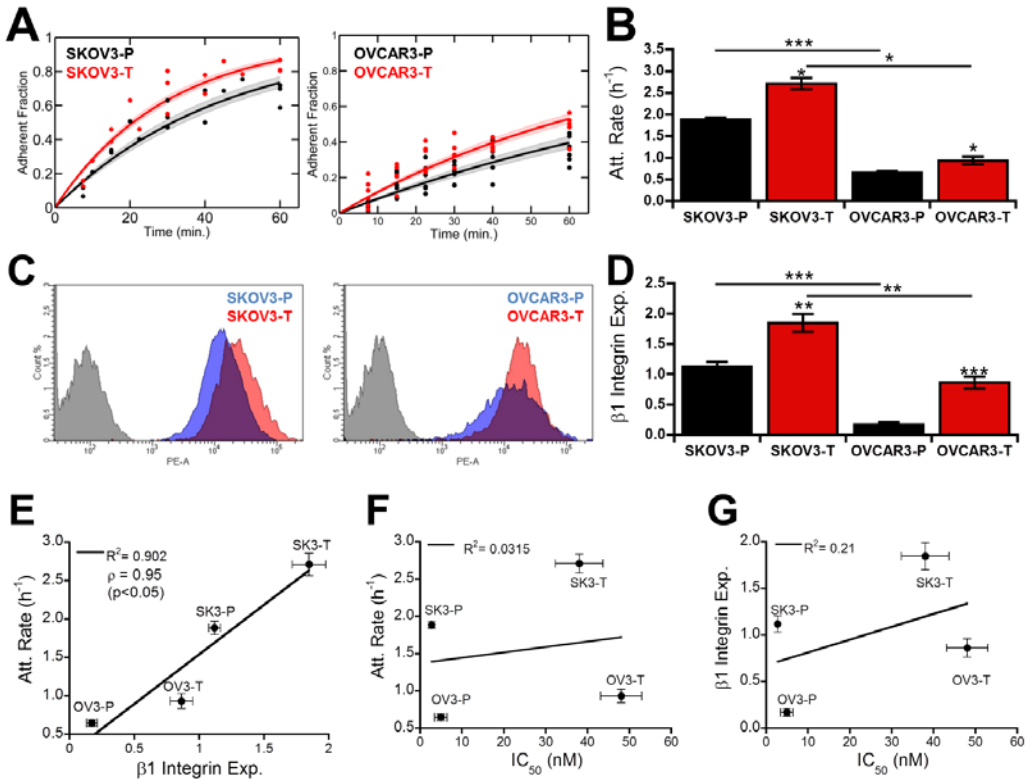

Figure 5.3 Taxol resistance alters attachment kinetics through β1 integrin. (A) Cells fluorescently labeled green with Calcein AM were plated for specified period of time before removing non-adherent cells and quantifying the adherent fraction fluorometrically. Individual dots represent independent experiments; solid lines are fit curves with shaded region representing the 95% confidence interval. (B) Attachment rate determined from regression of each independent experiment. (C-D) Representative flow cytometry intensity histograms for cells labeled with PE-CD29 (β1 integrin) (C) as well as mean fluorescence intensity of surface β1 integrin (D), normalized to the mean of each individual experiment to account for any variations in laser intensity (N = 3). (E) Surface expression of β1 integrin shows direct linear correlation with adhesion rate (Pearson correlation coefficient β = 0.95, R2 = 0.902). (F-G) Neither β1 integrin (F) or adhesion rate (G) correlated with Taxol sensitivity. Values given as mean ± SEM; significance is indicated relative to control parent population unless otherwise noted, *P<0.05, **P<0.01,***P<0.001.

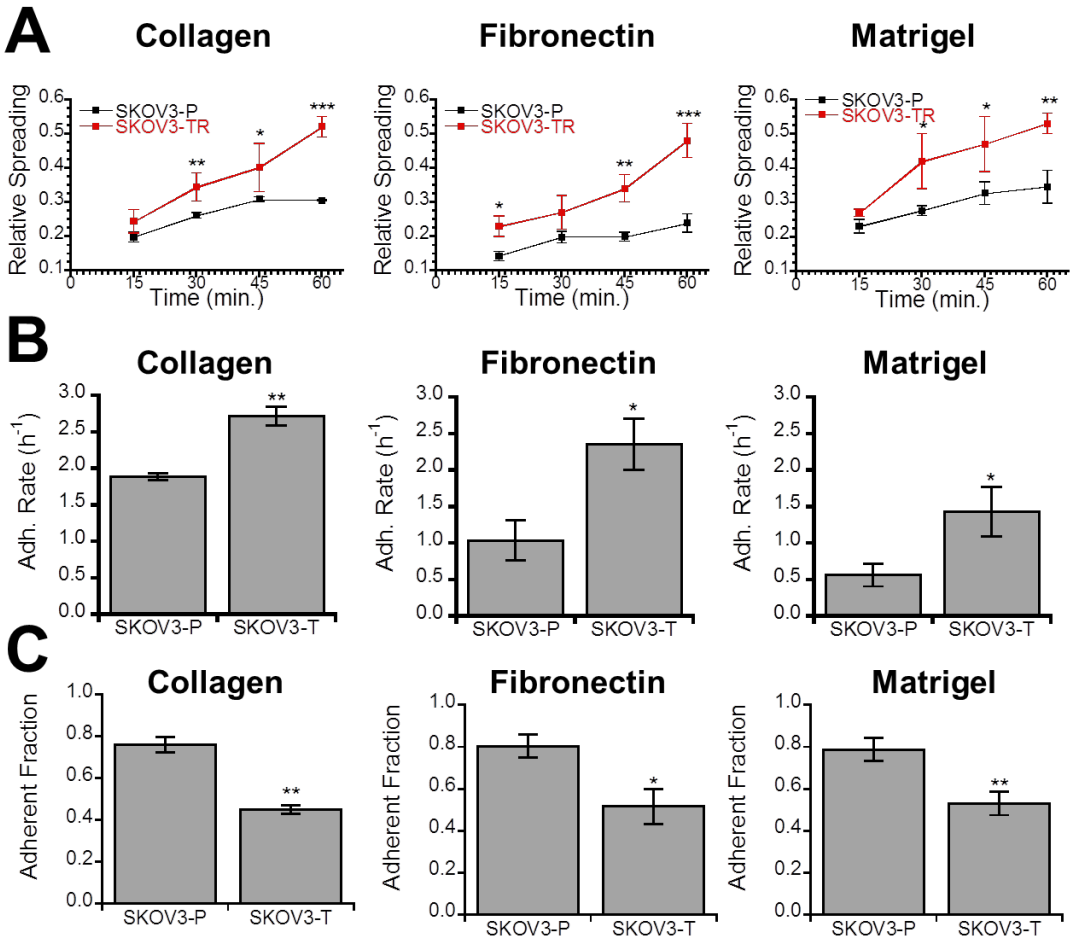

Figure 5.4 Adhesion differences are conserved across multiple ECMs. Plates were coated either with 10 μg/mL Type I Collagen, 10 μg/mL fibronectin, or 100 μg/mL Matrigel and blocked with 1% heat-denatured BSA. (A) Cell spreading was analyzed by plating Calcein-labeled cells for specify period of time before fixing and staining F-actin with Rhodamine Phalloidin and nuclei with DAPI to quantify cell area. (B) Adhesion rate to various ECMs shows some baseline variation based on ECM, but increased adhesion rate in Taxol-resistant cells was conserved on all tested molecules. (C) Adhesion strength was also tested on all three ECMs with Taxol-resistant cells being more weakly adherent in all cases and no significant dependence on ECM. Values reported as mean ± SEM of three independent experiments, *P<0.05, **P<0.01,***P<0.001.

5.3.4 Taxol resistance decreases adhesion strength through diminished focal adhesion formation

The increased integrin expression suggested that adhesion strength would be increased in Taxol-resistant cells, but inhibition of tubulin polymerization has previously been shown to effect focal adhesion formation and steady state adhesion strength (135, 136). Since Taxol-resistant cells displayed decreased polymerized tubulin, we next quantified their adhesion strength using a centrifugal-force based adhesion assay to test if the integrin up-regulation in Taxol-resistant clones led to increased adhesion strength. After adhering overnight, the detached fraction following centrifugation in Taxol-resistant population was nearly twice that of their parental lines (Fig. 5.5A), despite integrin overexpression. This result correlated well with changes in IC_{50} (Fig. 5.5B) suggesting alterations in Taxol sensitivity may be related to alterations in adhesion strength.

Based on this, we hypothesized that Taxol resistance was decreasing focal adhesion formation; therefore, focal adhesions were visualized by staining for the focal adhesion protein paxillin (Fig. 5.5C). Cells from both parent populations contained large focal adhesions distributed throughout the cell periphery. In the Taxol-resistant populations these focal adhesions were smaller and more disperse. Quantification of paxillin localized to focal adhesions showed significant reductions in both Taxol-resistant cell lines compared to their respective parent lines (Fig. 5.5C). Similar results for the focal adhesion protein vinculin were observed in OVCAR3 cells; however neither population of SKOV3 showed significant vinculin positive focal adhesion expression with only

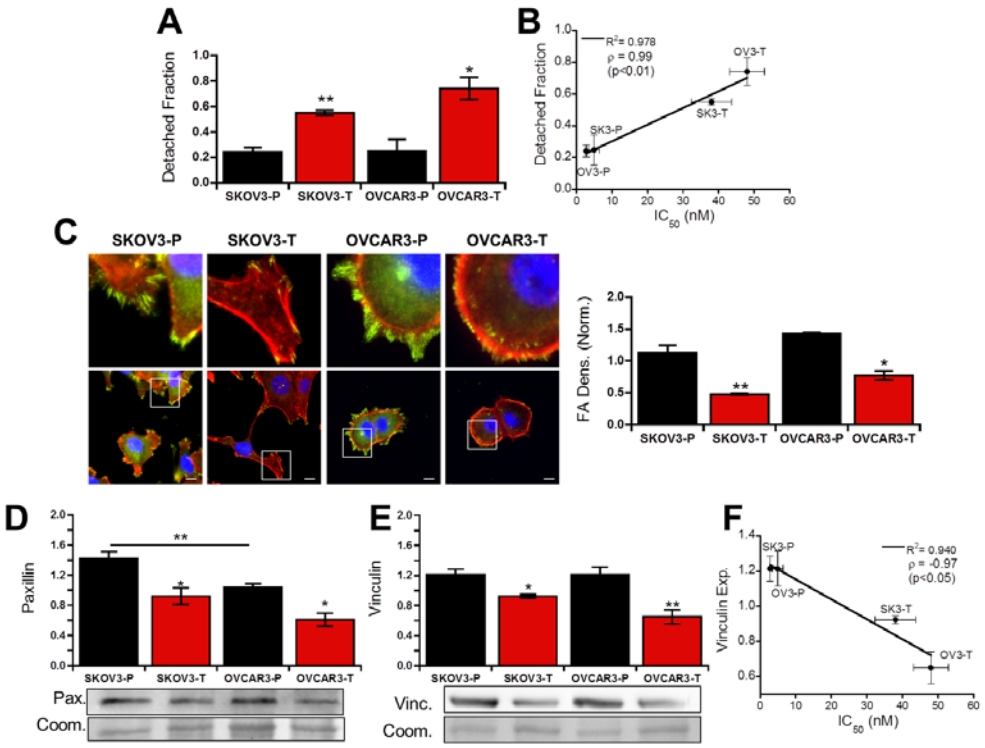

Figure 5.5 Taxol resistance decreases adhesion strength by altering focal adhesions. (A) Detached fraction of parent (-P) and Taxol-resistant (-T) cells allowed to adhere overnight before detachment by centrifugal force shows significantly decreased adhesion strength in Taxol-resistant clones ($p<0.01$,N=4). (B) Detached fraction of cells correlates directly with IC50 values ($p<0.01$), Pearson correlation coefficient $\rho = 0.99$. (C) Immunofluorescent micrographs of cells labeled for paxillin (green), F-actin (red), and nuclei (blue) with zoomed versions of highlighted areas. Scale bar = 10 μm. Focal adhesion density was quantified as the integrated density of segmented focal adhesions relative to cell area (N=3). (D-E) Total paxillin (D, N=4) and vinculin (E, N=3) expression, quantified by Western blot normalized to total protein, is decreased in Taxol-resistant cells but is also dependent on cell line. For total protein from Coomassie, a representative region of the quantified area is shown. (F) Vinculin expression inversely correlates with IC50 values ($p<0.05$), Pearson correlation coefficient $\rho = -0.97$.

disperse staining (Fig. 5.6A). Analysis of total paxillin expression by Western blot showed decreased expression in Taxol-resistant cells (Fig. 5.5D). Paxillin levels were equivalent between SKOV3-T and OVCAR3-P even though the latter exhibits significantly higher adhesion strength (Fig. 5.5A), indicating the decreased adhesion

strength is not solely due to decreased paxillin expression. Surprisingly, despite the lack of vinculin-containing adhesions in SKOV3 cells, expression of vinculin agreed best with adhesion strength results (Fig. 5.5E) and also inversely correlated with Taxol sensitivity (Fig. 5.5F).

While total vinculin expression does seem to agree with adhesion strength, the disparate distribution of vinculin between SKOV3 and OVCAR3 cells suggests alternative molecules may be a larger determining factor. Since vinculin has been shown to inhibit paxillin interactions with focal adhesion kinase (FAK)(137), we also stained for FAK phosphorylated at Y397 (FAKp397). In parental cells FAKp397-positive adhesions tended to be larger but less numerous than paxillin-positive focal adhesions, whereas in Taxol-resistant cells FAKp397-positive adhesions tended to appear as more nascent adhesions both smaller in size and more disperse (Fig. 5.6B). Taxol-resistant cells also expressed higher overall levels of FAKp397 by Western blot (Fig. 5.6C). Consistent with the idea that parental cells tend to have larger more mature adhesions whereas Taxol-resistant cells tend to have more nascent adhesions which are known to exert larger forces,(138) traction force cytometry revealed that Taxol-resistant cells exert nearly 2-fold larger forces than their parental counter parts (Fig. 5.7). These results demonstrate that the decreased adhesion strength coincides with smaller nascent focal adhesions which exert higher forces as a result of changes in expression of adhesion proteins. These changes agree with decreased vinculin expression in Taxol-resistant cells, but do not correlate with paxillin expression or integrin expression suggesting additional intracellular signaling cascades contribute to the decreased adhesion strength.

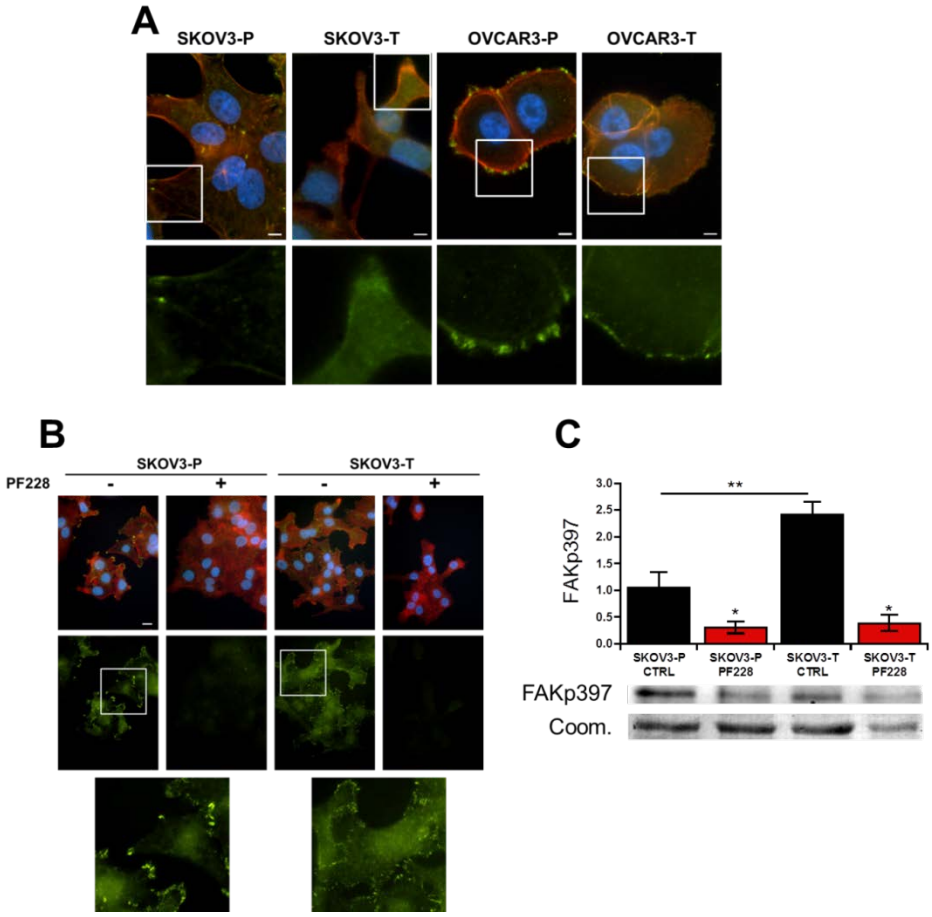

Figure 5.6 Alterations in focal adhesions in Taxol-resistant cells. (A) Cells were stained for vinculin (green), actin (red) and nuclei (blue). While OVCAR displayed several large vinculin positive adhesions in the parental population and small vinculin positive adhesions in the Taxol-resistant population, only parental SKOV3 cells showed any formation of vinculin adhesions with diffuse staining in the Taxol-resistant population. (B) Cells were stained for FAKp397 (green), actin (red) and nuclei (blue). Consistent with other stains, this revealed large focal adhesions in the parent population with smaller focal adhesions in the Taxol-resistant cells coinciding with an increase in diffuse cytoplasmic signal. Staining was largely negligible after four hour incubation with 10 μM PF228. Scale bars = 10 μm. (C) Increased FAKp397 in Taxol-resistant cells demonstrated by Western blot, with inhibition to equivalent levels following four hour incubation with 10 μM PF228. Values reported as mean ± SEM of three independent experiments. Significance indicated relative to untreated control unless otherwise noted; *P<0.05, *P<0.01.

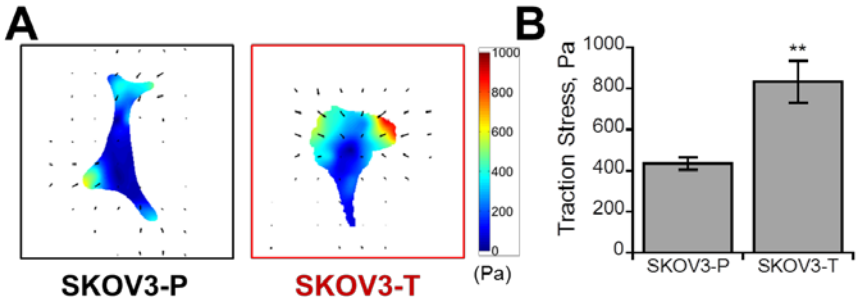

Figure 5.7 Increased Traction Forces in Taxol-resistant cells. (A) Heat maps of traction stresses in Pascals show larger forces in Taxol-resistant cells. (B) Quantification of peak stress shows a two-fold increase in traction forces as quantified by average peak traction stress (N=3). Values given as mean ± SEM; *P<0.05, **P<0.01,***P<0.001.

5.3.5 Alterations in adhesion strength are dependent on focal adhesion kinase and upstream of microtubule dynamics

We next sought to determine what intracellular signaling cascades could be responsible for the alterations in adhesion strength and microtubule dynamics. Based on our observations, we hypothesized that either (1) alterations in microtubule dynamics were decreasing focal adhesion formation or (2) decreased focal adhesion formation was altering microtubule dynamics. To determine which mechanism was ultimately altering the adhesive strength of Taxol-resistant cells we chemically modified both pathways and repeated the adhesion strength assay. First, to test if the decreased adhesion strength was due to increased microtubule dynamics we pre-incubated cells with either Taxol to stabilize (Fig. 5.8A) microtubules or nocodazole to depolymerize microtubules (Fig. 5.8B) and repeated the adhesion strength assay. In both cases, there was no change in the adhesive strength of either the parent or Taxol-resistant cells across a wide array of concentrations indicating the changes in adhesion strength are not due to microtubule dynamics. To investigate if these changes were due to altered focal adhesion signaling we

inhibited the increased FAK phosphorylation observed in Taxol-resistant cells with PF228 (Fig. 5.6B-C), which has been shown to block focal adhesion turnover(139). In parental cells FAK inhibition did not alter adhesion strength at any tested concentration (Fig. 5.8C, black line). In contrast to this, the detached fraction was significantly lower than untreated control for all concentrations in Taxol-resistant cells and no longer significantly different than the parental cell line for all concentrations greater than 5 μM (Fig. 5.8C, red line). To probe if FAK inhibition could also reverse changes in attachment kinetics, we allowed cells to adhere for 30 minutes after pretreatment with PF228 and found FAK inhibition significantly reduced Taxol-resistant cell attachment with equal fractions of both parental and Taxol-resistant cells adhering in this short time scale (Fig. 5.8D). Finally, to verify that changes in adhesive signaling were the up-stream cause we repeated the microtubule plus-tip tracking with EB3 after FAK inhibition and found a significant ($p<0.001$) decrease in microtubule growth rate for both SKOV3-P and SKOV3-T cells (Fig. 5.8E). Notably, this produced equivalent growth rates in both cell populations through a larger growth rate decrease in the Taxol-resistant cells (45% vs. 28%). Taken together, these results suggest a model where changes in focal adhesion signaling cause alterations in microtubule dynamics leading to increased resistance to microtubule-stabilizing drugs such as Taxol.

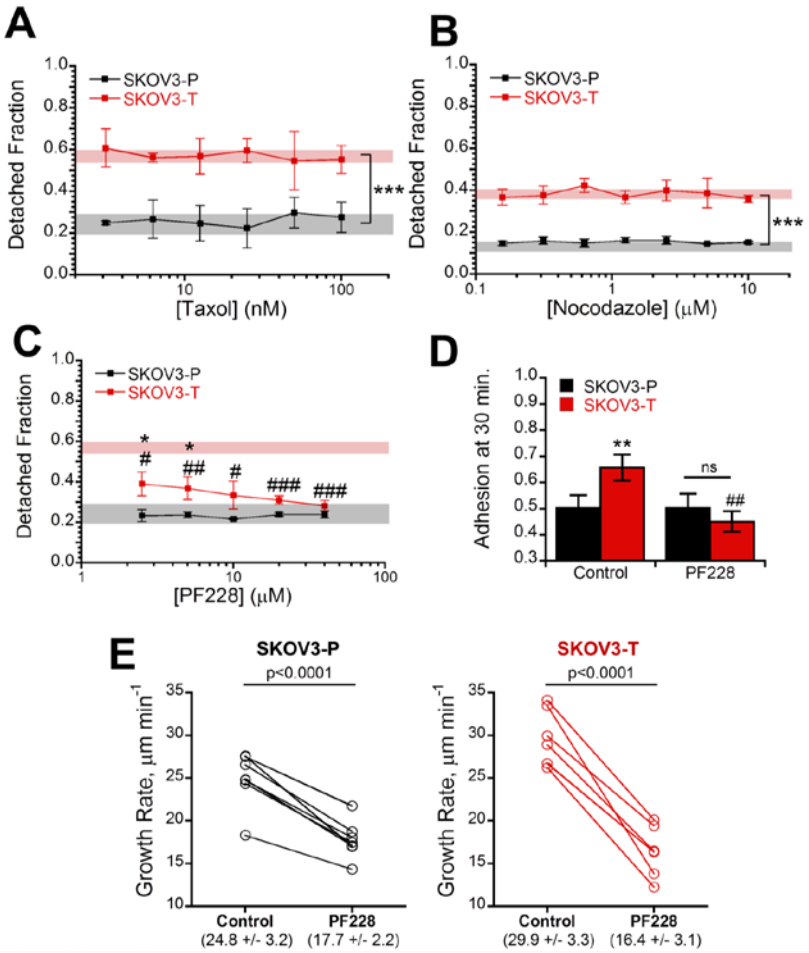

Figure 5.8 Alterations in in adhesion and microtubule dynamics in Taxol-resistant cells are reversible with FAK inhibition. (A) SKOV3 parent (-P) and Taxol-resistant (-T) were pre-incubated with Taxol for 4 hours to stabilize microtubules before repeating the adhesion strength assay and displayed no change from the untreated controls (shaded region). (B) The adhesion strength assay was repeated using 4 hour nocodazole pre-treatment to depolymerize microtubules. In order to prevent changes from increased Rho activity upon nocodazole upon washout the experiment was carried out in the drug-containing media instead, producing a slightly higher baseline for SKOV3-T. (C) To inhibit focal adhesion signaling cells were pre-incubated with focal adhesion kinase inhibitor PF228 for 4 hours before running the adhesion strength assay demonstrating selective recovery of adhesion force in Taxol-resistant cells relative to their untreated controls (red shaded region) to become equivalent with parent control cells (gray shaded region). (D) To determine the effects of FAK inhibition on attachment kinetics, cells were pre-incubated with 10 μM PF228 and allowed to adhere for 30 minutes revealing FAK inhibition decreased attachment kinetics in Taxol-resistant cells (N=3). (E) Cells transfected with mCherry-EB3 were imaged and then treated with 10 μM PF228 for four hours before re-imaging revealing a significant ($p<0.0001$) decrease in both parent and Taxol-resistant cells to a statistically equal value. Values listed in parenthesis are given as mean ± std. All other values given as mean ± SEM; significance is indicated relative to matched parent population with *'s and relative to solvent treated control #'s. *P<0.05, **P<0.01,***P<0.001.

5.4 Discussion

Taxol is clinically effective in treating a variety of cancers, including breast and ovarian cancer, but eventual acquired resistance limits its long-term efficacy. Some studies suggest this may be through increased drug efflux or altered survival signals (111, 114). For instance, early evidence showed Taxol resistance can cause over expression of the P-glycoprotein (Pgp) drug efflux pump (113). Indeed, highly Taxol resistant populations of ovarian cancer show increased expression of multiple drug resistance pumps(140). Despite this extremely promising *in vitro* data, clinical trials of drug pump inhibitors have failed to meet general clinical end points (141). High early Pgp expression is an indicator of poor prognosis; therefore targeting of these patients with high de novo expression may yield more positive results (142).

One potential reason for the lack of success of drug pump inhibitors is many studies on chemoresistance were conducted in populations resistant to concentrations much greater than occur therapeutically (118). Resistance to such high concentrations may activate alternative chemoresistance mechanisms that would not be relevant in the clinic. Moreover, isolation of Taxol-resistant ovarian cancer cells with high initial Taxol concentrations confers cross-resistance to other chemotherapeutics that is minimized when isolated with initially lower concentrations (143). The Taxol-resistant cells isolated here using our metronomic approach of repeated exposure and withdrawal of clinically relevant concentrations of Taxol (118) produced lines with IC50 values of 20-50 nM. These Taxol resistant populations that showed no difference in ability to efflux Rhodamine 123 (Fig. 5.1B-C), which is also effluxed by the multidrug transporter P-

glycoprotein responsible for Taxol efflux (131). Moreover, the lack of change in resistance to carboplatin suggests the resistance is not due to either increased survival signals or decreased sensitivity to death signals (Fig. 5.1D). Another potential mechanism lies in modifications to microtubule isoforms and dynamics (144). Several of these studies, like ours, used less resistant clones with IC_{50} values in the 20-40 nM range (115–117). In agreement with their findings, we found decreased levels of polymerized tubulin and increased microtubule dynamics within our Taxol-resistant cells (Fig. 5.2). Treatment of Taxol-resistant cells with 10 nM Taxol returned level of polymerized tubulin to those of untreated parental populations (Fig. 5.2D). This result may explain the increased viability in Taxol-resistant cells that peaks at similar Taxol concentrations (Fig. 5.1A), which could act to stabilize the hyper-dynamic microtubules in Taxol-resistant cells to normal levels. In the absence of Taxol, the resistant cells' microtubules may not have the stability necessary to properly form the mitotic spindle for division, which is then recovered by low-dose Taxol.

Since microtubules have been shown to regulate focal adhesion assembly and disassembly (129) and focal adhesions have also been shown to alter microtubule dynamics (127, 128), we hypothesized that Taxol resistance may result in altered cell adhesion. While both attachment kinetics (Fig. 5.3A-B, Fig. 5.4B) and strength (Fig. 5.5A, Fig. 5.4C) were altered, only adhesion strength correlated with Taxol sensitivity (Fig. 5.3F, Fig. 5.5B), whereas attachment kinetics were more strongly correlated with integrin expression (Fig. 5.3E). As expected, this decreased adhesion strength coincided with smaller focal adhesions in Taxol-resistant cells (Fig. 5.5C, Fig. 5.6). Early studies

into the effects of microtubules on focal adhesions demonstrated that microtubules are critical for focal adhesion disassembly and their stabilization with Taxol results in increased focal adhesion size (145). Consistent with this, parental cells with more polymerized and less dynamic microtubules (Fig. 2) displayed larger focal adhesions (Fig. 5.5C, Fig. 5.6). Recent studies have also shown focal adhesion dissolution may be facilitated by CLASP proteins which bind microtubule plus-ends to adhesion sites where they secrete MMPs to degrade the underlying matrix expediting focal adhesion turnover(146). The higher density of microtubule plus-ends in Taxol-resistant cells (Fig. 5.2C) may thus expedite focal adhesion turnover leading to less large adhesions.

In another classic work, depolymerization of microtubules with nocodazole in serum-starved fibroblasts was shown to increase formation of focal adhesions, which then dissolve and turn over following drug washout as microtubules regrow (133). In this model, though FAK null and FAK expressing fibroblasts formed focal adhesions during depolymerization to a similar degree, only cells expressing FAK were able to dissolve focal adhesions following microtubule regrowth. This microtubule depolymerization also corresponds to increased traction forces, which occurred in absence of FAK or myosin II activation, but was blocked by simultaneous inhibition of both (134). Here, we likewise saw larger traction forces in Taxol-resistant cells with more dynamic microtubules (Fig. 5.7). However, consistent with previous reports (147) we found no difference in adhesion strength upon stabilizing (Fig. 5.8A) or depolymerizing microtubules (Fig. 5.8B) suggesting an alternative microtubule-independent signaling pathway was controlling the phenomena.

Focal adhesion turnover is FAK-dependent (133, 139), so we next inhibited FAK with PF228 to attempt to recover adhesion strength. We found it selectively increased adhesive strength in Taxol-resistant cells (Fig. 5.8C) and likewise recovered differences in attachment kinetics (Fig. 5.8D). Similar trends were found by Michael et. al. using FAK-null fibroblasts expressing tetracycline-regulated FAK where FAK expression increased adhesion kinetic parameters but decreased steady-state strength(148). Finally, we verify that FAK is acting up-stream of changes in microtubule dynamics by tracking microtubule plus-ends before and after FAK inhibition. We found significantly decreased microtubule growth rates in both parent and Taxol-resistant populations (Fig. 5.8D) with statistically equal growth rates in both treated populations ($p = 0.37$). Conversely, others have shown that active FAK acts via Rho signaling to facilitate the formation stable Glu-microtubules from the more dynamic tyrosinated microtubules(127). This suggests that FAK inhibition should increase microtubule dynamics; however, these studies in fixed cells may not be able to fully capture microtubule dynamics. Other researchers have noted similar differences when comparing live-cell microtubule dynamics to results quantified from fixed cells stained for Glu-microtubules(149). One potential explanation is that ovarian cancer cells, which are known to overexpress Rho(150), have sufficient basal Rho signaling to circumvent the need for FAK activity to form stabilized microtubules. As noted by Salaycik and colleagues, this may also be because stabilized Glu-microtubules only represent a relatively small fraction of microtubules within the cell, primarily localized to the perinuclear region and not the lamella, or that these signals are required for the generation, but not maintenance of, Glu-microtubules(149). The

increased formation of stable Glu-microtubules also does not preclude the remaining majority of microtubules from exhibiting increases in dynamics.

The hypothesis that FAK intracellular signaling pathway is altering adhesion formation is further supported by the increase in β1 integrin expression in Taxol-resistant populations (Fig. 5.3D). We observed decreased adhesion strength despite higher levels of integrin expression (Fig. 5.5A). Though this result is somewhat counterintuitive, focal adhesion strengthening is largely dependent on both integrin clustering and focal adhesion formation, but can occur without additional binding of integrins to the extracellular matrix (151). Modeling of focal adhesion bond strength indicates that focal adhesion assembly alone can double adhesion strength in absence of integrin binding or clustering (152), in good agreement with our observations. Additionally, the collagen I receptor integrin α2β1 is known to activate FAK, so increased β1 expression may lead to higher FAK activity promoting focal adhesion dissolution (153). There may be additional defects in focal adhesion formation/maturation due to vinculin down-regulation in Taxol-resistant cells (Fig. 5.5E). Loss of vinculin has been shown to increase paxillin-FAK interactions leading to higher phosphorylation of both(137), causing increased focal adhesion disassembly rates (154).

This finding adds to a body of work suggesting that FAK inhibition may be an effective treatment for advanced ovarian cancer (155–157). Previous work has demonstrated that decreasing FAK activity through either FAK silencing (155) or inhibition (156) increases ovarian cancer sensitivity to taxanes. This suggests a causal

role for focal adhesion dynamics in Taxol resistance. In addition to altering microtubule dynamics as shown here, FAK has also been shown to act through additional pathways such as YB1 (156). Furthermore, FAK is significantly up-regulated in ovarian cancer ($p = 1.71e-5$), more than any other tumor site (158) and FAK overexpression has been linked to poor prognosis with an over two-fold decrease in median survival (157). Completed phase I trials of FAK inhibitors in multiple solid tumors show promise (159), and phase I/Ib trials of FAK inhibitors with Taxol are currently underway in patients with advanced ovarian cancer (NCT01778803).

In addition to changes in chemoresistance, these changes in adhesion dynamics may also contribute to cancer metastasis, which is ultimately responsible for 90% of cancer deaths (119). In order to metastasize, cells must first escape the primary tumor. Decreases in focal adhesion strength could increase the frequency of this event, making it easier for cells to begin spreading to distant sites. Moreover, during this process focal adhesion turnover is critical for effective migration; if focal adhesions grow too large the excessive adhesion prevents cell translocation (160). In ovarian cancer, altering these processes by blocking FAK inhibits tumor cell migration and invasion (157). Once reaching the secondary site, the faster attachment kinetics from increased integrin expression could increase the rate at which cells engraft. The interaction of mesothelial VCAM-1 with its ligand $\alpha4\beta1$ integrin is critical for mesothelial cell clearance and ovarian cancer metastasis (64). This process additionally requires cell-generated traction forces found to be up-regulated in Taxol-resistant cells (Fig. 5.7)(75). These findings indicate blocking integrin signaling may also be a successful adjuvant therapeutic in ovarian cancer. Early

clinical trials of anti-integrin therapeutics have already shown success in glioblastoma with minimal toxicity (123), and promise with ovarian cancer as well (161). Several studies also suggest increased integrin expression can lead to general chemoresistance (162) and is a marker of poor patient prognosis (163). The integrin up-regulation may also act synergistically with FAK, as integrin-dependent FAK activation from the ascites can also protect ovarian cancer cells from death by Akt phosphorylation (164).

In conclusion, this study demonstrates previously unknown changes in adhesion properties of cells resistant to chemotherapeutics. These alterations correlated with an increase in microtubule dynamics, but were unaffected by chemical perturbation of microtubule dynamics. FAK inhibition not only mitigated adhesive differences between parent and Taxol-resistant cells, but also normalized microtubule dynamics. Thus, FAK could potentially be therapeutically targeted to not only increase chemosensitivity, but also block metastasis to improve the extremely poor prognosis of chemorefractory ovarian cancer.

5.5 Materials and Methods

5.5.1 Cell Culture and Isolation of Taxol-Resistant Cells

Human ovarian carcinoma SKOV-3 cells were acquired from ATCC and OVCAR-3 cells were the generous gift of Dr. John McDonald. Both cell lines were cultured in RPMI 1640 (Corning) containing 10% FBS (Atlanta Biologicals) and 1% penicillin streptomycin (Corning). To isolate Taxol resistant cell lines, cells were plated at 20% of confluence and treated with 10 nM Taxol (Enzo) for 48 hours before returning to growth media. After reaching 40% of confluence, cells were again treated with 10 nM Taxol for 48 hours before returning to growth media. This process was repeated until the Taxol could no longer maintain cell growth (approximately 4 months for OVCAR3 and 6 months for SKOV3), at which time cells were fed with standard growth media with a maintenance concentration of 5 nM Taxol added at least once per week. Four independent viability assays were performed over the course of the study with no significant change in IC_{50}.

5.5.2 Viability Assay

Cells were plated at 20% of confluence before treating with varying concentrations of Taxol, 25 μM carboplatin (approximately the IC_{50} for both cell lines)(165), or a DMSO solvent control (<0.1% v/v). After 72 hours, cells were incubated in 1mg/mL MTT reagent for four hours in standard growth conditions. The supernatant was then removed and replaced with isopropanol acidified with 4mM HCl to solubilize insoluble purple formazan product. The absorbance of this product was then measured in DTX-800 Multimode Detector microwell plate reader (Beckman Coulter) at 620 nm absorbance

with 595 nm reference value. Since low-dose Taxol showed a significant increase in Taxol-resistant cell viability we chose to interpolate the IC_{50} in the linear region of the plot instead of a standard sigmoidal fit which may not accurately model the data.

5.5.3 Attachment Kinetics

All plates were coated with 10 µg/mL Collagen I (Corning) and blocked with 1% heat-denatured BSA (Rockland) unless otherwise noted. Cells were first labeled with 2 µM Calcein AM (AnaSpec), a transmembrane green fluorescent marker, in HBSS with divalents (Corning) for 20 minutes at 37°C. Next, cells were passed per standard procedure, resuspended in media, and incubated for 30 minutes at 37°C. Cells were then pelleted and resupsended in adhesion buffer (140 mM NaCl, 2.5 mM KCl, 1.8 mM $CaCl_2$, 1.0 mM $MgCl_2$, 20 mM HEPES, 20 mM dextrose, pH 7.4) before plating at 20% of confluence. At each time point, non-adherent cells were removed to a new plate. At the end of the experiment, the fluorescence of the plates containing both the adherent and non-adherent fractions was read at 485nm excitation, 535nm emission in a DTX-800 Multimode Detector microwell plate reader. Adherent fraction was then defined as the reading of the adherent cells over the sum of the adherent cells and non-adherent cells. Attachment was modeled by the differential equation $dC_{Adh}/dt = kC_{Non-adh}$ where C is the concentration of cells and k is the adhesion rate. This equation can be reduced to $dA/dt = k(1 - A)$ where A is adherent fraction calculated as $A = C_{Adh}/(C_{Adh} + C_{Non-adh})$ and solved using boundaries of A=0 and A=1 at t=0 and as t→∞, respectively, to yield $A(t) = 1 - e^{-kt}$. The equation was linearized, yielding R^2 values for individual experiments ranging from 0.92 to 0.99.

5.5.4 Adhesion Strength

Adhesion strength was quantified in a centrifugal force-based adhesion assay(68). Cells were allowed to adhere overnight to a collagen-coated (unless otherwise noted) 96 well plate and then labeled with Calcein AM. The media was replaced with adhesion buffer before taking an initial fluorescence reading, and then plates were inverted and centrifuged at 29 rcf for 5 minutes. After washing with adhesion buffer, a final reading was taken. Detached fraction was determined as one minus final fluorescence divided by initial fluorescence. In some experiments, cells were pre-incubated with Taxol, Nocodazole (Sigma), or PF-573,228 (PF228, Sigma) 4 hours before performing the experiment.

5.5.5 Rhodamine Efflux

Cells in a 96 well plate were loaded with 0.5 μg/mL Rhodamine 123 for 60 minutes and then washed extensively with adhesion buffer. At desired time points, supernatant was removed for fluorescence quantification at 485 nm excitation, 535 nm emission. To account for variations in loading, rhodamine efflux was determined as [effluxed rhodamine / (effluxed rhodamine + rhodamine in cells)]. Rate constants were fit as described in attachment kinetics. For 24 hour efflux, a similar procedure was performed except cells were incubated in growth media.

5.5.6 Flow Cytometry

To determine levels of surface integrin expression, cells were analyzed with a BD LSR-II flow cytometer. Briefly, cells were detached with 5 mM EDTA, centrifuged, and separated into 100μl aliquots then labeled with PE-conjugated anti-human CD29 (integrin

β1, Clone TS-2/16, BioLegend) per manufacturer's instructions. Mean fluorescence intensity was determined after subtraction of a respective negative control.

5.5.7 Focal Adhesion Staining and Image Analysis

For immunostaining all cells were plated on collagen I coated coverslips. For focal adhesion staining, cells were fixed in 4% formaldehyde, permeabilized with 0.5% Triton X-100, and blocked with 5% horse serum before staining with either 1:200 anti-paxillin (Clone Y113, GeneTex), 1:500 anti-vinculin (Invitrogen), or 1:200 anti-FAKp397 (Genetex) diluted in PBS with 1% BSA. Cells were then washed, incubated with 1:100 rhodamine phalloidin (Invitrogen) and anti-rabbit Alexa Fluor 488 (Invitrogen), counterstained with DAPI (AnaSpec), and sealed with Vectashield (Vector Labs). All images were captured at 40x magnification on an inverted Nikon Microscope with a CoolSNAP camera (Photometrics). For each experiment, all images were captured in one session and normalized to the average for that session to account for any differences in light brightness. To quantify focal adhesions, paxillin images were first convolved with a low pass Gaussian filter before applying a morphological top hat filter to correct for differences in basal paxillin expression. Pixels within the cell area (determined based on F-actin fluorescence) that exceeded the cell background by 2 standard deviations were considered positive. After thresholding, pixel noise of less than 10 pixels (~0.25 μm^2) was discarded. The remaining segmented focal adhesions were used for analysis, with pixel intensity values taken from the original, unfiltered image after background subtraction (background defined as the average intensity value of the non-cell area).

Focal adhesion density was calculated as the integrated focal adhesion intensity normalized to cell area.

5.5.8 Western Blot Analysis

Cells were lysed in radioimmunoprecipation buffer containing a protease inhibitor cocktail and separated on either 10% (paxillin/tubulin) or 7.5% (vinculin/FAKp397) polyacrylamide gel before transferring to a PVDF membrane. Membranes were blocked in 5% milk, and incubated overnight at 4°C in primary antibodies against tubulin (1:3000, Rockland), paxillin (1:500, BioLegend), vinculin (1:1000, Invitrogen), or FAKp397 (1:1000, Genetex). Bands were visualized following incubation with 1:1000 HRP-conjugated anti-rabbit IgG (Rockland) using Novex ECL chemiluminescent substrate (Invitrogen). Since typical loading controls such as cytoskeletal elements (tubulin/actin) or metabolic enzymes (GAPDH) are often differentially expressed in cancer, we utilized total protein as a loading control by staining the membranes with Coomassie G250 (BioRad). Quantification of total protein has been not only been shown to be more consistent across different cells than typical loading control proteins, but also offer improved detection linearity (166, 167). All analysis was performed using built-in blot analysis tools in ImageJ (NIH) as described in the user manual (http://rsbweb.nih.gov/ij/docs/guide/, Section 30.13).

5.5.9 Tubulin Polymerization Assay

A microtubule pelleting assay was used to quantify fraction of polymerized tubulin as previously described(168). Cells that had been in absence of Taxol for 5-7 days were grown to 80% confluence in a 24-well plate. Cells were lysed with 100μL hypotonic lysis

buffer (20 mM Tris-HC1, pH 6.8, 0.5% Nonidet P-40, 1 mM MgC12, 2 mM EGTA) for 5 minutes. Lysates were transferred to a 1.5 mL microcentrifuge tube, wells were washed 1x with 100μL hypotonic lysis buffer, and the entire 200 μL volume was vortexed before pelleting the insoluble fraction by room temperature centrifugation at 12,000 rcf for 10 minutes. Meanwhile, any remaining cytoskeletal elements in the wells were dissolved in the above buffer with addition of 0.5% SDS. Finally, supernatants were transferred to a new tube and pellets re-suspended in the SDS-containing buffer with the remaining insoluble tubulins. Equal volumes were loaded for immunoblotting as described above.

5.5.10 Microtubule Recovery Assay

To visualize microtubule regrowth, microtubules were first depolymerized by treatment with 20 μM nocodazole for 4 hours and then allowed to regrow following washout for specified periods of time. To ensure accurate washout times all coverslips for each cell line were initially contained within the same 10cm dish which was then washed four times with fresh media before returning to media that had been pre-equilibrated in the cell incubator to 5% CO_2 for regrowth in normal culture conditions. At desired time points, coverslips were removed for processing. Cells were stained for F-actin and microtubules as previously described (169). In brief, cells were Triton-extracted before fixing in glutaraldehyde, which was then neutralized with sodium borohydride before blocking in horse serum and incubating with rhodamine phalloidin and FITC-conjugated anti-α-tubulin (Sigma, clone DM1a). The α-tubulin isoform has been shown to be unchanged with Taxol-resistance (116).

5.5.11 EB3 Microtubule Tracking

To visualize live-cell microtubule dynamics, cells were transfected with mApple-EB3, a gift from Michael Davidson (Addgene plasmid #54892), using the TransIT-LT1 transfection reagent (Mirus Bio) per manufacturer's instructions. Cells were imaged with a Nikon Eclipse Ti inverted epifluorescent microscope, maintained at 37° C and 5% carbon dioxide throughout the experiment using an In Vivo Scientific environmental cell chamber and Bioscience Tools CO_2 controller. A Photometrics QuantEM CCD camera (Princeton Instruments) was used to minimize exposure time while imaging with a Nikon CFI Apochromat TIRF 100X oil-immersion lens. Videos were captured at 1 Hz for 2 minutes and quantified using the open source u-track software as described (132, 170).

5.5.12 Traction Force Cytometry

Cell-exerted forces were quantified by traction force cytometry as previously described (84, 109) by culturing cells on an elastic 10 kPa collagen-coated polyacrylamide substrate embedded with 200 nm fluorescent nanoparticles as fiduciary tracers. After capturing an initial image of the cells and particles, cells were removed by trypsinization and a final particle image captured. The embedded beads were used to determine gel displacement, which could then be used to calculate forces(70).

5.5.13 Statistics

The data are reported as mean ± standard error of the mean (SEM) from three independent experiments unless otherwise noted. Statistical analysis was carried out using a student's t-test or analysis of variance (ANOVA) followed by post-hoc analysis with Student–Newman–Keuls test, considering $p < 0.05$ to be significant

(***$p<0.001$,**$p<0.01$,*$p<0.05$). Pearson correlation coefficients (ρ), ranging from -1 for perfectly inversely correlated to +1 for perfectly positively correlated, were determined in MATLAB.

CHAPTER 6
EPITHELIAL-MESENCHYMAL TRANSITION PRODUCES CONCERTED BIOPHYSICAL CHANGES FROM ALTERED CYTOSKELETAL GENE EXPRESSION[4]

6.1 Summary

A growing body of evidence suggests that the developmental process of epithelial-to-mesenchymal transition (EMT) is coopted by cancer cells in order to metastasize to distant sites. This transition is associated with morphological elongation and loss of cell-cell adhesions, though little is known about how it alters cell biophysical properties critical for migration. Here, we use multiple-particle tracking microrheology and traction force cytometry to probe how genetic induction of EMT in epithelial MCF7 breast cancer cells changes their intracellular stiffness and extracellular force exertion, respectively, relative to an empty-vector control. This analysis demonstrated that EMT alone was sufficient to produce dramatic cytoskeletal softening coupled with increases in cell-exerted traction forces. Microarray analysis revealed that these changes corresponded with down-regulation of genes associated with actin crosslinking and up-regulation of genes associated with actomyosin contraction. Finally, we show that this loss of structural integrity to expedite migration could inhibit mesenchymal cell proliferation in a secondary tumor as it accumulates solid stress. This work demonstrates that not only does EMT enable escape from the primary tumor through loss of cell adhesions, but it also

[4]McGrail DJ, Mezencev R, Kieu QMN, McDonald JF, Dawson MR. (2014) SNAIL-induced epithelial-to-mesenchymal transition produces concerted biophysical changes from altered cytoskeletal gene expression. *FASEB J.* 29: 1280–9.

induces a concerted series of biophysical changes enabling enhanced migration of cancer cells after detachment from the primary tumor.

6.2 Introduction

The problem of cancer metastasis is undoubtedly one of the biggest hurdles facing cancer clinicians, as this deadly process is currently responsible for over 90% of cancer-related deaths. A large body of evidence suggests that epithelial-to-mesenchymal transition (EMT), whereby less motile regularly shaped polygonal epithelial cells transition into elongated invasive mesenchymal cells, is critical for cancer cells to leave the primary tumor to spread to distant sites (171). This increased invasiveness is largely attributed to loss of E-cadherin responsible for cell-cell adhesion and increasing expression of matrix-binding integrins (23). Furthermore, increased expression of matrix-degrading matrix metalloproteinases allows for degradation of the basement membrane and dissemination to other tissues (24).

In addition to these molecular changes, the emerging field of physical oncology has highlighted that cells modulate their mechanical properties in order to disseminate effectively (119). Moreover, during the morphological rearrangement the epithelial cells lose their apical-basal polarity causing dissolution of cortical actin structure as the cells gain the more elongated mesenchymal morphology with front-rear polarity (172). Despite extensive study into EMT over the past three decades, how it affects these critical biophysical properties remains largely unknown. Environmental factors used to induce EMT, such as soluble factors, matrix stiffness, or adhesive ligands (22), alter other

biophysical and biochemical properties confounding the analysis of the effects of EMT alone. These pathways use a variety of intermediate signaling molecules, but in all studied cases of EMT they converge on the activation of SNAIL genes (173). SNAIL is a transcriptional repressor primarily thought to induce EMT from direct repression of E-cadherin leading to nuclear β-catenin accumulation and activation of WNT signaling (171), but E-cadherin knockdown fails to recapitulate SNAIL-induced EMT suggesting that SNAIL plays a broader role in EMT (174). Thus, in order to directly examine EMT in isolation without confounding environmental cues we utilized a robust genetically-engineered model of EMT in epithelial MCF7 breast cancer cells. To do so, we chose a SNAIL variant modified to be stable and localized within the cell nucleus, which was recently shown to be a superior model of EMT compared to overexpression of wild-type SNAIL (175).

Here, we demonstrate that EMT directly produces biophysical changes resulting in a pro-metastatic phenotype and further elucidate the underlying alterations in gene expression by microarray transcriptomic analysis. SNAIL-transformed cells were significantly more compliant than an empty-vector control, both softening their cytoplasm by an order of magnitude and relaxing their nucleus approximately 5-fold to allow for navigation of the extracellular environment. These mechanical changes coincided with structural changes including decreased polymerized actin and abnormal nuclear morphology, correlating with decreased expression of actin crosslinkers such as *FLNA* (Filamin A) and structural nuclear proteins such as *LMNA* (Lamin A). In addition to these changes in intracellular compliance and structure, EMT also increased

extracellular force exertion and contractile gene expression to further expedite migration. We show these changes allow for increased motility regardless of extracellular mechanics, possibly helping cells adapt to their new environment as they disseminate. However, more migratory mechanically compliant SNAIL cells lacked the structural stability to form large spheroids analogous to secondary tumors. Taken together, this work not only demonstrates that biophysical changes associated with cancer progression are produced by EMT, but integrates this mechanical analysis with gene expression profiling for a more complete portrait of this key process in cancer metastasis.

6.3 Results

6.3.1 SNAIL transformation induces a mesenchymal phenotype and increased malignant character.

After transformation with SNAIL-6SA, MCF7 breast cancer cells exhibited a more mesenchymal phenotype than their empty vector transformed controls. This was confirmed both by cell morphology, where SNAIL cells showed a two-fold increase in aspect ratio (Fig. 6.1A-B), as well as gene expression which revealed classical changes associated with EMT such as down regulation in E-cadherin (*CDH1*) as well as up-regulation of N-cadherin (*CDH2*) and vimentin (*VIM*) (Fig. 6.1C). To understand the functional consequences of this transformation, we next evaluated the migratory and proliferative capacity of the transformed cell lines. We tracked the migration of over 500 cells per condition (Fig. 6.1D) and found mesenchymal SNAIL-transformed cells showed a large ($p<1e-5$) increase in motility relative to their control counterparts with an over two-fold increase in cell speed (Fig. 6.1E). Moreover, SNAIL cells utilized a different

migratory phenotype characterized by "bursty" migration as opposed to persistent migration over time. We quantified this difference by the coefficient of variation (176), which increases as the velocity of a cell becomes less consistent, to find a significant

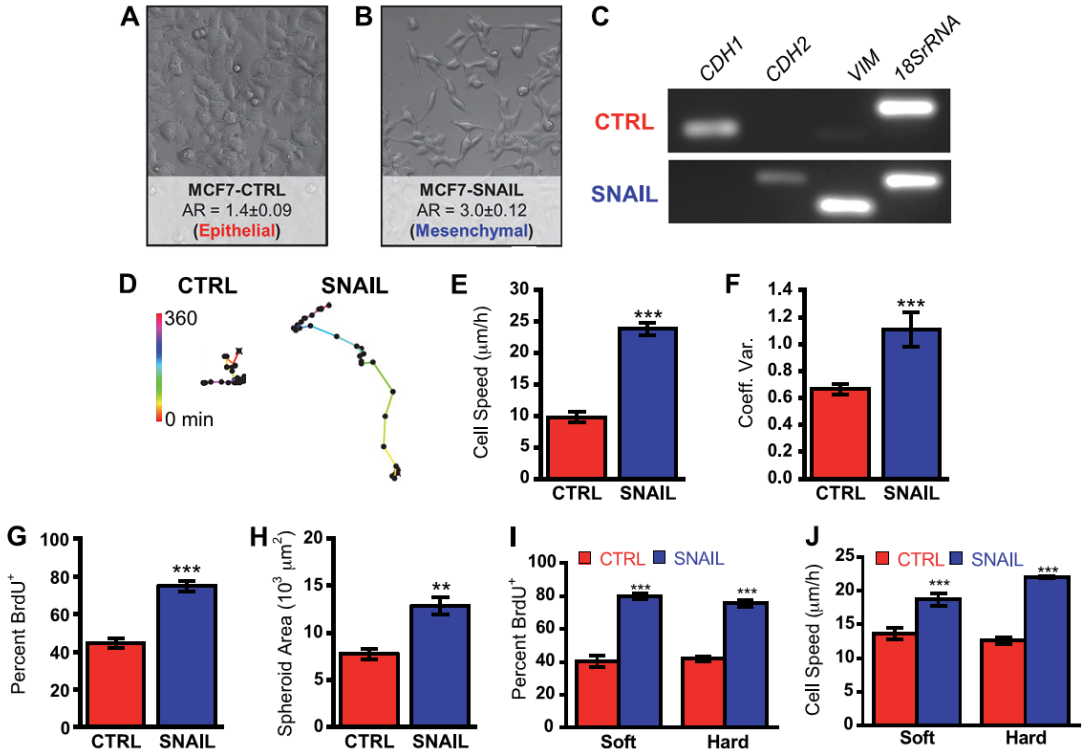

Figure 6.1 MCF-7 cells transformed with SNAIL-6SA show increased mesenchymal phenotype and malignant characteristics. Empty-vector transformed MCF7-CTRL (A) display a cobblestone morphology whereas MCF7-SNAIL (B) are more elongated, with a two-fold increase in aspect ratio (AR). (C) SNAIL transformation induces changes in CDH1 (E-cadherin), CDH2 (N-cadherin), and VIM (Vimentin) gene expression associated with EMT. (D) Exemplary traces of control and SNAIL cells color-coded by time, each dot representing a 10 minute interval. (E) Average instantaneous velocity of SNAIL cells is significantly greater than control cells. (F) Coefficient of variation, defined as the standard deviation of a cell's instantaneous velocity over the average instantaneous velocity, is significantly increased in SNAIL cells indicating more bursty migration. SNAIL increases proliferation quantified both in a 2D system by BrdU incorporation (G) and in a 3D anchorage-independent spheroid assay (H). Motility is increased and altered by SNAIL transformation. When cultured on either soft (2.83 kPa) or hard (34.88 kPa) substrates SNAIL cells remain more proliferative (I) and more motile (J) regardless of matrix stiffness.

increase following SNAIL transformation (Fig. 6.1F). Finally, we evaluated proliferation in both 2D and 3D. When grown on a 2D surface, the proliferation was significantly increased in SNAIL-transformed cells (Fig. 6.1G). Proliferation was also increased in 3D, as determined with an anchorage-independent spheroid formation assay in agarose (Fig. 6.1H). This increase in proliferation and migration indicative of a more aggressive phenotype are conserved across multiple substrate rigidities by repeating the proliferation (Fig. 6.1I) and motility (Fig. 6.1J) experiments on soft (2.83 kPa) and hard (34.88 kPa) substrates.

6.3.2 Increased traction forces during SNAIL-induced EMT

Due to the major role of actomyosin contraction in cell migration, we utilized traction force cytometry to quantify alterations in cell-exerted traction forces after EMT. Traction force maps of control (Fig. 6.2A) and SNAIL (Fig. 6.2B) cells show altered force arrangement. Control cells have forces distributed throughout the cell body whereas SNAIL forces are more localized to the tips of the cell. In addition to this altered intracellular distribution, SNAIL cells also exerted significantly ($p<0.01$) higher forces (Fig. 6.2C). Due to the increased "bursting" migration in the SNAIL cells, we hypothesized that this would translate to capturing some cells "post-burst" and others "pre-burst" resulting in a larger variance within the population compared to the control cells that moved more consistently. Supporting this idea, we found that the coefficient of variance for traction stress within each individual experiment was increased almost two-fold in the SNAIL cells (Fig. 6.2D). Microarray analysis of gene expression data revealed that this force increase coincided with up-regulation of genes that promote actomyosin

contraction such as *MYLK* (myosin light chain kinase) and *MYH10* (myosin IIb) as well as down-regulation of genes that reduce contractility such as *PPP1R12B* (myosin phosphatase) (Fig. 6.2E).

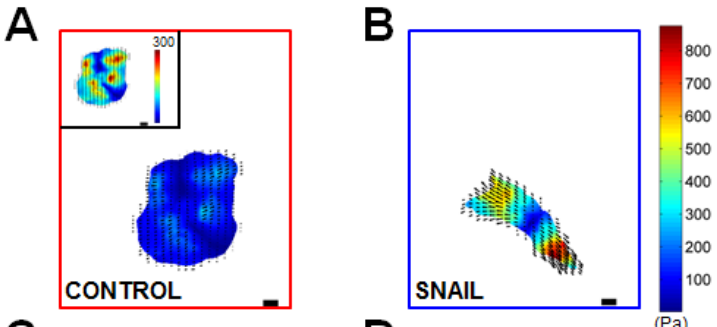

E

Gene	FC	Gene	FC
Up-Regulated		Down-Regulated	
DAPK1	10.81	*CDC42BPB*	-1.88
MYH10	2.87	*ARHGAP35*	-2.22
PRKCA	2.26	*PPP1R12B*	-2.68
MYLK	2.20	*ARHGAP1*	-3.92
ARHGEF3	1.74	*CNN2*	-4.51
		MYH14	-8.02

Figure 6.2 SNAIL-induced EMT increases cell-exerted traction forces. Traction heat maps in units of Pascals ranging from 0 (dark blue) to 850 (dark red) overlaid with matrix displacements (black arrows). Scale bars are 10 μm. (A) Control cells forces are located predominately in the cell interior (inset heat map is rescaled to a max value of 300 Pa for visualization). (B) SNAIL cells exert forces closer to the cell periphery. (C) Peak traction stresses in SNAIL cells were 3-fold higher than those exerted by control cells. (D) Coefficient of variation, defined here as the standard deviation of the cells within each experiment over the average of all the cells within the experiment, is increased as seen with motility results in Figure 1. (E) Microarray analysis shows differential regulation of contractile markers between SNAIL and control cells.

6.3.3 EMT softens the cytoplasm and alters actin structure

In order to investigate how EMT altered intracellular mechanics, we utilized multiple particle tracking microrheology (MPT) to determine rheological information from the thermal motion of ballistically injected fluorescent nanoparticles (177). Larger mean squared displacements (MSDs) of particles in SNAIL cells indicate less resistance to particle motion within their cytoplasm. At all evaluated time scales, SNAIL cells displayed a higher MSD (Fig. 6.3A). This result translated to a 5-fold higher effective diffusion coefficient (Fig. 6.3B) and an order of magnitude increase in cytoplasmic compliance (Fig. 6.3C). Calculation of viscoelastic parameters further revealed that control cells have an appreciable elastic moduli of 29±5 dyn/cm^2, but this value is almost negligible for SNAIL cells at 0.6±0.4 dyn/cm^2 (Fig. 3D) with similar trends in viscosity (Fig. 6.3E). Moreover, though control cells maintained some elastic character over all frequencies, SNAIL cells became entirely viscous (phase angle of 90°) at frequencies higher than 1 Hz (Fig. 6.3F).

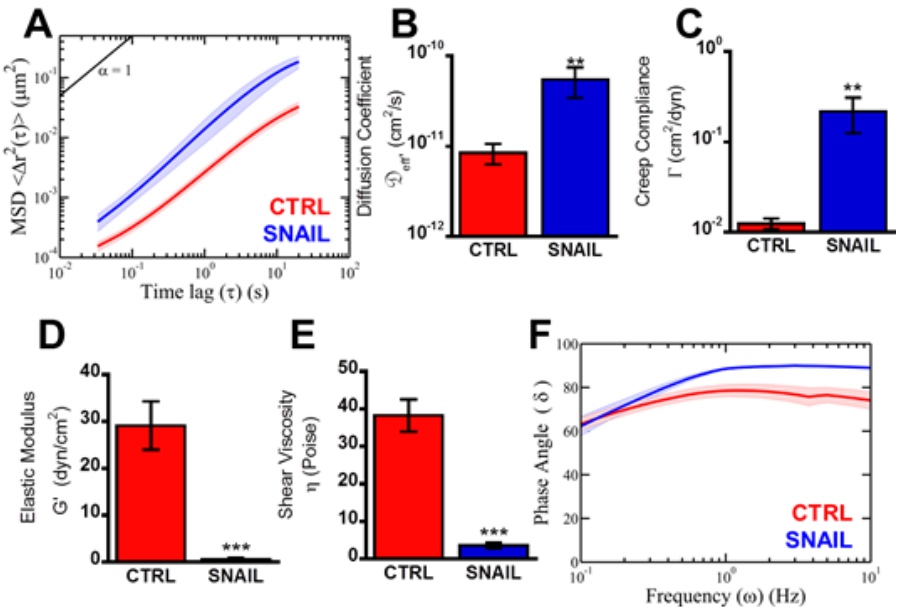

Figure 6.3 Analysis of intracellular microrheology reveals greatly softened cytoplasmic space by SNAIL transformation through loss of polymerized actin. (A) Mean-squared displacements (MSDs) of 200 nm particles injected into the cytoplasmic space are increased by nearly half a decade across all time lags. (B) Intracellular diffusion coefficient at τ = 1 s is decreased over five-fold in SNAIL cells. (C) Creep compliance of cytoplasm is also decreased by an order of magnitude at τ = 1 s. (D) Elastic moduli at a frequency of 1 Hz is significantly decreased in SNAIL cells. (E) Shear viscosity shows similar decrease in SNAIL cells. (F) Evaluation of the phase angle, δ, which quantifies the relative ratio of viscous to elastic character shows that at frequencies above 0.3 Hz SNAIL cells show significantly lower elastic character.

We hypothesized that these changes in cytoplasmic mechanics were largely due to decreases in actin polymerization. To test this hypothesis, we stained cells for F-actin, which showed that control cells had organized actin filaments and that tension from these cortical actin stress fibers helps create a more uniform, flat cell shape (Fig. 6.4A). Overexpression of SNAIL dissolved these stress fibers (Fig. 6.4B) and produced more rounded, three dimensional cells (Fig. 6.4B). SNAIL cells also displayed enhanced lamellipodial ruffling at either pole (blue arrows), as well as additional filopodial structures extending from the cell body (red arrow). We additionally characterized intermediate filaments cytokeratin and vimentin which are known to be down- and up-

regulated during the EMT (22), respectively, and are known to play a role in cell mechanical properties (178–180). Though control cells display robust keratin networks, these are completely lost following EMT in SNAIL cells (Fig. 6.4D). Conversely, ectopic SNAIL expression increased the expression of vimentin (Fig. 6.4E). To quantify these changes we took the integrated fluorescence density of each filament, revealing that SNAIL cells have a 3-fold decrease, 10-fold decrease and a 4-fold increase in F-actin, cytokeratin, and vimentin, respectively (all $p<0.001$, Fig. 6.4F). This was further confirmed by gene expression data showing the up-regulation of vimentin as well as down-regulation of several keratin isoforms (Fig. 6.4G).

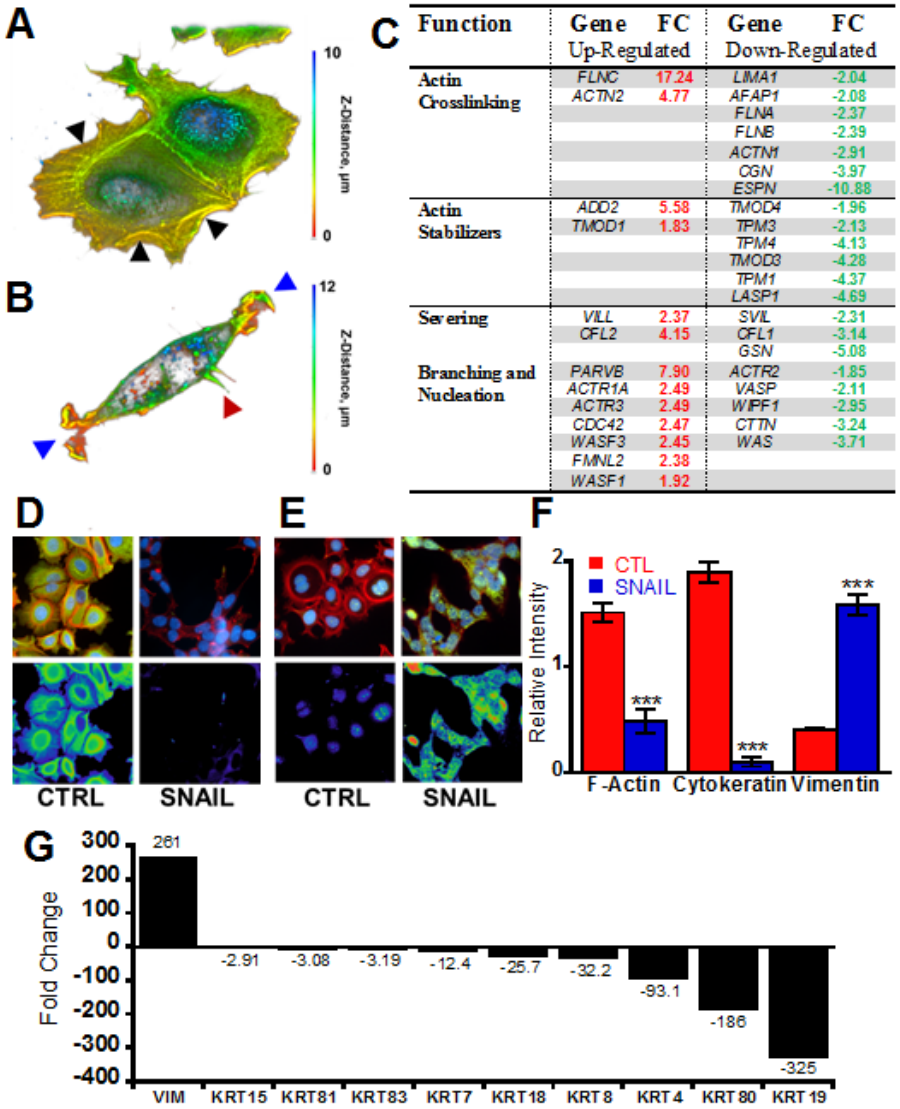

Figure 6.4 Cytoskeletal architecture is altered by EMT. To visualize corresponding changes in cytoskeletal structure, cells were stained for F-actin and visualized via confocal microscopy. Three dimensional confocal reconstruction color-coded by Z-distance for (A) control cells and (B) SNAIL cells shows not only cortical actin structure present in control cells (black arrows) but also increased ruffling (blue arrows) and actin protrusions (red arrow) in SNAIL cells. (C) Microarray analysis of gene expression data reveals significant dysregulation of genes associated with actin cytoskeletal structure. To visualize intermediate filaments cells were stained for cytokeratins (D) and vimentin (E) both shown in green, and then counterstained for F-actin (red) and nuclei (blue). (F) Quantification of fluorescence intensities show that SNAIL cells have decreased levels of F-actin and cytokeratin but increased level of vimentin (all values reported normalized to the average of both cell types). (G) Gene expression analysis shows up-regulation of vimentin and down-regulation of several cytokeratins consistent with protein expression findings. All scale bars are 10 µm in length.

To determine the molecular mechanism for this loss of mechanical structure, we utilized several approaches to analyze microarray gene expression data. The GSEA analysis, which does not depend on an arbitrary selection of differentially expressed genes revealed that the "Actin Polymerization and/or Depolymerization" (M2403) and "Rho Protein Signal Transduction" (M7069) gene sets were significantly enriched in the control phenotype (q-values 0.223 and 0.196, respectively). Since Rho GTPase is known to regulate actin cytoskeleton remodeling during cell morphogenesis and motility (181), our data suggest that phenotypic differences between mesenchymal-like SNAIL and epithelial-like control cells likely include Rho-mediated reorganization of actin cytoskeleton. Consistent with this finding, pathway enrichment analysis by MetaCore suite identified alterations in several actin cytoskeleton-related gene signaling networks including "Regulation of Cytoskeletal Rearrangement" ($p=5.06\times10^{-7}$, FDR $q=2.70\times10^{-5}$) and "Cytoskeleton Actin Filaments" ($p=3.55\times10^{-6}$, FDR $q=1.14\times10^{-4}$). Moreover, analysis by David 6.7 functional annotation tool identified KEGG pathway "Regulation of Actin Cytoskeleton" (hsa04810, Fig. 6.5A) as significantly enriched ($p=4.7\times10^{-3}$, FDR q=0.00092) for genes down-regulated in SNAIL cells.

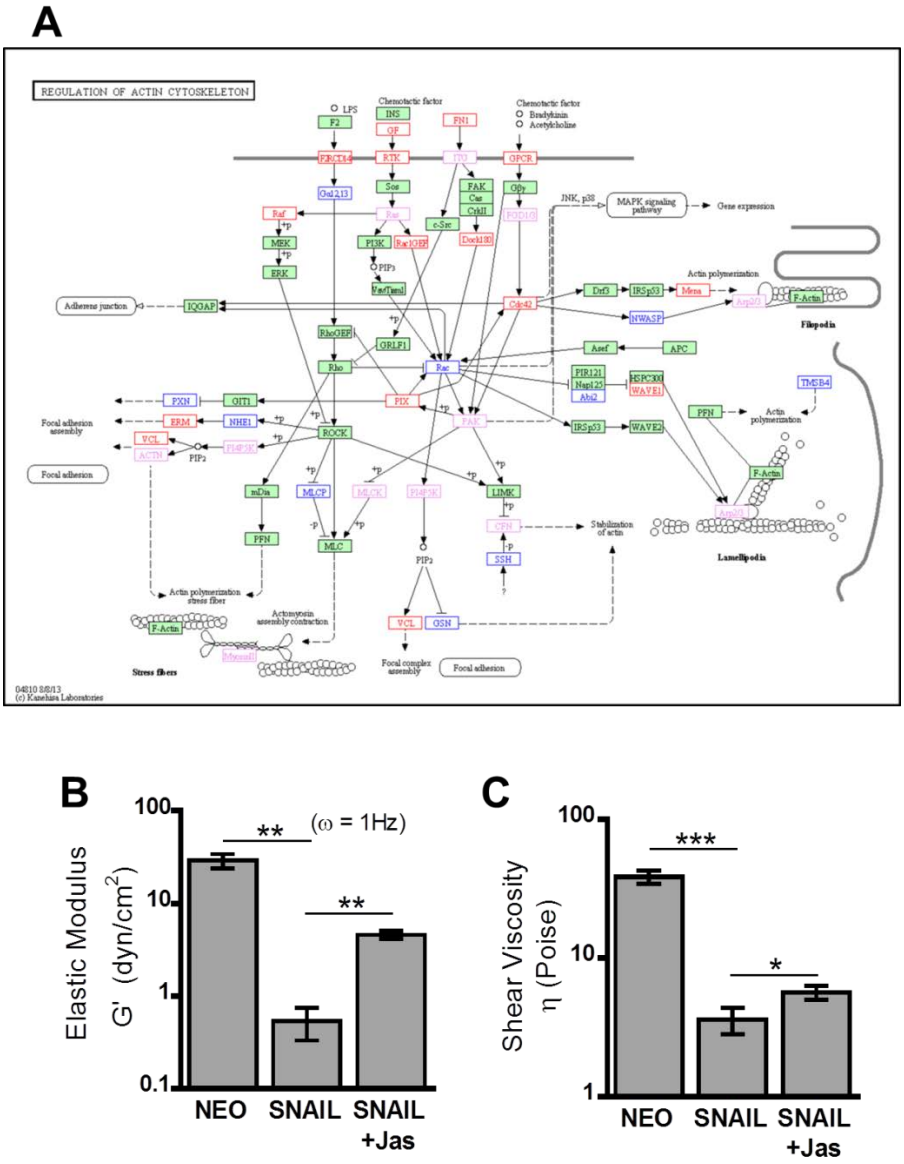

Figure 6.5 Changes in actin cytoskeleton and cell rheology. (A) Regulation of Actin Cytoskeleton – Homo sapiens (KEGG pathway hsa04810) with mapped color-coded genes identified as differentially expressed between SNAIL and control cells. Red: up-regulated in SNAIL cells; blue: down-regulated in SNAIL cells; pink: both up- and down-regulated genes were identified for given KEGG entry; green rectangles: genes not identified as differentially expressed. Changes in cell rheology following treatment with actin-stabilizing Jasplakinolide (Jas). (B) The elastic moduli of SNAIL cells is partially recovered following actin treatment, increasing an order of magnitude from untreated levels. (C) Shear viscosity is also partially recovered in SNAIL cells treated with Jasplakinolide increasing 2-fold.

To verify that these changes were primarily caused directly through SNAIL-induced EMT and not through down-stream modulation of non-EMT genes, we compared microarray results from other related perturbation experiments with MCF7 cells. Since the loss of estrogen receptor-alpha (ERα) is associated both with breast cancer progression and SNAIL expression (182), we analyzed changes in MCF7 cells induced by siRNA-mediated knockdown of the expression of *ESR1* gene that encodes ERα. This analysis revealed minimal changes in the expression of EMT-associated genes and no enrichment of the actin-related processes seen in the SNAIL cells. Furthermore, analysis of vimentin knockdown only revealed one conserved actin-related gene, the cross linker cingulin, indicating it may have some effect on the actin cytoskeleton in isolation.

For brevity, a subset of actin cytoskeleton-related genes is displayed in Figure 6.4C. There was no clear trend in actin severing proteins, but several actin crosslinking genes such as filamins A and B were down-regulated along with a series of actin stabilizing proteins. This implies that the loss of actin structure was largely mediated via decreased expression of actin cross-linking, not an increased rate of disassembly. We further tested this hypothesis by treating cells with membrane permeable jasplakinolide, which acts to polymerize and stabilize actin filaments, and found that this treatment was only able to partially recover cell mechanical properties (Fig. 6.5B-C). This incomplete recovery may be due to the lack of filamins to crosslink the actin fibers in SNAIL cells, or because some of the mechanical stability originates from keratin intermediate filaments which were lost following SNAIL transformation. Though actin severing proteins showed no direct relation to actin cytoskeletal architecture, the large down-regulation of gelsolin is

notable since reduced expression in breast cancer is associated with poor patient prognosis (183, 184). This indicates decreased gelsolin may be a conserved feature of breast cancer progression. Moreover, several genes associated with filopodia formation such as *CDC42*, *ACTR3*, and *PARVB* were up-regulated suggesting these regulate the protrusion formation in SNAIL cells. Interestingly, Snail cells also overexpress the *WASF3* gene encoding WAVE3 member of WASP/WAVE protein family known to regulate actin cytoskeleton remodeling through Arp2/3 and enhance invasive and metastatic potential of breast cancer cells in vitro and in vivo (185).

6.3.4 SNAIL relaxes nuclear stiffness and produces defects in nuclear morphology

Though relaxing cytoskeletal rigidity may help cells navigate through tight pores in the extracellular matrix, the nuclear deformation is often the rate limiting step for effective invasion (186). Thus, we sought to probe if SNAIL-induced EMT would likewise soften nuclear mechanics by performing particle tracking in the nucleus but instead of using injected nanoparticles utilizing Hoechst-labeled chromatin as tracer particles (187). Consistent with previous studies, we found at short time-scales the nuclei of both cells behaved as elastic solids, corresponding to a MSD slope close to zero (Fig. 6.6A). However, at later time scales nuclei began to transition to more viscous behavior indicated by an increasing MSD slope approaching one for a perfectly viscous material. The time for this transition, or relaxation time, was 5-fold faster in SNAIL cells (Fig. 6.6B). This relaxation produced a significantly softer nucleus after SNAIL transformation, quantified by an effective diffusion coefficient nearly an order of magnitude higher than control cells (Fig. 6.6C).

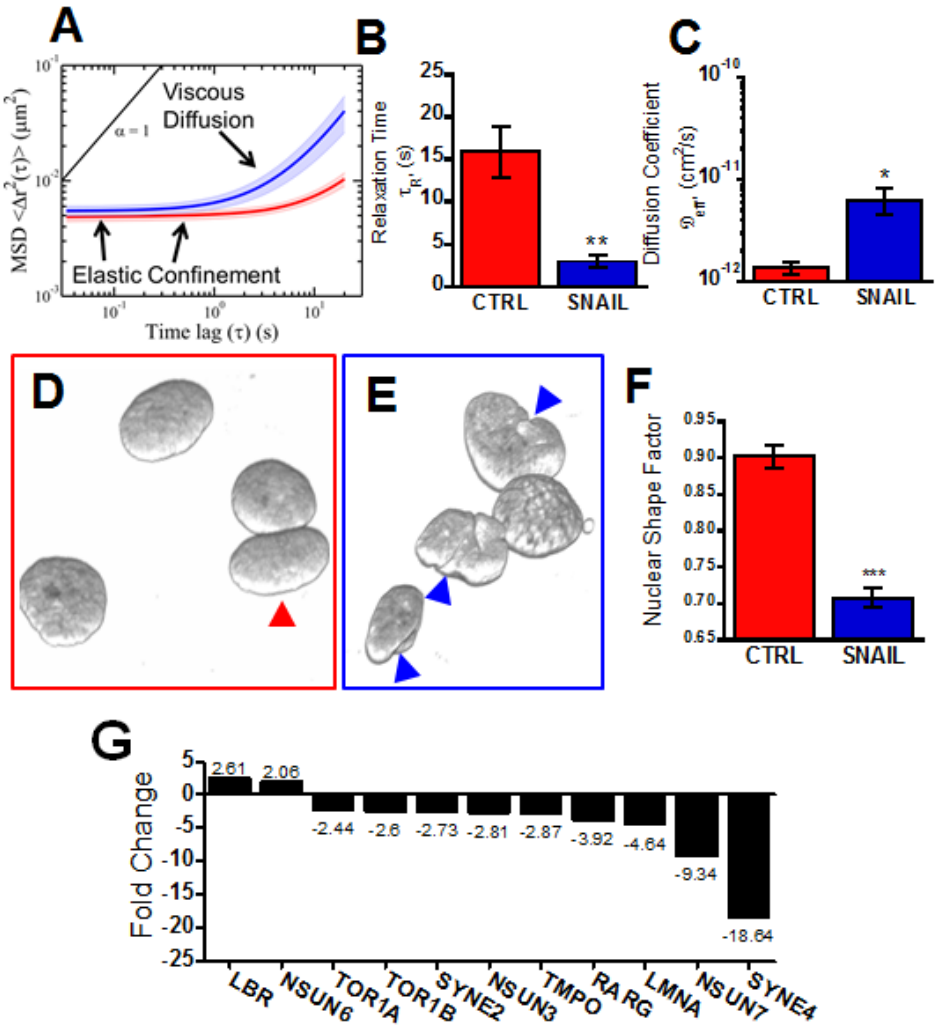

Figure 6.6 Nuclear structure is compromised by SNAIL-induced EMT. (A) Mean-squared displacements (MSDs) of Hoechst-labeled chromatin show that while at low scales nuclei behave primarily as an elastic solid regardless of cell line, at later time MSDs begin to increase indicative of more viscous diffusion. (B) Quantification of the time until this relaxation from elastic to viscous character shows that it happens over 3-fold faster in SNAIL cells. (C) The nuclei of SNAIL cells show a nearly order of magnitude increase in effective diffusion coefficient at 10 seconds. Loss of nuclear integrity was verified by examining three dimensional reconstructions of confocal micrographs where control cells (D) show some elongated nuclei (red arrow), but SNAIL nuclei (E) show several abnormal structural deformations (blue arrows). Scale bars are 10 μm in length. (F) This structural abnormality was quantified by nuclear shape factor, or $4 \cdot \pi \cdot \text{Area}/\text{Perimeter}^2$ ranging from 0 for a line to 1 for a perfect circle showing a significant decrease in SNAIL cell nuclei. (G) Gene expression analysis shows down-regulation of several genes associated with nuclear structure in SNAIL cells.

Based on this loss of mechanical stability, we sought to determine if this produced alterations in bulk nuclear structure. Though there were some visually elongated nuclei in both the control cells (Fig. 6.6D, red arrow) as well SNAIL cells, the latter additionally displayed frequent aberrations in nuclear morphology including elongation, but also excessive creasing and folding within the membrane (Fig. 6.6E, blue arrows). Morphological quantification based on nuclear shape factor (188), defined as $4 \cdot \pi \cdot \text{Area}/\text{Perimeter}^2$ ranging from 0 for a line to 1 for a perfect circle, demonstrated that control nuclei were significantly more circular (Fig. 6.6F). Analysis of microarray gene expression data by David 6.7 functional annotation tool revealed enrichment of the nuclear lumen (GO:0031981; $p=3.5\times10^{-16}$, FDR $q=3.5\times10^{-15}$), nucleoplasm (GO:0005654; $p=3.6\times10^{-11}$, FDR $q=5.5\times10^{-10}$) and nuclear pore (GO:0005643; $p=1.0\times10^{-3}$, FDR $q=1.5\times10^{-2}$) cellular component gene ontologies for genes up-regulated in SNAIL cells. This result provides an evidence for molecular differences between SNAIL and control cells in their nuclear compartments and implies the role of nuclear compartments in phenotypic differences between these two cell types. Notably, several genes coding for nuclear structural proteins were differentially expressed including lamin A/C, Nesprin 2 and several Sun proteins (Fig. 6.6G). Down-regulation of lamin A was recently shown to decrease nuclear stiffness and enhance cancer cell migration (189).

6.3.5 Epithelial phenotype supports higher levels of solid stress during tumor growth

To expand against agarose gels cells must have structural stability to maintain the induced solid stress, so we sought to test if increasing this solid stress would

differentially block proliferation between control and SNAIL cells by doubling the percentage of agarose used during spheroid growth. Control cell spheroids showed a slight but insignificant decrease in spheroid area in 1.0% gels, whereas SNAIL cell spheroids in 1.0% agarose were 5-fold smaller than in 0.5% agarose ($p<0.001$, Fig. 6.7A). This indicated that the induced solid-stress affected mesenchymal SNAIL cells (86±6.2% growth inhibition) significantly more than the epithelial controls (18±1.4% growth inhibition) (Fig. 6.7B). Quantification of the solid stress exerted by the spheroids demonstrated that SNAIL cells were able to withstand a peak solid stress of ~35 mmHg regardless of gel concentration, whereas control cells were able to withstand at least 80 mmHg in stiffer gels (Fig. 6.7C).

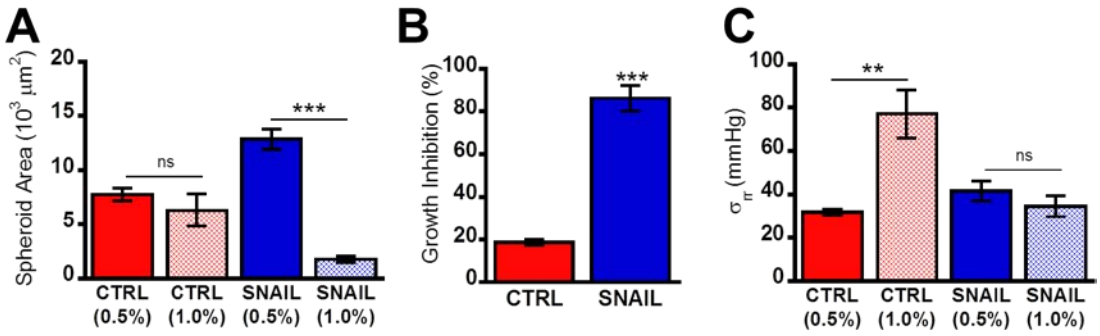

Figure 6.7 Mesenchymal SNAIL cells do not support solid stress. (A) Spheroid cross sectional area after four weeks growth in either 0.5% or 1.0% (w/v) agarose gels shows no significant difference between the two concentrations for control cells, but a dramatic decrease for SNAIL cells. (B) Four-fold higher growth inhibition from increasing solid stress by altering gel concentration in SNAIL cells. (C) Calculation of radial stress during spheroid growth shows that control cells are able to support at least 80 mmHg, whereas SNAIL cells plateau at about 50% of this value.

6.4 Discussion

Epithelial to mesenchymal transition is hypothesized to be a key step in cancer metastasis, predominately through loss of cell-cell adhesions leading to escape of cells from the primary tumor (171). However, recent studies have shown that biophysical changes may be equally important for cancer metastasis (190). To bridge the gap between these observed molecular and biophysical changes, we utilized a genetically induced model of EMT in epithelial MCF7 breast cancer cells transformed to a mesenchymal phenotype with a stable SNAIL mutant (175). As previously observed when comparing invasive and non-invasive cells (74), we found that the more motile (Fig. 6.1D-F) SNAIL cells exerted larger traction stresses on their underlying matrix (Fig. 6.2A-C). Although this result was somewhat surprising considering the decreased level of polymerized actin, we find it to be consistent with results reported by other investigators. For instance, more aggressive cancer cells are known to be soft with decreased actin polymerization (191–193) and exert larger traction forces (190). Analysis of relevant gene expression revealed key changes, consistent with those previously observed in other models of EMT, such as a concomitant up-regulation of *MYH10* (myosin IIb) and down-regulation of *MYH14* (myosin IIc) (194).We further observed up-regulation of genes that would increase contractility including myosin light chain kinase and ARHGEF3 as well as decreased expression of contractility inhibitors such as myosin phosphatase and ARHGAP1 (Fig. 2E).

In addition to the extracellular forces exerted by cells, the intracellular mechanics of cancer cells have also been shown to correlate with metastatic potential with softer cells

displaying a higher degree of invasiveness (192, 193). To determine if EMT could be responsible for this loss of cytoskeletal stiffness, we probed intracellular mechanical properties using multiple particle tracking microrheology. This analysis revealed that across all time lags particles within SNAIL cells had higher mean squared displacements indicative of a softer cytoplasm (Fig. 6.3A). Quantification of creep compliance demonstrated that SNAIL cytoplasm is deformed nearly an order of magnitude easier than their control counterparts (Fig. 6.3C). Moreover, increased effective diffusion coefficient within SNAIL cells may allow for more rapid transport of chemical signals or actin retrograde flow (Fig. 6.3B). Control cells had elastic moduli and shear viscosity mirroring other epithelial cancer cells (195), but both parameters were nearly totally abrogated following EMT (Fig. 6.3D-E).

Consistent with this loss of mechanical structure, SNAIL cells also displayed decreased polymerized actin (Fig. 6.4F). Though SNAIL cells lost this internal actin structure, they did display increased filopodium-like protrusions (Fig. 6.4B). The formation of these protrusions has been shown to be governed largely through β-parvin (*PARVB*) which we found to be up-regulated as a result of EMT (Fig. 6.4C). This effect was most likely further enhanced by increased expression of several actin nucleating/branching proteins such as ARP3 (Fig. 6.4C). Based on transcriptional analysis, the loss of actin structure was largely mediated via decreased expression of actin crosslinking proteins, not increases in actin severing proteins (Fig. 6.4C), supported by the stabilization of actin filaments only being able to partially recover the mechanical

stability of control cells (Fig. 6.5B-C). This may open the possibility for new therapeutic approaches to reduce metastatic potential of cancer cells.

Although cytoplasmic deformation is required to navigate the extracellular environment, the nuclei is the largest organelle and it's deformation is often the rate limiting step in migration (186). The nuclear relaxation following EMT (Fig. 6.6), may be important in allowing cells to navigate through small pores during migration, and in uncovering cryptic binding sites during transcription for increased gene expression (196). This nuclear softening has also been observed in stem cells (197) and supports the proposition that EMT creates stem cell-like cells (198).

Despite the body of evidence supporting the importance of EMT for cancer cells to migrate to distant sites, a continuing critique of this theory is the lack of mesenchymal signatures within secondary tumors (199). Recent studies have demonstrated that tumors *in vivo* are under mechanical solid stress and that this stress accumulates as tumors grow (52). Based on this, it reasons that softer cells would show impaired growth as this stress accumulates. Our results demonstrate that below a critical solid stress threshold, the mesenchymal SNAIL cells showed increased spheroid growth akin to the increased 2D BrdU incorporation (Fig. 6.1G-H). However, increasing the solid stress against the growing spheroids by doubling the agarose concentration effectively blocked SNAIL spheroid growth, whereas the area of control spheroids was unaffected (Fig. 6.7A). Calculation of the accumulated solid stress revealed SNAIL cells grew until reaching a maximum stress of approximately 35 mmHg regardless of gel composition, whereas

control cells were able to withstand at least 80 mmHg of stress (Fig. 6.7C). One potential mechanism for this observation is that the reduced actin cytoskeletal structure from changes in crosslinking proteins does not allow the SNAIL-transformed cells to generate enough force to push the gel out allowing for further cell division. Alternatively, this could be a byproduct of decreased *LMNA* expression which has been shown to not only expedite 3D migration, but also make cells more prone to stress-induced apoptosis (189). This inability to survive in high-stress environments could potentially explain the inability to detect mesenchymal signatures in metastatic tumors, as stress acts as a selective pressure mitigating the presence of mesenchymal cells in favor of epithelial cells that can support the growing tumor.

In conclusion, this report demonstrates that the biophysical changes including increased traction forces and loss of cytoskeletal and nuclear structure associated with cancer metastasis are directly induced by epithelial to mesenchymal transition in absence of any extraneous environmental cues. Microarray gene expression analysis revealed concerted topographical alterations in gene expression networks associated with these phenomena. Finally, we show that these pro-metastatic biophysical changes may come at the cost of survival as secondary tumors progress in size, with accumulating solid stress only allowing for the survival of cells that return to a more mechanically stable epithelial phenotype. Further understanding of this complex interplay between changes in gene expression and cell biophysical properties with implications for cancer metastasis may help develop novel targeted therapeutics.

6.5 Materials and Methods

6.5.1 Cell Culture and Phenotype Verification

Human breast carcinoma MCF7 stably transformed with either SNAIL-6SA (mutated for internuclear stability (175)) or empty vector control, both encoding for Neomycin resistance, were cultured in RPMI 1640 (Mediatech, Herndon, VA) containing 10% FBS (Atlanta Biologicals, Norcross, GA) and 400 μg/mL G418 (Sigma Aldrich, Carlsbad, CA). Cell aspect ratio was determined by manually tracing cells in ImageJ (NIH). Gene expression analysis using RT-PCR was performed using primers as previously described (68, 200). All experiments were performed on glass coated with 10μg/mL Collagen I or compliant substrates coated with Collagen I synthesized as previously described (84) with either 10% acrylamide and 0.3% bisacrylamide (hard, 34.88 kPa) or either 10% acrylamide and 0.03% bisacrylamide (soft, 2.83 kPa).

6.5.2 Cell Function Analysis

Proliferation was quantified using BrdU staining as previously described (99) by labeling with 50 μM BrdU (Sigma) for 90 minutes before staining. For motility quantification, cells were labeled with NucBlue (Invitrogen, Carlsbad, CA) per manufacturer's instructions and then imaged every 5 minutes on a Nikon Eclipse Ti inverted epifluorescent microscope equipped with an environmental chamber (In Vivo Scientific, St. Louis, MO) for 6-12 hours. Nuclei were tracked in MATLAB and traces used to determine mean velocity, defined as the average velocity over each 30 minute time interval, directional velocity, defined as the net change in position over total tracking time, and straightness, defined as the total path length over the net displacement.

Spheroids were formed by creating single-cell suspensions in either 0.5% or 1.0% low-gelling agarose and allowing them to grow for 4 weeks before labeling live cells with green fluorescent Calcein AM to quantify spheroid area. Only spheroids isolated from other spheroids by at least 2 radii were imaged. Solid stress was calculated as described (201) using a linear poroelastic model assuming no initial stress at time 0 and that stress goes to zero at an infinite distance. Spheroids with elongated morphologies were discarded as symmetric assumptions were no longer valid; the remaining population had equivalent average area (t-test $p=0.52$) and variance (F-test for equality of variances, $p=0.41$).

6.5.3 Microarray Analysis

After achieving about 80% of confluency, cells from triplicate cultures of both cell types were harvested by trypsinization; total RNA was isolated, processed to fragmented biotin-labelled cDNA, hybridized on Human Genome U133 Plus 2.0 Array (Affymetrix, Santa Clara, CA) and scanned as described in detail in the Gene Expression Omnibus repository (GEO, http://www.ncbi.nlm.nih.gov/geo/) dataset under the accession number GSE58252. Data were processed with the Expression Console software Build 1.2.1.20 (Affymetrix) using the Affymetrix default analysis setting for PLIER algorithm. Probesets that displayed absent detection calls (MAS5.0 algorithm) across all chips were removed and PLIER16 values were used to identify genes differentially expressed between SNAIL and empty vector control cells using the Significance Analysis of Microarrays (SAM) version 4.01 (202). Genes were reported as differentially expressed between SNAIL and control classes at FDR=2.12% and absolute fold change (FC) ≥ 1.5.

Probesets corresponding to differentially expressed genes were employed for enrichment analysis using the MetaCore suite 6.18 build 65505 (Thomson Reuters). Briefly, significantly perturbed pathways and process networks were identified by mapping differentially expressed genes onto manually curated GeneGO canonical pathway maps and process networks (203). Additionally, functional enrichment for up-regulated and down-regulated genes was determined using David 6.7 functional annotation tool (Laboratory of Immunopathogenesis and Bioinformatic, SAIC-Frederick, Inc.) (204, 205). In order to test for the statistical significance of enrichment, p-values were calculated based on hypergeometric distribution and corrected for multiplicity using the false discovery rate (FDR) procedure. Complementary to the differential expression and pathway enrichment analysis, the Gene Set Enrichment Analysis (GSEA) (206) was performed on PLIER16 processed data without any pre-filtering of probe sets for SNAIL and control cells, using categorical phenotype labels and signal-to-noise metrics to identify gene sets significantly enriched in specific phenotypes. Gene set permutation type and GO Biological Processes (BP) gene sets (Molecular Signatures Database v4.0; 825 gene sets) were the parameters used in this GSEA. Gene sets were considered to be significantly enriched in a given phenotype, if their q-values were ≤ FDR threshold, for which the expected number of false positive gene sets was ≤ 1. The analysis of gene expression data presented in this report is focused on solely on cell mechanics and details relevant to other functional contexts will be reported elsewhere.

6.5.4 Traction Force Cytometry

Substrates (34.88 kPa) were synthesized as above except embedded with 200nm red fluorescent particles (Invitrogen). Cells were first labeled green fluorescent with Calcein AM (Anaspec) and NucBlue (Invitrogen) per manufacturer's instructions. An initial image of the cells and the stressed gel were captured, and then the cells were lysed with 0.5% SDS before capturing a final unstressed gel image. An average of 100 cells per experiment were captured, values represent average of 3-5 experiments. Cell-induced displacements from particle images, a freely available MATLAB particle tracking algorithm (MatPIV, http://www.math.uio.no/~jks/matpiv/) was used with minor modifications and used to determine traction forces as previously described (70).

6.5.5 Intracellular Mechanics

Multiple particle tracking microrheology (MPT) was used to quantify intracellular rheology based on the thermal motion of nanoparticles (Reviewed in (177)). Cells were injected as described (169) on collagen-coated 35mm dishes and then immediately passed to collagen-coated 35mm glass bottom dishes (MatTek). Cells were allowed to adhere overnight and imaged the following day in the live-cell chamber described above with a Nikon CFI Apochromat TIRF 100X oil-immersion lens and QuantEM CCD (Princeton Instruments, Trenton, NJ) at 30 frames per second for 20 seconds. Particle displacements were tracked in MATLAB based on previous established algorithms (207) by first using a bandpass filter to isolate particles and the sub-pixel accuracy centroid was determined based on the intensity-weighted centroid. After building tracks using a Hungarian linker algorithm the time-dependent 2D particle mean squared displacements (MSDs) were calculated as $\langle \Delta r^2(\Delta t) \rangle = \langle [x(t+\Delta t)-x(t)]^2+[y(t+\Delta t)-y(t)]^2 \rangle$, which can then be used to

determine rheological properties including diffusion coefficient, creep compliance, as well as the viscous (G"(ω)) and elastic (G'(ω)) moduli (195). The ratio of viscous to elastic moduli is represented by the phase angle (δ, where $\delta = \arctan(G''(\omega)/G'(\omega))$, which ranges from 0° for an elastic solid to 90° for a viscous liquid (208). To quantify nuclear mechanics, we tracked Hoechst-labeled chromatin (187) using techniques as described above for MPT. The relaxation time was determined as when the logarithmic slope of the MSD was equal to 0.5, indicating a transition from a viscoelastic solid to a viscoelastic liquid.

6.5.6 Cytoskeletal Staining and Image Analysis

Cells were stained for F-actin with Rhodamine Phallodin (Invitrogen) as previously described (169). Images were captured at 20x magnification on an inverted Nikon Microscope with a CoolSNAP camera (Photometrics) and quantified in MATLAB. For quantification, image histograms were first adjusted to fill the entire range before applying a median filter and then segmenting by Otsu's method. Actin intensity was defined by taking the average intensity of the segmented region (cells) minus the average intensity of the non-segmented region (background) of the original, unmodified image. Confocal images were captured on a Zeiss LSM 700 confocal microscope equipped with a 63x lens and rendered in ZEN 2012 software.

6.5.7 Statistics

All studies were performed in triplicate or more. The data are reported as mean ± standard error of the mean. Statistical analysis was carried out using a student's t-test for comparison considering $p < 0.05$ to be significant (***$p<0.001$,**$p<0.01$,*$p<0.05$).

CHAPTER 7
INTERPLAY OF ACTIN FILAMENTS AND SODIUM EFFLUX IS REQUIRED FOR TUMOR CELLS TO SUPPORT SOLID STRESS

7.1 Summary

In order for a solid tumor to grow, it must be able to support the compressive stress generated as it presses against the surrounding tissue. Though the literature suggests a role for the cytoskeleton in counteracting these stresses, there has been no systematic evaluation of which filaments are responsible or to what degree. Here we show that cytoskeletal filaments are not actively supporting compressive loads in a three dimensional spheroid model. However, modulation of tonicity could induce alterations in spheroid size. We find that under compression tumor cells actively efflux sodium to decrease their intracellular tonicity and that this is reversible by blockade of sodium channel NHE1. Moreover, though polymerized actin was not actively supporting the compressive load, it is required for sodium efflux. Compression-induced cell death was increased both by sodium blockade and actin depolymerization, whereas increased actin polymerization offered protective effects and increased sodium efflux. Taken together, these results demonstrate that cancer cells modulate their tonicity to survive under compressive solid stress.

7.2 Introduction

Solid tumors grow under stress from the local tissue. This growth results in further accumulation of compressive stress in the tumor. To remain viable and grow, the tumor cells must be able to survive under these compressive stresses, which correspond with mechanical loads of 50-200 mmHg (51, 52). Previous work has shown that this solid stress prevents the growth of cancer cell spheroids (51). Moreover, as this stress accumulates *in vivo* it can lead to further adverse effects such as blood vessel compression hindering drug delivery (52). Despite the importance of solid stress in tumor growth, few studies have explored how cancer cells actually support this stress.

Most literature suggests that the ability of cells to resist deformation largely emanates from the cytoskeleton (209). A series of studies have demonstrated that actin, microtubules, and intermediate filaments all contribute to support of external compressive stresses (14, 180, 210). Supporting this, in a genetically engineered model of epithelial-mesenchymal transition we recently found that mesenchymal cells could support less stress than their epithelial counterparts, which correlated with decreased polymerized actin and cytoplasmic stiffness (109). Here we show that compressive stress is not actively supported by cytoskeletal filaments, but induces NHE1-dependent sodium efflux from the tumor cells. While actin polymerization did not actively support solid stress, depolymerization of actin also mitigated the ability of cells to efflux sodium. Taken together, this work shows that regulation of intracellular tonicity is required for cells to maintain viability under compressive stress.

7.3 Results

7.3.1 Supporters of solid stress

To analyze how cancer cells support compressive solid stress we cultured tumor spheroids from single MCF7 breast cancer cells in inert agarose gels, resulting in the accumulation of solid stress (51, 201). Next, to elucidate the roles of cytoskeletal filaments in supporting this stress we treated the spheroids with a variety of cytoskeletal stabilizing and destabilizing molecules and tracked changes in spheroid cross-sectional area using live-cell microscopy as described in the Supporting Material. Unexpectedly, depolymerization of actin filaments using Cytochalasin D resulted in an increase in spheroid size and increasing actin polymerization with Jasplakinolide had no effect, suggesting actin was not primarily responsible for supporting solid stress (Fig. 1 *A*). Modulation of microtubule polymerization did not alter spheroid diameter (Fig. 1 *B*) and depolymerization of intermediate filaments with 4 mM acrylamide (211) produced a slight increase in spheroid area (Fig. 1 *C*). Since none of these treatments produced significant decreases in spheroid area indicative of actively supporting stress, we hypothesized the stress may instead be supported by osmotic pressure. Decreasing media tonicity caused spheroid swelling while increasing media toncitiy with a variety of solutes caused spheroids to shrink (Fig. 1 *D*). Finally, to ascertain if cells in steady state spheroids have higher or lower tonicity than their surrounding media we permeabilized cells with 0.0025% Triton-X100. Following permeabilization, spheroids increased in area over 25% (Fig. 1 *E*). Based on osmotic models of cell size this implies that cells inside stressed spheroids have lower tonicity than their surrounding media, such that following

permeabilization extracellular ions enter the cells, inducing an inward water flux (and consequential spheroid swelling) to equilibrate (212).

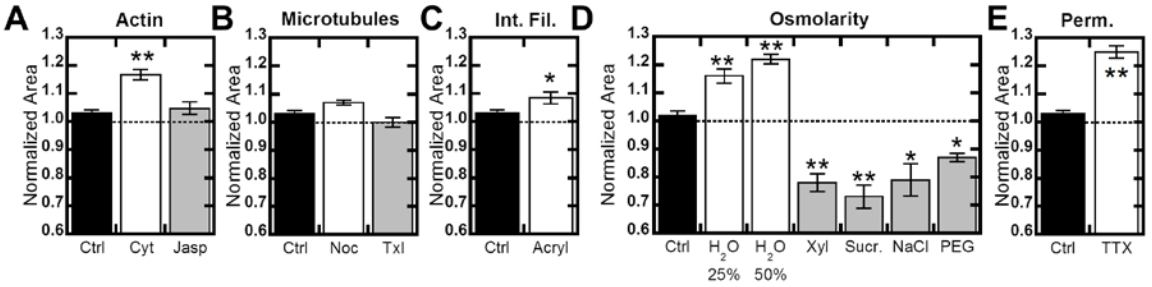

Figure 7.1 Change in spheroid area after 6 hours of treatment. All values normalized to initial area before treatment. (A) Depolymerization of actin with Cytochalasin D (Cyt) and enhanced polymerization with Jasplakinolide (Jasp). (B) Microtubule depolymerization with Nocodazole (Noc) and stabilization with Taxol (Txl). (C) Depolymerization of intermediate filaments with acrylamide. (D) Altering media osmolarity with water (hypo-osmotic), and 250 mM xylose, sucrose, NaCl, or PEG400 (hyper-osmotic). (E) Spheroid permeabilization with 0.0025% Triton-X100 (TTX). Values given ± SEM, *P<0.05, **P<0.01.

7.3.2 Sodium efflux under compressive solid stress

To ascertain how cells were decreasing their intracellular tonicity, we utilized a 2D model of solid stress. Here, instead of allowing spheroids to accumulate solid stress from growth, we used weights to directly apply a controlled stress to a monolayer of cells (213). Quantification of intracellular sodium with CoroNa Green revealed cells effluxed sodium following mechanical compression (Fig. 2 *A*). While blockade of sodium channel NKKC1 did not produce a statistically significant difference in sodium efflux under stress, inhibition of the sodium-hydrogen channel NHE1 with EIPA did significantly block sodium efflux ($p<0.05$, Fig. 2 *B*). This is consistent with previous studies showing hydrostatic pressure induces sodium efflux (214). Repeating this experiment with modulation of actin filaments revealed that actin depolymerization blocked sodium efflux

to a similar degree as NHE1 blockade. Consistent with this, actin stabilization with Jasplakinolide produced a slight but statistically insignificant (p=0.063) increase in sodium efflux (Fig. 2 *C*). These results suggest that while polymerized actin may not be actively supporting stress, it is required for cells to function properly under compression. This is consistent with recent studies showing the importance of NHE1 for confined cell migration where it colocalizes with polymerized actin (215).

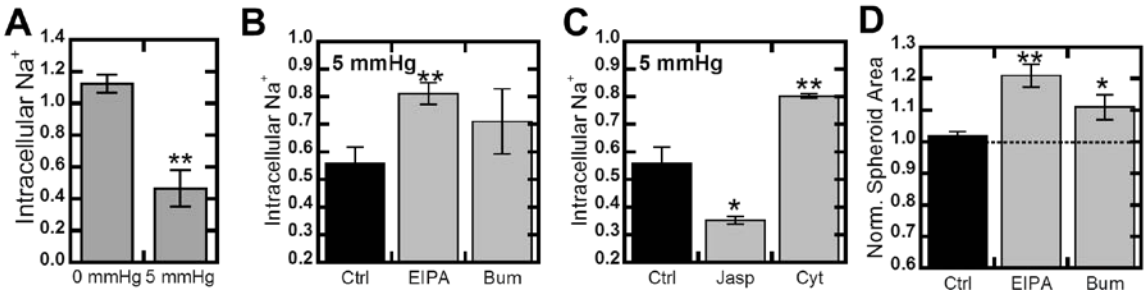

Figure 7.2 Cancer cells efflux sodium under solid stress. (A) A 2D monolayer of MCF7 cells was loaded with CoroNa Green sodium tracer and compressed with 5 mmHg solid stress for two hours. CoroNa intensity was measured using a plate reader, values are reported relative to the 0 time point. (B) Intracellular sodium under 5 mmHg stress in presence of NHE1 inhibitor EIPA and NKCC1 inhibitor Bumetanide (Bum). (C) Intracellular sodium under 5 mmHg stress in presence of Jasplakinolide (Jasp) to enhance actin polymerization and Cytochalasin D (Cyt) to depolymerize actin. (D) In 3D tumor spheroids, blockade of sodium channels NHE1 (EIPA) and NKCC1 (Bum). Values given ± SEM, *P<0.05, **P<0.01.

To verify that these results would translate into our 3D spheroid model, we repeated the spheroid assay. Blockade of NKCC1 with Bumetanide did cause modest swelling, but consistent with the sodium efflux findings NHE1 blockade with EIPA produced a larger increase in spheroid cross-sectional area (Fig. 2 *D*) identical to that seen with actin depolymerization (Fig. 1 *A*).

7.3.3 Sodium efflux, tonicity, and actin polymerization contribute to cell viability under stress

To test that the observed stress-induced sodium efflux was actually protective, we finally analyzed viability of cells under compression. In our 2D system, we found that compression with 5 mmHg induced significant cell death (Fig. 3 *A*). While cells in hypertonic media did show increased death without compression, 5 mmHg of compression did not significantly increase this death suggesting it may have been protective to the surviving cells (Fig. 3 *A*). Increasing actin polymerization with Jasplakinolide was more protective under stress, significantly decreasing cell death relative to the compressed control. Conversely, decreasing media tonicity, blocking sodium efflux, or actin depolymerization all significantly increased the amount of cell death under compression (Fig. 3 *A*).

To verify that these mechanisms were conserved in our three dimensional model, we repeated the analysis of viability following addition of EIPA and Cytochalasin D. These results are presented as the resulting cell death as a function of radial stress, (Fig. 3 *B*). If these molecules induce compressive stress-dependent toxicity, then we should see increasing cell death as a function of radial stress in the spheroids. In the control condition, there is a weak positive correlation between radial stress and cell death, which is subsequently increased by NHE1 inhibition and even further by actin depolymerization demonstrating the both are required for tumor cells to survive under stress.

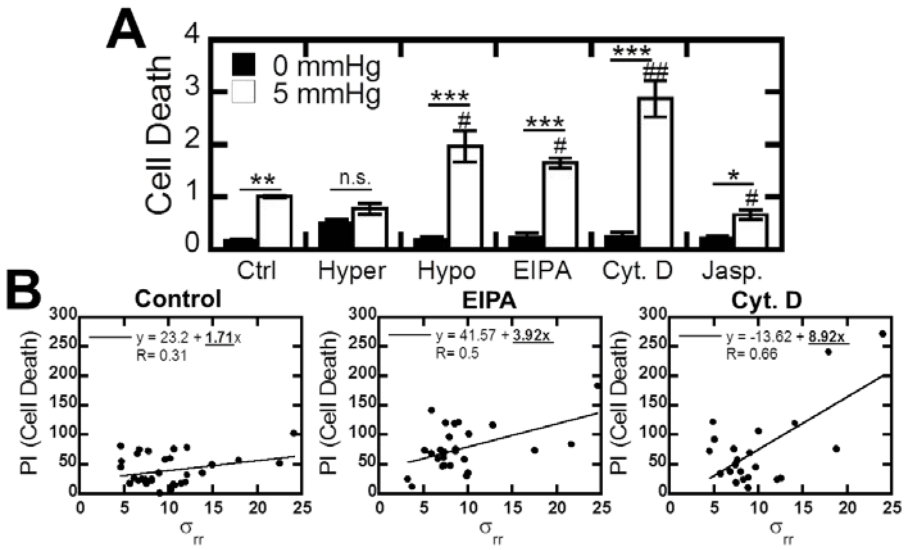

Figure 7.3 Sodium efflux and actin polymerization are required for viability under solid stress. (A) Quantification of cell death based on ratio of propidium iodide to Calcein AM after 4 hours of compression of 2D monolayer. Hyper (250 mM Xylose); Hypo (25% H2O); Cytochalasin D (Cyt); Jasplakinolide (Jasp). (B) Cell death in 3D tumor spheroids versus radial stress. Stress-dependent toxicity is indicated by slope value. Values given ± SEM, # indicates significance to stressed control, *P<0.05, **P<0.01, ***P<0.001

7.4 Discussion

Cells use ion pumps to maintain a constant volume by modulating their tonicity and subsequently osmotic pressure (216). Here, we document that when under compressive stress multi-cell spheroids as well as cell monolayers will similarly efflux sodium, decreasing intracellular tonicity, and increasing viability under stress. This finding is consistent with the work of Hui et. al. who found that increased hydrostatic pressure induced active sodium efflux (214). Recent studies using *C. elegans* suggest these organisms may have an absolute internal pressure set point (217). This could be consistent with the model of cell volume and pressure regulation present by Jiang et. al.,

which relates changes in cell volume to water flux, controlled by the differences in hydrostatic and osmotic pressure across the cell membrane (212). The lower steady state intracellular tonicity under stress implies a negative pressure change across the cell membrane from osmotic pressure. This negative pressure change may help offset the compressive stress. Taken together, this work demonstrates that to survive under compressive stress cells must be able to modulate their tonicity by effluxing sodium, and that polymerized actin is necessary for this process.

7.5 Materials and Methods

7.5.1 Cell Culture and Spheroid Generation

Human breast carcinoma MCF7 (ATCC, Manassas, VA) were cultured in RPMI 1640 (Mediatech, Herndon, VA) containing 10% FBS (Atlanta Biologicals, Norcross, GA). Spheroids were generated by creating a single-cell suspension in 0.75% low-gelling agarose (Type VIIA, Sigma-Aldrich, St. Louis, MO) and allowing them to grow for 3 weeks (201).

7.5.2 Chemical Perturbations

For hypotonic media, DI water was added to 25-50% v/v, for hypertonic media Xylose (Spectrum), Sucrose (BDH), NaCl (Amresco) or PEG400 (TCI) were added to final concentration of 250 mM. Chemical inhibitors were used at the following concentrations:

Table 7.1 Chemical inhibitors used in study

Chemical	Manufacturer	Concentration	Effect
Cytochalasin D	Enzo	1 μM	Depolymerize actin
Jasplakinolide	Enzo	100 nM	Increase actin polymerization
Nocodazole	Sigma	20 μM	Depolymerize microtubules
Taxol	Enzo	100 nM	Stabilize microtubules
Acrylamide	Acros Organics	4 mM	Depolymerize intermediate filaments
Triton-X100	BioRad	0.0025%	Permeabilize cells
EIPA	Enzo	50 μM	Blocks sodium channel NHE1
Bumetanide	Enzo	20 μM	Blocks sodium channel NKCC1

7.5.3 3D Spheroid Compression Model

After 3 weeks of growth to accumulate solid stress, spheroids were analyzed by live-cell microscopy on a Nikon Eclipse Ti inverted epifluorescent microscope, maintained at 37° C and 5% carbon dioxide throughout the experiment using an In Vivo Scientific environmental cell chamber and Bioscience Tools CO_2 controller. After capturing initial images of spheroids, spheroids were treated with inhibitors described above and returned to the microscope for continued imaging. Spheroid areas were manually traced, the value given represents the spheroid area 6 hours post treatment normalized to the initial area. Solid stress was determined as previously described (201). In brief, the deformation in the gel is determined from the final spheroid size relative to the initial radius of the single cells they originated from (taken to be 5 μm), and this deformation can be used to determine stresses based on the known mechanical properties of agarose.

7.5.4 2D Compression Model

Cells were grown as a monolayer and then compressed with weighted pistons as previously described (213). After reaching 80% of confluence, monolayers were washed with PBS and a 2% agarose solution and flattened using a custom well plate insert. After polymerization, this agarose cushion was topped with media and allowed to equilibrate in standard culture conditions. To apply stress, custom pistons that applied 5 mmHg of solid stress (piston weight divided the piston surface area) were then added and incubated for desired period of time. Unstressed controls were topped with coverslips of equal size to the pistons to account for differences in oxygen diffusion.

7.5.5 Live-Dead Quantification

In order to quantify cell viability, cells were labeled with 10 μg/mL propidium iodide and 2 μM Calcein AM (Enzo) to identify dead and live cells, respectively. Images were then collected on a Nikon Eclipse Ti inverted epifluorescent microscope as described above. Image analysis was then performed in MATLAB, taking cell death as total propidium iodide signal normalized to total Calcein signal. For 2D studies, cells were pre-treated with inhibitors for 2 hours before applying stress for 4 hours. For 3D studies, spheroids were incubated with inhibitors for 6 hours before performing analysis.

7.5.6 Intracellular Sodium

Intracellular sodium was measured using CoroNa Green (Invitrogen, Carlsbad, CA) per manufacturer's instructions. Individual aliquots were solubilized to 1 mM in DMSO. Cell monolayers were washed twice with HBSS before incubation in 10 μM CoroNa green in HBSS for 45 minutes. Cells were washed two more times before returning to

growth media, and then treated as described in the 2D compression model. For quantification, wells were read on a DTX-800 Multimode Detector microwell plate reader (Beckman Coulter) at 485nm excitation, 535nm emission. An initial reading was taken before applying 5 mmHg stress (or coverslip control) and then a final reading taken two hours later after removing weights. Values are reported as final CoroNa signal normalized to initial signal after blank subtraction.

7.5.6 Statistics

All studies were performed in triplicate or more. The data are reported as mean ± standard error of the mean. Statistical analysis was carried out using a student's t-test for comparison considering $p < 0.05$ to be significant (***$p<0.001$,**$p<0.01$,*$p<0.05$).

CHAPTER 8
CONCLUSIONS

8.1 Ovarian Cancer Tropism for Compliant Matrices

Although extensive studies have focused on improving the detection and treatment of ovarian cancer, it remains the fifth leading cause of cancer deaths among women (60). Ovarian cancer is not detected until after spread from the primary site in 85% of patients (54). Once it has spread, or metastasized, most therapies often fail to cure even patients with initially chemosensitive tumors (218). As the cancer disseminates from the primary tumor, it almost universally metastasizes to the soft peritoneal fat pad (219), but there remains a scarcity of studies understanding the mechanisms underlying this metastatic tropism. This study offers new mechanistic insight into the process of ovarian cancer metastasis.

Previous studies have offered chemical explanations for ovarian cancer's predisposition to metastasize to soft tissues (58). However, our results show that it might also be the mechanical properties of the soft tissue influencing this tropism. This hypothesis is supported by other work showing growth on matrices of varying rigidities is indicative of tissue tropism (61). Moreover, microarray analysis between ovarian carcinomas and metastases to the omentum show few genetic perturbations (220). Though this could be explained by the more passive mechanism by which ovarian cancer cells enter the peritoneum, our findings suggest that ovarian cancer simply does not need additional genetic mutations to thrive in soft tissues; it already prefers the decreased

rigidity. This latent ability for ovarian cancer to thrive in the surrounding soft tissues may also help explain why ovarian cancer is often diagnosed late stage.

Previous work using 3D scaffolds noted ovarian cancer cells showed decreased chemosensitivity in 3D compared to 2D (73), attributed to the difference in dimensionality. However, these scaffolds were also much more compliant than 2D tissue culture plastic which could imply the altered mechanosensitivity is merely due to changes in matrix stiffness. Notably, the decreased chemosensitivity observed moving from 2D to 3D closely mirrored that observed in our study. This result suggests that more accurate models may be created using only two dimensional substrates allowing for easier screening while maintaining the more realistic results found with compliant 3D scaffolds. In order for drug screening on compliant substrates to be feasible, it would require synthesis of substrates directly in a 96 or 384 well microplate as opposed to the individual glass coverslips used in this study. While some effort has been made to produce these gels in microplates (97), it still required the use of glass bottom dishes that would be prohibitively expensive for any meaningful scale up. A cheaper alternative synthesized in standard tissue culture plastic dishes would be required. Tissue culture plastic is polystyrene that has been surface oxidized by plasma treatment. This surface could be reacted with the strong reducing agent hydrazine (N_2H_4) resulting in presentation of free amine groups on the surface. Once free amine groups are present, standard substrate synthesis protocols could be followed starting at the glutaraldehyde step. In the simplest case, microplates could be synthesized with a single substrate rigidity to test a larger number of drugs. Alternatively, microplates could be synthesized

with a gradient of rigidities to test how drug efficacy varies across multiple substrate rigidities. The gradient may be created by varying the gel composition, or by use of a photomask and photo-activated cross-linker. These compliant substrates could allow for drug screening more representative of *in vivo* at a cost economical enough to allow for large-scale drug testing.

8.2 Mechanisms of Cancer Mechanosensitivity

An array of studies have highlighted how breast cancer advances on stiff matrices through Rho/ROCK (8, 37, 92, 93), and this study as well as others (73) shows that ovarian cancer cells grow better on soft matrices. This disparity poses the question that originally motivated these studies: what is the difference? Initial analysis of microarray data showed differential regulation of contractile pathways, with higher latent contractility being linked with a preference for a stiffer matrix. Chemical perturbation of these pathways verified that that a “hard-tropic” or “soft-tropic” phenotype could be induced by activation or blockade of these contractile pathways.

In a broader context, this work further supports the idea of matrix stiffness as an additional ingredient in the ‘soil’ (or microenvironment) required for growth of the seeds (or metastatic cancer cells), as proposed by Stephen Paget nearly a century ago (221). The past decade has produced monumental advances in our knowledge of what specific molecular factors contribute to these observed tissue affinities, or tropism, of metastatic cancer cells. Notably, a series of studies by Massagué and colleagues compared breast cancer subclones that preferentially accumulate in one of the three main breast cancer

metastatic sites (brain, lung, bone) to their parent lines to understand what gave these cells the ability to colonize specific sites (89–91). These studies revealed location-specific adaptations like higher expression of key molecules for adhesion and extravasation into the secondary site as well as growth factor receptors that aid in homing and survival. Interestingly, in these isolated subclones we see similar higher expression of contractile genes in the clones that metastasized to bone compared to those that metastasized to lung tissue (Fig. 4.5). Based on these findings taken together, we postulate that after gaining the ability to invade the secondary site, adhere to the surrounding ECM, and respond to local growth factors metastatic cells must also adapt to the rigidity of the secondary site, largely through regulation of cytoskeletal tension. While we found that cells from different systems (e.g. MDA-MB-231 vs SKOV-3, bone metastatic vs lung metastatic cells, etc.) up-regulated contractility through some conserved pathways they also used many unique pathways to increase or decrease contractility.

Future studies aimed at developing a “tropic gene expression signature” using these contractility pathways, along with relevant adhesive ligands and other adaptions necessary for metastasis may prove useful in predicting and targeting metastasis from primary tumor biopsies. Alternatively, since many of these pathways are regulated by activity a proteomics such as reverse-phase protein array approach looking at phosphorylation of relevant proteins may produce a more accurate metastatic signature (222). Moreover, additional mechanistic studies focused on understanding how these signals from the extracellular matrix and translated into growth signals may illuminate

novel therapeutic targets. This also may be accomplished using proteomic approaches to identify differentially regulated proteins, or by using siRNA screening of cells grown on soft and hard substrates to determine what pathways are important for mechanosensitive growth. Integrating the rigidity-dependent siRNA screen with the cell motility assay would enable a high-throughput automated method to analyze entire cell populations. Preliminary studies to demonstrate the feasibility of high-throughput motility screening were performed using serial dilutions of pre-clinical cancer drugs (Fig. 8.1). When culturing ovarian cancer cells on soft substrates, we observed the largest increases in the top 1% most motile cells (Fig. 3.4A), which may represent the subpopulation capable of metastasis. These cells may be difficult to detect using bulk molecular methods, but could easily be identified using single cell motility analysis.

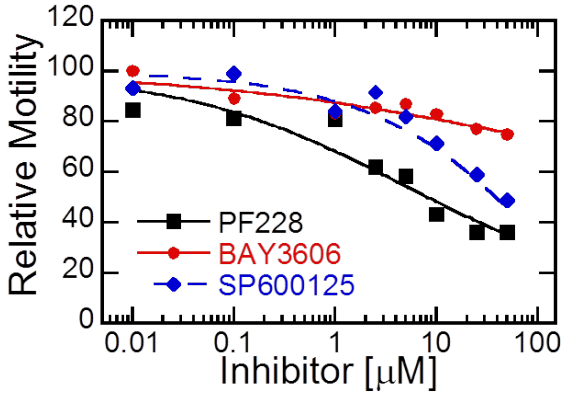

Figure 8.1 High-throughput motility analysis proof of concept. Cells were treated with serial dilution of inhibitors for focal adhesion kinase (PF228), SYK (BAY3606) and JNK (SP600125) in a 96 well plate and tracked as described in section 4.5.5 except images were collected every 15 minutes. Values represent the average of 100-300 cells from duplicate wells, all values normalized to solvent-treated control cells.

8.3 EMT and 3D Solid Stress

Despite the body of evidence supporting the importance of EMT for cancer cells to migrate to distant sites, a continuing critique of this theory is the lack of mesenchymal signatures within secondary tumors (199). Recent studies have demonstrated that tumors *in vivo* are under mechanical solid stress and that this stress accumulates as tumors grow (52). Our results demonstrate that below a critical solid stress threshold, the mesenchymal SNAIL cells showed increased spheroid growth akin to the increased 2D proliferation (Fig. 6.1G-H). However, increasing the solid stress against the growing spheroids by doubling the agarose concentration effectively blocked SNAIL spheroid growth, whereas the area of control spheroids was unaffected (Fig. 6.7A). Calculation of the accumulated solid stress revealed SNAIL cells grew until reaching a maximum stress of approximately 35 mmHg regardless of gel composition, whereas control cells were able to support at least 80 mmHg of stress (Fig. 6.7C).

One potential mechanism for this observation is that the reduced actin cytoskeletal structure from changes in crosslinking proteins does not allow the SNAIL-transformed cells to generate enough force to push the gel out allowing for further cell division. Follow-up studies tested this hypothesis by depolymerizing cytoskeletal filaments in spheroids under solid stress, but found that neither actin nor any other filament was actively supporting this compressive stress (Fig. 7.1). Instead, we found that cells actively modulated their tonicity under compressive stress by effluxing sodium (Fig. 7.2). Notably, while actin was not directly supporting solid stress actin polymerization it was required for proper sodium efflux, validating the role of cytoskeletal integrity in

supporting solid stress. This finding is consistent with the work of Hui et. al. who found that increased hydrostatic pressure induced active sodium efflux (214) and Stewart et. al. who showed osmotic pressure is critical for mitotic rounding and cell division (223). Additional work should be performed to determine if the osmotic regulation to solid stress observed here in cancer cells is also present in non-malignant cells. This could have implications in diverse fields such as tissue engineering when trying to re-create cartilage, as chondrocytes are also routinely exposed to high levels of stress. Moreover, this work observed a disparate toxicity response to inhibitors such as EIPA and Cytochalasin D under solid stress compared to normal culture conditions. Introducing this 3D spheroid model during cancer drug screening could help recapitulate mechanical factors of the tumor microenvironment and lead to more accurate pre-clinical testing.

Future studies analyzing the role of stromal cells in support of tumor solid stress would be required before transitioning to animal models. Not only can stromal cells deposit matrix which may help support stress (224), they are also naturally stiffer than cancer cells and undergo further stiffening when exposed to tumor secreted soluble factors (68, 109). A final follow-up study analyzing this phenomenon *in vivo* could verify osmotic regulation as a therapeutic target. Sodium channel blockade using EIPA, a derivative of the clinically used diuretic amiloride, was sufficient to induce cell death under solid stress in this 3D model. Either EIPA or amiloride could be used to test the effects on tumor growth *in vivo* using a xenograft model, and with previous FDA approval would be easy to translate to the clinic if successful.

REFERENCES

1. Hanahan, D., and R. Weinberg. 2000. The hallmarks of cancer. Cell. 100: 57–70.

2. Van der Veldt, A. a M., M. Lubberink, I. Bahce, M. Walraven, M.P. de Boer, et al. 2012. Rapid decrease in delivery of chemotherapy to tumors after anti-VEGF therapy: implications for scheduling of anti-angiogenic drugs. Cancer Cell. 21: 82–91.

3. Conley, S.J., E. Gheordunescu, P. Kakarala, B. Newman, H. Korkaya, et al. 2012. Antiangiogenic agents increase breast cancer stem cells via the generation of tumor hypoxia. Proc. Natl. Acad. Sci. U. S. A. 109: 2784–9.

4. Lee, S.L.C., P. Rouhi, L. Dahl Jensen, D. Zhang, H. Ji, et al. 2009. Hypoxia-induced pathological angiogenesis mediates tumor cell dissemination, invasion, and metastasis in a zebrafish tumor model. Proc. Natl. Acad. Sci. U. S. A. 106: 19485–90.

5. Goel, S., A.H.-K. Wong, and R.K. Jain. 2012. Vascular normalization as a therapeutic strategy for malignant and nonmalignant disease. Cold Spring Harb. Perspect. Med. 2: a006486.

6. Fidler, I. 2003. The pathogenesis of cancer metastasis: the “seed and soil”hypothesis revisited. Nat Rev Cancer. 3: 1–6.

7. Khaled, W., S. Reichling, O.T. Bruhns, H. Boese, M. Baumann, et al. 2004. Palpation imaging using a haptic system for virtual reality applications in medicine. Stud. Health Technol. Inform. 98: 147–53.

8. Paszek, M.J., N. Zahir, K.R. Johnson, J.N. Lakins, G.I. Rozenberg, et al. 2005. Tensional homeostasis and the malignant phenotype. Cancer Cell. 8: 241–54.

9. Akiri, G., E. Sabo, H. Dafni, Z. Vadasz, Y. Kartvelishvily, et al. 2003. Lysyl Oxidase-related Protein-1 Promotes Tumor Fibrosis and Tumor Progression in Vivo Lysyl Oxidase-related Protein-1 Promotes Tumor Fibrosis and Tumor Progression. : 1657–1666.

10. Mehlen, P., and A. Puisieux. 2006. Metastasis: a question of life or death. Nat. Rev. Cancer. 6: 449–58.

11. Jaalouk, D.E., and J. Lammerding. 2009. Mechanotransduction gone awry. Nat. Rev. Mol. Cell Biol. 10: 63–73.

12. Orr, a W., B.P. Helmke, B.R. Blackman, and M. a Schwartz. 2006. Mechanisms of mechanotransduction. Dev. Cell. 10: 11–20.

13. Hall, A. 2009. The cytoskeleton and cancer. Cancer Metastasis Rev. 28: 5–14.

14. Brangwynne, C.P., F.C. MacKintosh, S. Kumar, N. a Geisse, J. Talbot, et al. 2006. Microtubules can bear enhanced compressive loads in living cells because of lateral reinforcement. J. Cell Biol. 173: 733–41.

15. Janmey, P. a, U. Euteneuer, P. Traub, and M. Schliwa. 1991. Viscoelastic properties of vimentin compared with other filamentous biopolymer networks. J. Cell Biol. 113: 155–60.

16. Horwitz, A.R. 2012. The origins of the molecular era of adhesion research. Nat. Rev. Mol. Cell Biol. 13: 805–811.

17. Jean, C., P. Gravelle, J.-J. Fournie, and G. Laurent. 2011. Influence of stress on extracellular matrix and integrin biology. Oncogene. 30: 2697–706.

18. Liu, S., D. a Calderwood, and M.H. Ginsberg. 2000. Integrin cytoplasmic domain-binding proteins. J. Cell Sci. 113 (Pt 2: 3563–71.

19. Gumbiner, B.M. 2005. Regulation of cadherin-mediated adhesion in morphogenesis. Nat. Rev. Mol. Cell Biol. 6: 622–34.

20. Ratheesh, A., and A.S. Yap. 2012. A bigger picture: classical cadherins and the dynamic actin cytoskeleton. Nat. Rev. Mol. Cell Biol. 13: 673–679.

21. Maruthamuthu, V. 2011. Cell-ECM traction force modulates endogenous tension at cell–cell contacts. Proc. …. 108: 4708–4713.

22. Thiery, J.P., H. Acloque, R.Y.J. Huang, and M.A. Nieto. 2009. Epithelial-mesenchymal transitions in development and disease. Cell. 139: 871–90.

23. Thiery, J.P., and J.P. Sleeman. 2006. Complex networks orchestrate epithelial-mesenchymal transitions. Nat. Rev. Mol. Cell Biol. 7: 131–42.

24. Hotary, K., X.-Y. Li, E. Allen, S.L. Stevens, and S.J. Weiss. 2006. A cancer cell metalloprotease triad regulates the basement membrane transmigration program. Genes Dev. 20: 2673–86.

25. Lauffenburger, D. a, and a F. Horwitz. 1996. Cell migration: a physically integrated molecular process. Cell. 84: 359–69.

26. Parsons, J.T., A.R. Horwitz, and M. a Schwartz. 2010. Cell adhesion: integrating cytoskeletal dynamics and cellular tension. Nat. Rev. Mol. Cell Biol. 11: 633–43.

27. Kaverina, I., O. Krylyshkina, and J.V. Small. 2002. Regulation of substrate adhesion dynamics during cell motility. Int. J. Biochem. Cell Biol. 34: 746–61.

28. Holle, A.W., and A.J. Engler. 2011. More than a feeling: discovering, understanding, and influencing mechanosensing pathways. Curr. Opin. Biotechnol. 22: 648–54.

29. Schwartz, M.A. 2010. Integrins and extracellular matrix in mechanotransduction. Cold Spring Harb. Perspect. Biol. 2: a005066.

30. Riveline, D., E. Zamir, N.Q. Balaban, U.S. Schwarz, T. Ishizaki, et al. 2001. Focal contacts as mechanosensors: externally applied local mechanical force induces growth of focal contacts by an mDia1-dependent and ROCK-independent mechanism. J. Cell Biol. 153: 1175–86.

31. Grashoff, C., B.D. Hoffman, M.D. Brenner, R. Zhou, M. Parsons, et al. 2010. Measuring mechanical tension across vinculin reveals regulation of focal adhesion dynamics. Nature. 466: 263–6.

32. Del Rio, A., and R. Perez-Jimenez. 2009. Stretching single talin rod molecules activates vinculin binding. Sci. …. 323: 638–641.

33. Pasapera, A.M., I.C. Schneider, E. Rericha, D.D. Schlaepfer, and C.M. Waterman. 2010. Myosin II activity regulates vinculin recruitment to focal adhesions through FAK-mediated paxillin phosphorylation. J. Cell Biol. 188: 877–90.

34. Lim, Y., S.-T. Lim, A. Tomar, M. Gardel, J. a Bernard-Trifilo, et al. 2008. PyK2 and FAK connections to p190Rho guanine nucleotide exchange factor regulate RhoA activity, focal adhesion formation, and cell motility. J. Cell Biol. 180: 187–203.

35. Narumiya, S., M. Tanji, and T. Ishizaki. 2009. Rho signaling, ROCK and mDia1, in transformation, metastasis and invasion. Cancer Metastasis Rev. 28: 65–76.

36. Danen, E.H., P. Sonneveld, a Sonnenberg, and K.M. Yamada. 2000. Dual stimulation of Ras/mitogen-activated protein kinase and RhoA by cell adhesion to fibronectin supports growth factor-stimulated cell cycle progression. J. Cell Biol. 151: 1413–22.

37. Levental, K.R., H. Yu, L. Kass, J.N. Lakins, M. Egeblad, et al. 2009. Matrix crosslinking forces tumor progression by enhancing integrin signaling. Cell. 139: 891–906.

38. Zhao, X.-H., C. Laschinger, P. Arora, K. Szászi, A. Kapus, et al. 2007. Force activates smooth muscle alpha-actin promoter activity through the Rho signaling pathway. J. Cell Sci. 120: 1801–9.

39. Samuel, M.S., J.I. Lopez, E.J. McGhee, D.R. Croft, D. Strachan, et al. 2011. Actomyosin-mediated cellular tension drives increased tissue stiffness and β-catenin activation to induce epidermal hyperplasia and tumor growth. Cancer Cell. 19: 776–91.

40. Silver, F.H., L.M. Siperko, and G.P. Seehra. 2003. Review Mechanobiology of force transduction in dermal tissue. : 3–23.

41. Jiang, L., X. Liu, A. Kolokythas, J. Yu, A. Wang, et al. 2010. Downregulation of the Rho GTPase signaling pathway is involved in the microRNA-138-mediated inhibition of cell migration and invasion in tongue squamous cell carcinoma. Int. J. Cancer. 127: 505–12.

42. YOUNG, J.S., C.E. LUMSDEN, and A.L. STALKER. 1950. The significance of the tissue pressure of normal testicular and of neoplastic (Brown-Pearce carcinoma) tissue in the rabbit. J. Pathol. Bacteriol. 62: 313–33.

43. Jain, R.K. 1987. Transport of molecules across tumor vasculature. Cancer Metastasis Rev. 6: 559–93.

44. Jain, R.K. 1987. Transport of molecules in the tumor interstitium: a review. Cancer Res. 47: 3039–51.

45. Heldin, C.-H., K. Rubin, K. Pietras, and A. Ostman. 2004. High interstitial fluid pressure - an obstacle in cancer therapy. Nat. Rev. Cancer. 4: 806–13.

46. Curti, B.D., W.J. Urba, W.G. Alvord, J.E. Janik, J.W. Smith, et al. 1993. Interstitial pressure of subcutaneous nodules in melanoma and lymphoma patients: changes during treatment. Cancer Res. 53: 2204–7.

47. Milosevic, M., A. Fyles, D. Hedley, M. Pintilie, W. Levin, et al. 2001. Interstitial fluid pressure predicts survival in patients with cervix cancer independent of clinical prognostic factors and tumor oxygen measurements. Cancer Res. 61: 6400–5.

48. Roh, H.D., Y. Boucher, S. Kalnicki, R. Buchsbaum, W.D. Bloomer, et al. 1991. Interstitial hypertension in carcinoma of uterine cervix in patients: possible correlation with tumor oxygenation and radiation response. Cancer Res. 51: 6695–8.

49. Provenzano, P.P., C. Cuevas, A.E. Chang, V.K. Goel, D.D. Von Hoff, et al. 2012. Enzymatic targeting of the stroma ablates physical barriers to treatment of pancreatic ductal adenocarcinoma. Cancer Cell. 21: 418–29.

50. Cheng, G., J. Tse, R.K. Jain, and L.L. Munn. 2009. Micro-environmental mechanical stress controls tumor spheroid size and morphology by suppressing proliferation and inducing apoptosis in cancer cells. PLoS One. 4: e4632.

51. Helmlinger, G., P.A. Netti, H.C. Lichtenbeld, R.J. Melder, and R.K. Jain. 1997. Solid stress inhibits the growth of multicellular tumor spheroids. Nat. Biotechnol. 15: 778–783.

52. Stylianopoulos, T., J.D. Martin, M. Snuderl, F. Mpekris, S.R. Jain, et al. 2013. Co-evolution of solid stress and interstitial fluid pressure in tumors during progression: Implications for vascular collapse. Cancer Res. : 3833–3841.

53. Stylianopoulos, T., J.D. Martin, V.P. Chauhan, S.R. Jain, B. Diop-Frimpong, et al. 2012. Causes, consequences, and remedies for growth-induced solid stress in murine and human tumors. Proc. Natl. Acad. Sci. U. S. A. 109: 15101–8.

54. Jemal, A., R. Siegel, J. Xu, and E. Ward. 2010. Cancer statistics, 2010. CA. Cancer J. Clin. 60: 277–300.

55. Thomas, E., F. a. Holmes, T.L. Smith, A.U. Buzdar, D.K. Frye, et al. 2004. The use of alternate, non-cross-resistant adjuvant chemotherapy on the basis of pathologic response to a neoadjuvant doxorubicin-based regimen in women with operable breast cancer: Long-term results from a prospective randomized trial. J. Clin. Oncol. 22: 2294–2302.

56. Kumar, S., H. Mahdi, C. Bryant, J.P. Shah, G. Garg, et al. 2010. Clinical trials and progress with paclitaxel in ovarian cancer. Int. J. Womens. Health. 2: 411–27.

57. Coleman, R., B. Monk, A. Sood, and T. Herzog. 2013. Latest research and treatment of advanced-stage epithelial ovarian cancer. Nat. Rev. Clin. Oncol. 10: 211–224.

58. Nieman, K.M., H. a Kenny, C. V Penicka, A. Ladanyi, R. Buell-Gutbrod, et al. 2011. Adipocytes promote ovarian cancer metastasis and provide energy for rapid tumor growth. Nat. Med. 17: 1498–503.

59. Tilghman, R.W., E.M. Blais, C.R. Cowan, N.E. Sherman, P.R. Grigera, et al. 2012. Matrix rigidity regulates cancer cell growth by modulating cellular metabolism and protein synthesis. PLoS One. 7: e37231.

60. Landen, C.N., M.J. Birrer, and A.K. Sood. 2008. Early events in the pathogenesis of epithelial ovarian cancer. J. Clin. Oncol. 26: 995–1005.

61. Kostic, A., C.D. Lynch, and M.P. Sheetz. 2009. Differential matrix rigidity response in breast cancer cell lines correlates with the tissue tropism. PLoS One. 4: e6361.

62. Samani, A., J. Zubovits, and D. Plewes. 2007. Elastic moduli of normal and pathological human breast tissues: an inversion-technique-based investigation of 169 samples. Phys. Med. Biol. 52: 1565–76.

63. Tse, J.R., and A.J. Engler. 2010. Preparation of hydrogel substrates with tunable mechanical properties. Curr. Protoc. Cell Biol. Chapter 10: Unit 10.16.

64. Slack-Davis, J.K., K. a Atkins, C. Harrer, E.D. Hershey, and M. Conaway. 2009. Vascular cell adhesion molecule-1 is a regulator of ovarian cancer peritoneal metastasis. Cancer Res. 69: 1469–76.

65. Domcke, S., R. Sinha, D. a. Levine, C. Sander, and N. Schultz. 2013. Evaluating cell lines as tumour models by comparison of genomic profiles. Nat. Commun. 4: 1–10.

66. Ali, A.Y., M.R. Abedini, and B.K. Tsang. 2012. The oncogenic phosphatase PPM1D confers cisplatin resistance in ovarian carcinoma cells by attenuating checkpoint kinase 1 and p53 activation. Oncogene. 31: 2175–86.

67. Salani, R., R.J. Kurman, R. Giuntoli, G. Gardner, R. Bristow, et al. 2008. Assessment of TP53 mutation using purified tissue samples of ovarian serous carcinomas reveals a higher mutation rate than previously reported and does not correlate with drug resistance. Int. J. Gynecol. Cancer. 18: 487–91.

68. McGrail, D.J., K.M. McAndrews, and M.R. Dawson. 2013. Biomechanical analysis predicts decreased human mesenchymal stem cell function before molecular differences. Exp. Cell Res. 319: 684–96.

69. Dickinson, R.B., and R.T. Tranquillo. 1993. Optimal estimation of cell movement indices from the statistical analysis of cell tracking data. AIChE J. 39: 1995–2010.

70. Sabass, B., M.L. Gardel, C.M. Waterman, and U.S. Schwarz. 2008. High resolution traction force microscopy based on experimental and computational advances. Biophys. J. 94: 207–20.

71. Raab, M., J. Swift, P.C.D. P. Dingal, P. Shah, J.-W. Shin, et al. 2012. Crawling from soft to stiff matrix polarizes the cytoskeleton and phosphoregulates myosin-II heavy chain. J. Cell Biol. 199: 669–383.

72. Darling, E.M., M. Topel, S. Zauscher, T.P. Vail, and F. Guilak. 2008. Viscoelastic properties of human mesenchymally-derived stem cells and primary osteoblasts, chondrocytes, and adipocytes. J. Biomech. 41: 454–64.

73. Loessner, D., K.S. Stok, M.P. Lutolf, D.W. Hutmacher, J. a Clements, et al. 2010. Bioengineered 3D platform to explore cell-ECM interactions and drug resistance of epithelial ovarian cancer cells. Biomaterials. 31: 8494–506.

74. Kraning-Rush, C.M., J.P. Califano, and C. a Reinhart-King. 2012. Cellular traction stresses increase with increasing metastatic potential. PLoS One. 7: e32572.

75. Iwanicki, M., R. Davidowitz, M. Ng, A. Besser, T. Muranen, et al. 2011. Ovarian cancer spheroids use myosin-generated force to clear the mesothelium. Cancer Discov. 1: 144–157.

76. Jeong, K.J., S.Y. Park, K.H. Cho, J.S. Sohn, J. Lee, et al. 2012. The Rho/ROCK pathway for lysophosphatidic acid-induced proteolytic enzyme expression and ovarian cancer cell invasion. Oncogene. 31: 4279–4289.

77. Kranenburg, O., M. Poland, F.P. van Horck, D. Drechsel, a Hall, et al. 1999. Activation of RhoA by lysophosphatidic acid and Galpha12/13 subunits in neuronal cells: induction of neurite retraction. Mol. Biol. Cell. 10: 1851–7.

78. Ikenoya, M., H. Hidaka, T. Hosoya, M. Suzuki, N. Yamamoto, et al. 2002. Inhibition of rho-kinase-induced myristoylated alanine-rich C kinase substrate (MARCKS) phosphorylation in human neuronal cells by H-1152, a novel and specific Rho-kinase inhibitor. J. Neurochem. 81: 9–16.

79. Plotnikov, S.V., A.M. Pasapera, B. Sabass, and C.M. Waterman. 2012. Force Fluctuations within Focal Adhesions Mediate ECM-Rigidity Sensing to Guide Directed Cell Migration. Cell. 151: 1513–1527.

80. Engler, A., L. Bacakova, C. Newman, A. Hategan, M. Griffin, et al. 2004. Substrate Compliance versus Ligand Density in Cell on Gel Responses. Biophys. J. 86: 15–25.

81. Swift, J., I.L. Ivanovska, a. Buxboim, T. Harada, P.C.D.P. Dingal, et al. 2013. Nuclear Lamin-A Scales with Tissue Stiffness and Enhances Matrix-Directed Differentiation. Science (80-.). 341: 1240104–1240104.

82. Lili, L.N., L. V Matyunina, L.D. Walker, S.L. Wells, B.B. Benigno, et al. 2013. Molecular profiling supports the role of epithelial-to-mesenchymal transition (EMT) in ovarian cancer metastasis. J. Ovarian Res. 6: 49.

83. Rizvi, I., U. a Gurkan, S. Tasoglu, N. Alagic, J.P. Celli, et al. 2013. Flow induces epithelial-mesenchymal transition, cellular heterogeneity and biomarker modulation in 3D ovarian cancer nodules. Proc. Natl. Acad. Sci. U. S. A. 110: E1974–E1983.

84. McGrail, D.J., Q.M.N. Kieu, and M.R. Dawson. 2014. The malignancy of metastatic ovarian cancer cells is increased on soft matrices through a mechanosensitive Rho-ROCK pathway. J. Cell Sci. 127: 2621–6.

85. Tilghman, R.W., C.R. Cowan, J.D. Mih, Y. Koryakina, D. Gioeli, et al. 2010. Matrix rigidity regulates cancer cell growth and cellular phenotype. PLoS One. 5: e12905.

86. Cooper, J.A. 2002. Actin Dynamics : Tropomyosin Provides. Curr. Biol. 12: 523–525.

87. Kolega, J. 2004. Phototoxicity and photoinactivation of blebbistatin in UV and visible light. Biochem. Biophys. Res. Commun. 320: 1020–5.

88. Lengyel, E. 2010. Ovarian cancer development and metastasis. Am. J. Pathol. 177: 1053–64.

89. Kang, Y., P.M. Siegel, W. Shu, M. Drobnjak, S.M. Kakonen, et al. 2003. A multigenic program mediating breast cancer metastasis to bone. Cancer Cell. 3: 537–49.

90. Bos, P.D., X.H.-F. Zhang, C. Nadal, W. Shu, R.R. Gomis, et al. 2009. Genes that mediate breast cancer metastasis to the brain. Nature. 459: 1005–9.

91. Minn, A.J., G.P. Gupta, P.M. Siegel, P.D. Bos, W. Shu, et al. 2005. Genes that mediate breast cancer metastasis to lung. Nature. 436: 518–24.

92. Huang, S., and D.E. Ingber. 2005. Cell tension, matrix mechanics, and cancer development. Cancer Cell. 8: 175–6.

93. Wozniak, M. a, R. Desai, P. a Solski, C.J. Der, and P.J. Keely. 2003. ROCK-generated contractility regulates breast epithelial cell differentiation in response to the physical properties of a three-dimensional collagen matrix. J. Cell Biol. 163: 583–95.

94. Adorno, M., M. Cordenonsi, M. Montagner, S. Dupont, C. Wong, et al. 2009. A Mutant-p53/Smad complex opposes p63 to empower TGFbeta-induced metastasis. Cell. 137: 87–98.

95. Minotti, G., P. Menna, and E. Salvatorelli. 2004. Anthracyclines: molecular advances and pharmacologic developments in antitumor activity and cardiotoxicity. Pharmacol. Rev. 56: 185–229.

96. Nguyen, T. V, M. Sleiman, T. Moriarty, W.G. Herrick, and S.R. Peyton. 2014. Sorafenib resistance and JNK signaling in carcinoma during extracellular matrix stiffening. Biomaterials. 35: 5749–59.

97. Mih, J.D., A.S. Sharif, F. Liu, A. Marinkovic, M.M. Symer, et al. 2011. A multiwell platform for studying stiffness-dependent cell biology. PLoS One. 6: e19929.

98. Wu, Y., L. Chen, P.-S. Zheng, and B.B. Yang. 2002. Beta 1-Integrin-mediated glioma cell adhesion and free radical-induced apoptosis are regulated by binding to a C-terminal domain of PG-M/versican. J. Biol. Chem. 277: 12294–301.

99. Ulrich, T. a, E.M. de Juan Pardo, and S. Kumar. 2009. The mechanical rigidity of the extracellular matrix regulates the structure, motility, and proliferation of glioma cells. Cancer Res. 69: 4167–74.

100. Lo, C.M., H.B. Wang, M. Dembo, and Y.L. Wang. 2000. Cell movement is guided by the rigidity of the substrate. Biophys. J. 79: 144–52.

101. Pelham, R., and Y. Wang. 1997. Cell locomotion and focal adhesions are regulated by substrate flexibility. … Natl. Acad. Sci. 94: 13661–13665.

102. Mih, J., A. Marinkovic, and F. Liu. 2012. Matrix stiffness reverses the effect of actomyosin tension on cell proliferation. J. Cell Sci. 15: 5974–5983.

103. Totsukawa, G., Y. Yamakita, S. Yamashiro, D.J. Hartshorne, Y. Sasaki, et al. 2000. Distinct roles of ROCK (Rho-kinase) and MLCK in spatial regulation of MLC phosphorylation for assembly of stress fibers and focal adhesions in 3T3 fibroblasts. J. Cell Biol. 150: 797–806.

104. Nicolas, A., B. Geiger, and S. Safran. 2004. Cell mechanosensitivity controls the anisotropy of focal adhesions. Proc. Natl. Acad. Sci. 102: 12520–12525.

105. Nicolas, A., and S. Safran. 2006. Limitation of cell adhesion by the elasticity of the extracellular matrix. Biophys. J. 91: 61–73.

106. Lee, C., J. Lou, K. Wen, M. McKane, S.G. Eskin, et al. 2013. Actin depolymerization under force is governed by lysine 113:glutamic acid 195-mediated catch-slip bonds. Proc. Natl. Acad. Sci. 110: 5022–5027.

107. Zhu, C. 2013. Mechanochemitry: A Molecular Biomechanics View of Mechanosensing. Ann. Biomed. Eng. .

108. Luo, T., K. Mohan, P. a. Iglesias, and D.N. Robinson. 2013. Molecular mechanisms of cellular mechanosensing. Nat. Mater. 12: 1064–1071.

109. McGrail, D.J., R. Mezencev, Q.M.N. Kieu, J.F. McDonald, and M.R. Dawson. 2014. SNAIL-induced epithelial-to-mesenchymal transition produces concerted biophysical changes from altered cytoskeletal gene expression. FASEB J. 29: 1280–1289.

110. Hennessy, B.T., R.L. Coleman, and M. Markman. 2009. Ovarian cancer. Lancet. 374: 1371–82.

111. Agarwal, R., and S.B. Kaye. 2003. Ovarian cancer: strategies for overcoming resistance to chemotherapy. Nat. Rev. Cancer. 3: 502–16.

112. Kavallaris, M. 2010. Microtubules and resistance to tubulin-binding agents. Nat. Rev. Cancer. 10: 194–204.

113. Horwitz, S.B., D. Cohen, S. Rao, I. Ringel, H.J. Shen, et al. 1993. Taxol: mechanisms of action and resistance. J. Natl. Cancer Inst. Monogr. 15: 55–61.

114. Di Michele, M., A. Della Corte, L. Cicchillitti, P. Del Boccio, A. Urbani, et al. 2009. A proteomic approach to paclitaxel chemoresistance in ovarian cancer cell lines. Biochim. Biophys. Acta. 1794: 225–36.

115. Gonçalves, a, D. Braguer, K. Kamath, L. Martello, C. Briand, et al. 2001. Resistance to Taxol in lung cancer cells associated with increased microtubule dynamics. Proc. Natl. Acad. Sci. U. S. A. 98: 11737–42.

116. Kavallaris, M., D.Y. Kuo, C.A. Burkhart, D.L. Regl, M.D. Norris, et al. 1997. Taxol-resistant Epithelial Ovarian Tumors Are Associated with Altered Expression of Specific B-Tubulin Isotypes. J. Clin. Invest. 100: 1282–1293.

117. Cabral, F. 1981. Isolation of a taxol-resistant Chinese hamster ovary cell mutant that has an alteration in alpha-tubulin. Proc. Natl. Acad. Sci. 78: 4388–4391.

118. Zasadil, L.M., K. a. Andersen, D. Yeum, G.B. Rocque, L.G. Wilke, et al. 2014. Cytotoxicity of Paclitaxel in Breast Cancer Is due to Chromosome Missegregation on Multipolar Spindles. Sci. Transl. Med. 6: 229ra43–229ra43.

119. Wirtz, D., K. Konstantopoulos, and P.C. Searson. 2011. The physics of cancer: the role of physical interactions and mechanical forces in metastasis. Nat. Rev. Cancer. 11: 512–22.

120. Kajiyama, H., K. Shibata, M. Terauchi, M. Yamashita, K. Ino, et al. 2007. Chemoresistance to paclitaxel induces epithelial-mesenchymal transition and enhances metastatic potential for epithelial ovarian carcinoma cells. Int. J. Oncol. 31: 277–83.

121. Kenny, H., and S. Kaur. 2008. The initial steps of ovarian cancer cell metastasis are mediated by MMP-2 cleavage of vitronectin and fibronectin. J. Clin. Invest. 118: 1367–1379.

122. Vicente-Manzanares, M., and A.R. Horwitz. 2011. Adhesion dynamics at a glance. J. Cell Sci. 124: 3923–7.

123. Desgrosellier, J.S., and D. a Cheresh. 2010. Integrins in cancer: biological implications and therapeutic opportunities. Nat. Rev. Cancer. 10: 9–22.

124. Arboleda, M.J., J.F. Lyons, F.F. Kabbinavar, M.R. Bray, B.E. Snow, et al. 2003. Overexpression of AKT2/Protein Kinase B{beta} Leads to Up-Regulation of {beta}1 Integrins, Increased Invasion, and Metastasis of Human Breast and Ovarian Cancer Cells. Cancer Res. 63: 196–206.

125. Strobel, T., and S.A. Cannistra. 1999. Beta1-integrins partly mediate binding of ovarian cancer cells to peritoneal mesothelium in vitro. Gynecol. Oncol. 73: 362–7.

126. Landen, C., T. Kim, Y. Lin, and W. Merritt. 2008. Tumor-Selective Response to Antibody-Mediated Targeting of α v β 3 Integrin in Ovarian Cancer. Neoplasia. 10: 1259–1267.

127. Palazzo, A.F., C.H. Eng, D.D. Schlaepfer, E.E. Marcantonio, and G.G. Gundersen. 2004. Localized stabilization of microtubules by integrin- and FAK-facilitated Rho signaling. Science. 303: 836–9.

128. Efimov, a., N. Schiefermeier, I. Grigoriev, R. Ohi, M.C. Brown, et al. 2008. Paxillin-dependent stimulation of microtubule catastrophes at focal adhesion sites. J. Cell Sci. 121: 405–405.

129. Etienne-Manneville, S. 2013. Microtubules in cell migration. Annu. Rev. Cell Dev. Biol. 29: 471–99.

130. Debernardis, D., E. Siré, and P. De Feudis. 1997. p53 status does not affect sensitivity of human ovarian cancer cell lines to paclitaxel. Cancer Res. 57: 870–874.

131. Jang, S.H., M.G. Wientjes, and J.L. Au. 2001. Kinetics of P-glycoprotein-mediated efflux of paclitaxel. J. Pharmacol. Exp. Ther. 298: 1236–42.

132. Matov, A., K. Applegate, P. Kumar, C. Thoma, W. Krek, et al. 2010. Analysis of microtubule dynamic instability using a plus-end growth marker. Nat. Methods. 7: 761–8.

133. Ezratty, E.J., M. a Partridge, and G.G. Gundersen. 2005. Microtubule-induced focal adhesion disassembly is mediated by dynamin and focal adhesion kinase. Nat. Cell Biol. 7: 581–90.

134. Rape, A., W. Guo, and Y. Wang. 2011. Microtubule depolymerization induces traction force increase through two distinct pathways. J. Cell Sci. 124: 4233–40.

135. Elineni, K.K., and N.D. Gallant. 2013. Microtubules Mechanically Regulate Cell Adhesion Strengthening Via Cell Shape. Cell. Mol. Bioeng. 7: 136–144.

136. Bershadsky, a, a Chausovsky, E. Becker, a Lyubimova, and B. Geiger. 1996. Involvement of microtubules in the control of adhesion-dependent signal transduction. Curr. Biol. 6: 1279–89.

137. Subauste, M.C., O. Pertz, E.D. Adamson, C.E. Turner, S. Junger, et al. 2004. Vinculin modulation of paxillin-FAK interactions regulates ERK to control survival and motility. J. Cell Biol. 165: 371–81.

138. Beningo, K. a, M. Dembo, I. Kaverina, J. V Small, and Y.L. Wang. 2001. Nascent focal adhesions are responsible for the generation of strong propulsive forces in migrating fibroblasts. J. Cell Biol. 153: 881–8.

139. Slack-Davis, J.K., K.H. Martin, R.W. Tilghman, M. Iwanicki, E.J. Ung, et al. 2007. Cellular characterization of a novel focal adhesion kinase inhibitor. J. Biol. Chem. 282: 14845–52.

140. Duan, Z., D.E. Lamendola, Y. Duan, R.Z. Yusuf, and M. V Seiden. 2005. Description of paclitaxel resistance-associated genes in ovarian and breast cancer cell lines. Cancer Chemother. Pharmacol. 55: 277–85.

141. Fracasso, P.M., M.F. Brady, D.H. Moore, J.L. Walker, P.G. Rose, et al. 2001. Phase II study of paclitaxel and valspodar (PSC 833) in refractory ovarian carcinoma: a gynecologic oncology group study. J. Clin. Oncol. 19: 2975–82.

142. Penson, R.T., E. Oliva, S.J. Skates, T. Glyptis, A.F. Fuller, et al. 2004. Expression of multidrug resistance-1 protein inversely correlates with paclitaxel response and survival in ovarian cancer patients: a study in serial samples. Gynecol. Oncol. 93: 98–106.

143. Parekh, H., K. Wiesen, and H. Simpkins. 1997. Acquisition of taxol resistance via P-glycoprotein- and non-P-glycoprotein-mediated mechanisms in human ovarian carcinoma cells. Biochem. Pharmacol. 53: 461–70.

144. Orr, G. a, P. Verdier-Pinard, H. McDaid, and S.B. Horwitz. 2003. Mechanisms of Taxol resistance related to microtubules. Oncogene. 22: 7280–95.

145. Kaverina, I., O. Krylyshkina, and J.V. Small. 1999. Microtubule Targeting of Substrate Contacts Promotes Their Relaxation. J. Cell Biol. 146: 1033–1043.

146. Stehbens, S.J., M. Paszek, H. Pemble, A. Ettinger, S. Gierke, et al. 2014. CLASPs link focal-adhesion-associated microtubule capture to localized exocytosis and adhesion site turnover. Nat. Cell Biol. 16.

147. Belotti, D., M. Rieppi, M.I. Nicoletti, a M. Casazza, T. Fojo, et al. 1996. Paclitaxel (Taxol(R)) inhibits motility of paclitaxel-resistant human ovarian carcinoma cells. Clin. Cancer Res. 2: 1725–30.

148. Michael, K.E., D.W. Dumbauld, K.L. Burns, S.K. Hanks, and A.J. García. 2009. Focal adhesion kinase modulates cell adhesion strengthening via integrin activation. Mol. Biol. Cell. 20: 2508–19.

149. Salaycik, K.J., C.J. Fagerstrom, K. Murthy, U.S. Tulu, and P. Wadsworth. 2005. Quantification of microtubule nucleation, growth and dynamics in wound-edge cells. J. Cell Sci. 118: 4113–22.

150. Horiuchi, A., N. Kikuchi, R. Osada, C. Wang, A. Hayashi, et al. 2008. Overexpression of RhoA enhances peritoneal dissemination: RhoA suppression with Lovastatin may be useful for ovarian cancer. Cancer Sci. 99: 2532–9.

151. Gallant, N., K. Michael, and A. García. 2005. Cell adhesion strengthening: contributions of adhesive area, integrin binding, and focal adhesion assembly. Mol. Biol. Cell. 16: 4329–4340.

152. Gallant, N.D., and A.J. García. 2007. Model of integrin-mediated cell adhesion strengthening. J. Biomech. 40: 1301–9.

153. Schaller, M.D. 2010. Cellular functions of FAK kinases: insight into molecular mechanisms and novel functions. J. Cell Sci. 123: 1007–13.

154. Webb, D.J., K. Donais, L. a Whitmore, S.M. Thomas, C.E. Turner, et al. 2004. FAK-Src signalling through paxillin, ERK and MLCK regulates adhesion disassembly. Nat. Cell Biol. 6: 154–61.

155. Halder, J., C.N. Landen, S.K. Lutgendorf, Y. Li, N.B. Jennings, et al. 2005. Focal adhesion kinase silencing augments docetaxel-mediated apoptosis in ovarian cancer cells. Clin. Cancer Res. 11: 8829–36.

156. Kang, Y., W. Hu, C. Ivan, H.J. Dalton, T. Miyake, et al. 2013. Role of focal adhesion kinase in regulating YB-1-mediated paclitaxel resistance in ovarian cancer. J. Natl. Cancer Inst. 105: 1485–95.

157. Sood, A., J. Coffin, and G. Schneider. 2004. Biological significance of focal adhesion kinase in ovarian cancer: role in migration and invasion. Am. J. Pathol. 165: 1087–1095.

158. Gundem, G., C. Perez-Llamas, A. Jene-Sanz, A. Kedzierska, A. Islam, et al. 2010. IntOGen: integration and data mining of multidimensional oncogenomic data. Nat. Methods. 7: 92–3.

159. Infante, J.R., D.R. Camidge, L.R. Mileshkin, E.X. Chen, R.J. Hicks, et al. 2012. Safety, pharmacokinetic, and pharmacodynamic phase I dose-escalation trial of PF-00562271, an inhibitor of focal adhesion kinase, in advanced solid tumors. J. Clin. Oncol. 30: 1527–33.

160. Gupton, S.L., and C.M. Waterman-Storer. 2006. Spatiotemporal feedback between actomyosin and focal-adhesion systems optimizes rapid cell migration. Cell. 125: 1361–74.

161. Scalici, J.M., C. Harrer, A. Allen, A. Jazaeri, K. a Atkins, et al. 2014. Inhibition of α4β1 integrin increases ovarian cancer response to carboplatin. Gynecol. Oncol. 132: 455–61.

162. Zutter, M.M. 2007. Integrin-mediated adhesion: tipping the balance between chemosensitivity and chemoresistance. Adv. Exp. Med. Biol. 608: 87–100.

163. Oshita, F., Y. Kameda, N. Hamanaka, H. Saito, K. Yamada, et al. 2004. High expression of integrin beta1 and p53 is a greater poor prognostic factor than clinical stage in small-cell lung cancer. Am. J. Clin. Oncol. 27: 215–9.

164. Lane, D., N. Goncharenko-Khaider, C. Rancourt, and a Piché. 2010. Ovarian cancer ascites protects from TRAIL-induced cell death through alphavbeta5 integrin-mediated focal adhesion kinase and Akt activation. Oncogene. 29: 3519–31.

165. Smith, J. a, H. Ngo, M.C. Martin, and J.K. Wolf. 2005. An evaluation of cytotoxicity of the taxane and platinum agents combination treatment in a panel of human ovarian carcinoma cell lines. Gynecol. Oncol. 98: 141–5.

166. Eaton, S.L., S.L. Roche, M. Llavero Hurtado, K.J. Oldknow, C. Farquharson, et al. 2013. Total protein analysis as a reliable loading control for quantitative fluorescent Western blotting. PLoS One. 8: e72457.

167. Welinder, C., and L. Ekblad. 2011. Coomassie staining as loading control in Western blot analysis. J. Proteome Res. 10: 1416–9.

168. Minotti, A., S. Barlow, and F. Cabral. 1991. Resistance to antimitotic drugs in Chinese hamster ovary cells correlates with changes in the level of polymerized tubulin. J. Biol. Chem. 266: 3987–3994.

169. McGrail, D.J., D. Ghosh, N.D. Quach, and M.R. Dawson. 2012. Differential mechanical response of mesenchymal stem cells and fibroblasts to tumor-secreted soluble factors. PLoS One. 7: e33248.

170. Jaqaman, K., D. Loerke, and M. Mettlen. 2008. Robust single-particle tracking in live-cell time-lapse sequences. Nat. Methods. 5: 695–702.

171. Thiery, J.P. 2002. Epithelial-mesenchymal transitions in tumour progression. Nat. Rev. Cancer. 2: 442–54.

172. Lamouille, S., J. Xu, and R. Derynck. 2014. Molecular mechanisms of epithelial–mesenchymal transition. Nat. Rev. Mol. Cell Biol. 15: 178–196.

173. Nieto, M.A. 2002. The snail superfamily of zinc-finger transcription factors. Nat. Rev. Mol. Cell Biol. 3: 155–66.

174. Herschkowitz, J.I., K. Komurov, A.Y. Zhou, S. Gupta, J. Yang, et al. 2010. Core epithelial-to-mesenchymal transition interactome gene-expression signature is associated with claudin-low and metaplastic breast cancer subtypes. Proc. Natl. Acad. Sci. 107: 19132–19132.

175. Zhou, B.P., J. Deng, W. Xia, J. Xu, Y.M. Li, et al. 2004. Dual regulation of Snail by GSK-3beta-mediated phosphorylation in control of epithelial-mesenchymal transition. Nat. Cell Biol. 6: 931–40.

176. Lee, M.-H., P.-H. Wu, J.R. Staunton, R. Ros, G.D. Longmore, et al. 2012. Mismatch in mechanical and adhesive properties induces pulsating cancer cell migration in epithelial monolayer. Biophys. J. 102: 2731–41.

177. Wirtz, D. 2009. Particle-tracking microrheology of living cells: principles and applications. Annu. Rev. Biophys. 38: 301–326.

178. Seltmann, K., A.W. Fritsch, J. a Käs, and T.M. Magin. 2013. Keratins significantly contribute to cell stiffness and impact invasive behavior. Proc. Natl. Acad. Sci. U. S. A. 110: 18507–18512.

179. Guo, M., A.J. Ehrlicher, S. Mahammad, H. Fabich, M.H. Jensen, et al. 2013. The Role of Vimentin Intermediate Filaments in Cortical and Cytoplasmic Mechanics. Biophys. J. 105: 1562–1568.

180. Mendez, M.G., D. Restle, and P. a. Janmey. 2014. Vimentin Enhances Cell Elastic Behavior and Protects against Compressive Stress. Biophys. J. 107: 314–323.

181. Maekawa, M., T. Ishizaki, S. Boku, and N. Watanabe. 1999. Signaling from Rho to the actin cytoskeleton through protein kinases ROCK and LIM-kinase. Science (80-.). 285: 895–898.

182. Dhasarathy, A., M. Kajita, and P.A. Wade. 2007. The transcription factor snail mediates epithelial to mesenchymal transitions by repression of estrogen receptor-alpha. Mol. Endocrinol. 21: 2907–18.

183. Winston, J.S., H.L. Asch, P.J. Zhang, S.B. Edge, A. Hyland, et al. 2001. Downregulation of gelsolin correlates with the progression to breast carcinoma. Breast Cancer Res. Treat. 65: 11–21.

184. Asch, H.L., K. Head, Y. Dong, F. Natoli, J.S. Winston, et al. 1996. Widespread Loss of Gelsolin in Breast Cancers of Humans, Mice, and Rats. Cancer Res. 56: 4841–4845.

185. Sossey-Alaoui, K., A. Safina, X. Li, M.M. Vaughan, D.G. Hicks, et al. 2007. Down-regulation of WAVE3, a metastasis promoter gene, inhibits invasion and metastasis of breast cancer cells. Am. J. Pathol. 170: 2112–21.

186. Wolf, K., M. te Lindert, M. Krause, S. Alexander, J. te Riet, et al. 2013. Physical limits of cell migration: Control by ECM space and nuclear deformation and tuning by proteolysis and traction force. J. Cell Biol. 201: 1069–1084.

187. Spagnol, S.T., and K. Noel Dahl. 2014. Active cytoskeletal force and chromatin condensation independently modulate intranuclear network fluctuations. Integr. Biol. (Camb). 6: 523–31.

188. Khatau, S.B., S. Kusuma, D. Hanjaya-Putra, P. Mali, L. Cheng, et al. 2012. The differential formation of the LINC-mediated perinuclear actin cap in pluripotent and somatic cells. PLoS One. 7: e36689.

189. Harada, T., J. Swift, J. Irianto, J.-W. Shin, K.R. Spinler, et al. 2014. Nuclear lamin stiffness is a barrier to 3D migration, but softness can limit survival. J. Cell Biol. 204: 669–682.

190. Agus, D.B., J.F. Alexander, W. Arap, S. Ashili, J.E. Aslan, et al. 2013. A physical sciences network characterization of non-tumorigenic and metastatic cells. Sci. Rep. 3.

191. Guck, J., S. Schinkinger, B. Lincoln, F. Wottawah, S. Ebert, et al. 2005. Optical deformability as an inherent cell marker for testing malignant transformation and metastatic competence. Biophys. J. 88: 3689–98.

192. Xu, W., R. Mezencev, B. Kim, L. Wang, J. McDonald, et al. 2012. Cell stiffness is a biomarker of the metastatic potential of ovarian cancer cells. PLoS One. 7: e46609.

193. Swaminathan, V., K. Mythreye, E.T. O'Brien, A. Berchuck, G.C. Blobe, et al. 2011. Mechanical stiffness grades metastatic potential in patient tumor cells and in cancer cell lines. Cancer Res. 71: 5075–80.

194. Beach, J.R., G.S. Hussey, T.E. Miller, A. Chaudhury, P. Patel, et al. 2011. Myosin II isoform switching mediates invasiveness after TGF-β-induced epithelial-mesenchymal transition. Proc. Natl. Acad. Sci. U. S. A. 108: 17991–6.

195. Wu, P.-H., C.M. Hale, W.-C. Chen, J.S.H. Lee, Y. Tseng, et al. 2012. High-throughput ballistic injection nanorheology to measure cell mechanics. Nat. Protoc. 7: 155–70.

196. Dahl, K.N., A.J. Engler, J.D. Pajerowski, and D.E. Discher. 2005. Power-law rheology of isolated nuclei with deformation mapping of nuclear substructures. Biophys. J. 89: 2855–64.

197. Pajerowski, J., and K. Dahl. 2007. Physical plasticity of the nucleus in stem cell differentiation. Proc. …. 104: 15619–15624.

198. Mani, S. a, W. Guo, M.-J. Liao, E.N. Eaton, A. Ayyanan, et al. 2008. The epithelial-mesenchymal transition generates cells with properties of stem cells. Cell. 133: 704–15.

199. Tarin, D. 2005. The fallacy of epithelial mesenchymal transition in neoplasia. Cancer Res. : 5996–6001.

200. Chen, J., L. Wang, L. V Matyunina, C.G. Hill, and J.F. McDonald. 2011. Overexpression of miR-429 induces mesenchymal-to-epithelial transition (MET) in metastatic ovarian cancer cells. Gynecol. Oncol. 121: 200–5.

201. Roose, T., P. a. Netti, L.L. Munn, Y. Boucher, and R.K. Jain. 2003. Solid stress generated by spheroid growth estimated using a linear poroelasticity model. Microvasc. Res. 66: 204–212.

202. Tusher, V.G., R. Tibshirani, and G. Chu. 2001. Significance analysis of microarrays applied to the ionizing radiation response. Proc. Natl. Acad. Sci. U. S. A. 98: 5116–21.

203. Shi, W., M. Bessarabova, D. Dosymbekov, Z. Dezso, T. Nikolskaya, et al. 2010. Functional analysis of multiple genomic signatures demonstrates that classification algorithms choose phenotype-related genes. Pharmacogenomics J. 10: 310–23.

204. Huang, D.W., B.T. Sherman, and R.A. Lempicki. 2009. Systematic and integrative analysis of large gene lists using DAVID bioinformatics resources. Nat. Protoc. 4: 44–57.

205. Huang, D.W., B.T. Sherman, and R.A. Lempicki. 2009. Bioinformatics enrichment tools: paths toward the comprehensive functional analysis of large gene lists. Nucleic Acids Res. 37: 1–13.

206. Subramanian, A., P. Tamayo, V.K. Mootha, S. Mukherjee, B.L. Ebert, et al. 2005. Gene set enrichment analysis: a knowledge-based approach for interpreting genome-wide expression profiles. Proc. Natl. Acad. Sci. U. S. A. 102: 15545–50.

207. Crocker, J., and D. Grier. 1996. Methods of digital video microscopy for colloidal studies. J. Colloid Interface Sci. 310: 298–310.

208. Mason, T. 2000. Estimating the viscoelastic moduli of complex fluids using the generalized Stokes–Einstein equation. Rheol. Acta. 39: 371–378.

209. Fletcher, D. a, and R.D. Mullins. 2010. Cell mechanics and the cytoskeleton. Nature. 463: 485–492.

210. Chaudhuri, O., S.H. Parekh, and D. a Fletcher. 2007. Reversible stress softening of actin networks. Nature. 445: 295–298.

211. Wang, N., J.P. Butler, and D.E. Ingber. 1993. Mechanotransduction across the cell surface and through the cytoskeleton. Science. 260: 1124–1127.

212. Jiang, H., and S.X. Sun. 2013. Cellular pressure and volume regulation and implications for cell mechanics. Biophys. J. 105: 609–19.

213. Tse, J.M., G. Cheng, J. a Tyrrell, S. a Wilcox-Adelman, Y. Boucher, et al. 2012. Mechanical compression drives cancer cells toward invasive phenotype. Proc. Natl. Acad. Sci. U. S. A. 109: 911–6.

214. Hui, T.H., Z.L. Zhou, J. Qian, Y. Lin, a. H.W. Ngan, et al. 2014. Volumetric Deformation of Live Cells Induced by Pressure-Activated Cross-Membrane Ion Transport. Phys. Rev. Lett. 113: 118101.

215. Stroka, K.M., H. Jiang, S.-H. Chen, Z. Tong, D. Wirtz, et al. 2014. Water Permeation Drives Tumor Cell Migration in Confined Microenvironments. Cell. 157: 611–623.

216. Hoffmann, E.K., I.H. Lambert, and S.F. Pedersen. 2009. Physiology of cell volume regulation in vertebrates. Physiol. Rev. 89: 193–277.

217. Gilpin, W., S. Uppaluri, and C.P. Brangwynne. 2015. Article Worms under Pressure : Bulk Mechanical Properties of C . elegans Are Independent of the Cuticle. Biophysj. 108: 1887–1898.

218. Yap, T. a, C.P. Carden, and S.B. Kaye. 2009. Beyond chemotherapy: targeted therapies in ovarian cancer. Nat. Rev. Cancer. 9: 167–81.

219. Nakayama, K., N. Nakayama, H. Katagiri, and K. Miyazaki. 2012. Mechanisms of ovarian cancer metastasis: biochemical pathways. Int. J. Mol. Sci. 13: 11705–17.

220. Hibbs, K., K.M. Skubitz, S.E. Pambuccian, R.C. Casey, K.M. Burleson, et al. 2004. Differential gene expression in ovarian carcinoma: identification of potential biomarkers. Am. J. Pathol. 165: 397–414.

221. Paget, S. 1889. THE DISTRIBUTION OF SECONDARY GROWTHS IN CANCER OF THE BREAST. Lancet. 133: 571–573.

222. Koboldt, D.C., R.S. Fulton, M.D. McLellan, H. Schmidt, J. Kalicki-Veizer, et al. 2012. Comprehensive molecular portraits of human breast tumours. Nature. : 1–10.

223. Stewart, M.P., J. Helenius, Y. Toyoda, S.P. Ramanathan, D.J. Muller, et al. 2011. Hydrostatic pressure and the actomyosin cortex drive mitotic cell rounding. Nature. 469: 226–30.

224. Calvo, F., N. Ege, A. Grande-Garcia, S. Hooper, R.P. Jenkins, et al. 2013. Mechanotransduction and YAP-dependent matrix remodelling is required for the generation and maintenance of cancer-associated fibroblasts. Nat. Cell Biol. 15: 637–646.